

November 2017

# RF Sensing System for Continuous Blood Glucose Monitoring

Fabiola Araujo Cespedes

University of South Florida, [fabiola@mail.usf.edu](mailto:fabiola@mail.usf.edu)

Follow this and additional works at: <http://scholarcommons.usf.edu/etd>

 Part of the [Biomedical Engineering and Bioengineering Commons](#), and the [Electrical and Computer Engineering Commons](#)

## Scholar Commons Citation

Araujo Cespedes, Fabiola, "RF Sensing System for Continuous Blood Glucose Monitoring" (2017). *Graduate Theses and Dissertations*. <http://scholarcommons.usf.edu/etd/6998>

This Dissertation is brought to you for free and open access by the Graduate School at Scholar Commons. It has been accepted for inclusion in Graduate Theses and Dissertations by an authorized administrator of Scholar Commons. For more information, please contact [scholarcommons@usf.edu](mailto:scholarcommons@usf.edu).

# RF Sensing System for Continuous Blood Glucose Monitoring

by

Fabiola Araujo Cespedes

A dissertation submitted in partial fulfillment  
of the requirements for the degree of  
Doctor of Philosophy  
Department of Electrical Engineering  
College of Engineering  
University of South Florida

Major Professor: Stephen E. Sadow, Ph.D.  
Gokhan Mumcu, Ph.D.  
Silvia W. Thomas, Ph.D.  
Robert Frisina, Ph.D.  
Lennox Hoyte, M.D.

Date of Approval:  
November 2, 2017

Keywords: Non-invasive sensing, implantable sensing, blood sugar level, blood permittivity,  
antenna patch

Copyright © 2017, Fabiola Araujo Cespedes

## ACKNOWLEDGEMENTS

I would like to thank my supervisor Dr. Stephen Sadow for all his support and guidance throughout my graduate studies. I would like to thank Dr. Gokhan Mumcu for this guidance on the antenna simulations. I would like to thank Dr. Hoff and Dr. Bhanja for their academic support during my studies. Thank you to the Electrical Engineering Department for their teaching assistant support. Thank you to Schlumberger Faculty for the Future for their fellowship financial support during the endeavor. Thank you to the USF Graduate department for the USF Signature Research Fellowship and to the College of Engineering for the Da Vinci grant.

I thank all academic discussion and help by different friends and family members received at one point or another during the elaboration of my research. Deep and special thank you to my husband, Rodrigo Perales, who helped with several aspects during the elaboration of my research at different instances.. Thank you to Dr. Shamima Afroz for her input and information provided on her research on active sensing. Thank you to Maria Elena Fiol for her discussions and contributions in the electronic system platform of the system. Thank you to Michael Grady, Eduardo Rojas, Timothy Palomo, Merve Kacar, Ramiro Ramirez, Mona Fathollahi and any other who directly or indirectly contributed in my research. I thank my parents for the educational background they gave me, their love and support. I thank my sisters Monica, Paola and Ana Karina, who have always encouraged me. And last, but not least, I thank my daughters, Ariana and Noelia for being such wonderful and amazing girls that inspired and motivated me daily.

## TABLE OF CONTENTS

LIST OF TABLES.....	iv
LIST OF FIGURES .....	v
ABSTRACT.....	ix
CHAPTER 1: INTRODUCTION.....	1
1.1 Overview of Glucose Monitoring .....	1
1.1.1 Diabetes and Self-Monitoring of Glucose Levels .....	1
1.1.2 Self-Monitoring Glucose Methods .....	1
1.1.3 Developing Alternatives for Self- Monitoring Blood Glucose.....	2
1.2 Problem Statement.....	5
1.3 Research Objective .....	6
1.4 Research Background .....	6
1.5 Contributions of Dissertation.....	8
1.6 Dissertation Summary and Organization .....	8
CHAPTER 2: RF GLUCOSE SENSING .....	10
2.1 Overview of Antenna Glucose Sensing Models .....	10
2.1.1 Implantable Active Sensing .....	10
2.1.2 Implantable Passive Sensing .....	11
2.1.3 Non-Invasive Sensing .....	11
2.2 Glucose Dependent Properties of Blood.....	12
2.2.1 Permittivity and Conductivity of Blood .....	12
2.2.2 Blood Glucose Dependent Experiments.....	12
2.2.3 Sensing of Blood Glucose Levels with a 10GHz SiC Antenna.....	16
2.3 Human Tissue Models .....	17
2.3.1 Electrical Parameters for Each Human Tissue .....	17
2.3.2 Human Tissue Model for Active and Passive Implantable Sensing .....	18
2.3.2.1 Location in Human Body.....	18
2.3.2.2 Thickness Approximations of Human Tissue .....	19
2.3.2.3 Human Tissue Model for Implantable Sensing.....	19
2.3.3 Human Tissue Model for Non-Invasive Sensing.....	20
2.3.3.1 Location in Human Body.....	20
2.3.3.2 Thickness Approximations of Human Tissue .....	20
2.3.3.3 Human Tissue Models for Non-invasive Sensing.....	22
2.4 Electromagnetic Simulation Setup .....	23
2.4.1 HFSS™ Overview .....	23
2.4.2 PML Boundaries .....	23
2.5 Antenna Design for ISM Band (5.8 GHz) in Free Space .....	25
2.5.1 Antenna Design Overview.....	25
2.5.2 Optimizing the Antenna to Resonate at 5.8 GHz .....	26
2.6 Antenna Design for Active Sensing Mode.....	28

2.6.1	Antenna Design Overview.....	28
2.6.2	Antenna Matching to Tissue Environment.....	29
2.6.2.1	Varying the Parameter $P_y$ .....	29
2.6.2.2	Variation of Parameter PatchX. ....	30
2.6.3	Resulting Antenna Dimensions.....	31
2.6.4	Effect of Glucose Levels in Blood.....	32
2.6.5	Summary of Active Sensing Antenna Design.....	33
2.7	Passive Sensing Simulations.....	33
2.7.1	Overview of Passive Sensing System.....	33
2.7.2	Single External Antenna.....	34
2.7.3	External Antennas Tx and Rx.....	36
2.7.4	Implantable Antenna.....	37
2.7.4.1	Sensing Properties.....	38
2.7.4.2	Communication with External Antennas.....	39
2.7.4.2.1	Effect of Embedded Substrate and Ground.....	40
2.7.4.2.2	Effect of Embedded Patch, Substrate and Ground.....	45
2.7.5	Passive System Simulations with Varying Blood Glucose Levels.....	46
2.7.6	Summary of Passive Sensing Design.....	48
2.8	Non-invasive Sensing Simulations.....	49
2.8.1	Overview of Non-invasive Sensing.....	49
2.8.2	Effect of Variation of Blood Vessel Electrical Permittivity.....	50
2.9	Chapter Conclusion.....	51
CHAPTER 3: NON-INVASIVE ANTENNA BLOOD GLUCOSE SENSOR.....		52
3.1	Chapter Overview.....	52
3.2	Non-Invasive Antenna Experimental Measurements.....	52
3.2.1	Introduction to Human Tissue Phantoms.....	52
3.2.2	Human Tissue Phantoms Mimicking Electrical Properties.....	53
3.2.3	Experimental Measurements.....	58
3.2.3.1	Experimental Setup.....	58
3.2.3.2	Measured and Simulated Results.....	59
3.3	Factors that Affect the Non-Invasive Antenna's Return Loss.....	61
3.3.1	Physiological Factors.....	61
3.3.1.1	Skin Thickness and Resonant Frequency.....	61
3.3.1.2	Deepness of the Blood Vessel.....	63
3.3.2	Misalignment of Antenna.....	63
3.3.2.1	Vertical Displacement.....	63
3.3.2.2	Lateral Displacement.....	64
3.4	Chapter Summary.....	65
CHAPTER 4: GLUCOSE SENSOR SYSTEM.....		67
4.1	Chapter Overview.....	67
4.2	System Platform Hardware.....	67
4.2.1	Bi-Directional Coupler.....	68
4.2.2	Demodulating Logarithmic Amplifier.....	71
4.2.3	PIC Microcontroller 18F4221.....	74
4.2.4	Glucose Meter Display.....	75
4.2.5	System Platform Miniaturization.....	75
4.3	Non-Invasive Sensing Algorithm.....	76
4.4	Registration of Antenna Placement over Blood Vessel.....	83
4.5	Chapter Summary.....	85

CHAPTER 5: CONCLUSIONS AND FUTURE WORK .....	87
5.1 Summary .....	87
5.2 Recommendations and Future Work .....	91
REFERENCES .....	94
APPENDIX A: PERMISSION FOR MATERIAL IN CHAPTER 2.....	99
APPENDIX B: PERMISSION FOR FIGURE 4.....	101
APPENDIX C: PERMISSION FOR IEEE PUBLISHED FIGURES.....	106
APPENDIX D: PERMISSION FOR FIGURE 13 .....	107

## LIST OF TABLES

Table 1: Summary of non-invasive devices/company's status.....	3
Table 2: Conductivity and permittivity of human tissues at 2.4, 5.8 and 10GHz [37]......	17
Table 3: Human arm model physical dimensions. ....	21
Table 4: Propagation constant of each layer of human tissues.....	24
Table 5: Antenna patch dimensions for free space operation at 5.8 GHz .....	27
Table 6: Antenna dimensions for implantable antenna.....	31
Table 7: Antenna dimensions for non-invasive blood glucose sensing. ....	50
Table 8: Human tissue phantom ingredients for upper arm for skin, fat and muscle.....	54
Table 9: D-Glucose concentrations in blood phantom and $\epsilon_r$ .....	57

## LIST OF FIGURES

Figure 1: Active sensing antenna implanted in abdominal area configuration.....	10
Figure 2: Implanted passive sensing antenna and external antennas configuration. ....	11
Figure 3: Non-invasive sensing antenna on top of the arm configuration.....	11
Figure 4: Water/glucose concentration dependence of the dielectric constant. ....	13
Figure 5: Frequency dependence in blood gel as a function of sugar.....	13
Figure 6: Frequency dependence in blood gel as a function of sugar.....	14
Figure 7: Relative permittivity of blood plasma vs. glucose levels concentration .....	15
Figure 8: Electrical conductivity of blood plasma vs. glucose levels concentration. ....	15
Figure 9: Return loss of a 10GHz antenna for various blood glucose concentration.....	16
Figure 10: Resonance frequency vs. glucose concentration of a 10 GHz SiC antenna. ....	17
Figure 11: Proposed implant position in the fatty area of the front abdominal wall.....	18
Figure 12: Human tissue model for implant showing the thickness and $\epsilon_r$ of each layer. ....	19
Figure 13: Antenna patch location over the arm showing cross sectional anatomy. ....	20
Figure 14: Complete human tissue model for non-invasive sensing simulations. ....	22
Figure 15: Simplified human tissue model for non-invasive sensing simulations. ....	23
Figure 16: Human tissue model with (a) no PML boundary and b) with PML boundary. ....	24
Figure 17: Schematic top and cross section views of the SiC RF antenna. ....	25
Figure 18: Simulated antenna in free space to optimize operation at 5.8 GHz. ....	26
Figure 19: Plot of simulation data showing variation in $f_0$ vs. the variable Patch Y. ....	26
Figure 20: Simulated data showing variation of S11 based on the location of feed py.....	27
Figure 21: Final free-space antenna design showing simulated resonance at 5.80 GHz. ....	28
Figure 22: Simulated antenna beam profile of final optimized antenna.....	28



Figure 23: Return loss of active antenna based on $p_y$ variation. ....	29
Figure 24: Resonant frequency and gain of active antenna based on $p_y$ variation. ....	30
Figure 25: Return loss of active antenna based on patchX variation. ....	30
Figure 26: Resonant frequency and $S_{11}$ of active antenna based on patch X variation.....	31
Figure 27: $S_{11}$ of the optimized implantable antenna. ....	31
Figure 28: Simulated $S_{11}$ of antenna in human tissue results in a shift of resonant frequency as blood permittivity varies. ....	32
Figure 29: Plot of simulated resonant frequency vs. blood permittivity of the antenna. ....	32
Figure 30: Passive sensing requires an implantable antenna and two external antennas. ....	34
Figure 31: Simulation setup with one external antenna only in the air space.....	35
Figure 32: Simulated $S_{11}$ for external (or internal) antenna only. ....	35
Figure 33: Simulation model for both external antennas separated by 1, 10 or 20mm.....	36
Figure 34: $S_{11}$ for external antenna setup of Figure 33, for sep_d= 1,10 and 20mm.....	36
Figure 35: $S_{21}$ for external antenna setup of Figure 33 for sep_d=1, 10 and 20mm.....	37
Figure 36: Implantable antenna as a two single sided antenna with two functions. ....	38
Figure 37: Partial implanted antenna must detect glucose variations. ....	38
Figure 38: Partial implanted antenna must communicate with the external antennas.....	39
Figure 39: Simulated $S_{21}$ results of passive sensing antenna setup in free space. ....	39
Figure 40: External antennas and embedded in fat substrate with ground plane model. ....	41
Figure 41: Simulated $S_{21}$ of external antennas with internal substrate with a ground plane at 2mm from blood / muscle layer. ....	41
Figure 42: Simulated $S_{21}$ of external antennas with internal substrate with a ground plane at 7mm from blood / muscle layer. ....	42
Figure 43: Simulated effect of implanted substrate on $S_{21}$ of external antennas separated by 1mm.....	43
Figure 44: Simulated effect on implanted substrate on $S_{21}$ of external antennas separated by 10mm. ....	43
Figure 45: Simulated effect of implanted substrate on $S_{21}$ of external antennas separated by 20mm.....	44

Figure 46: Comparison of the simulated $S_{21}$ [dB] of the external antennas at 5.8GHz as a function of their separation and in relation to the internal implant position.....	44
Figure 47: Configuration with implant in fat layer 2mm and 7 mm from the blood layer. ....	45
Figure 48: Effect on the $S_{21}$ of external antennas of adding patch on implanted substrate and ground at 2mm from blood layer. ....	45
Figure 49: Effect on the $S_{21}$ of external antennas of adding patch on implanted substrate and ground at 7mm from blood.....	46
Figure 50: Passive dual antenna system as modeled in HFSS - side view.....	47
Figure 51: Three antennas passive system as modeled in HFSS - angular view.....	47
Figure 52: Passive antenna effect on $S_{21}$ of external antennas vs. blood permittivity. ....	48
Figure 53: Variation of blood permittivity vs. return loss for non-invasive antenna.....	50
Figure 54: Coaxial probe method for measuring the permittivity of solids and semi-solids using an HP dielectric probe model 85070 [55].....	54
Figure 55: HP Dielectric probe model 85070 measurement on each human tissue layer. ....	54
Figure 56: Dielectric properties of human tissue phantoms for skin, muscle and blood. ....	55
Figure 57: Dielectric properties of the fat tissue phantom. ....	55
Figure 58: Photograph of HP dielectric probe model 85070 used to measure the dielectric properties of the on blood glucose samples. ....	56
Figure 59: Permittivity, $\epsilon_r$ , of blood phantom samples with added D-glucose.....	56
Figure 60: Measured relative permittivity at 5.8GHz vs. glucose level. ....	57
Figure 61: Steps for layering the human tissue with the blood vessel phantom.....	58
Figure 62: Photographic sequence showing the assembly of the human tissue phantom. ....	59
Figure 63: Return loss of the antenna as a function of glucose concentration. ....	60
Figure 64: Measured and simulated $f_o$ vs. glucose concentration [mg/dL] and blood $\epsilon_r$ . ....	61
Figure 65: Skin thickness variation effect on resonant frequency. ....	62
Figure 66: Effect of blood vessel depth variation on resonant frequency.....	63
Figure 67: Vertical variation effect on the return loss of the non-invasive antenna. ....	64
Figure 68: Simulated effect of antenna misaligned from blood vessel. ....	65
Figure 69: Block diagram of system platform for non-invasive sensing. ....	68

Figure 70: Bi-directional coupler port connections to the circuitry.....	69
Figure 71: Measurements taken on coupler AMTERY model no. CP20008A.....	70
Figure 72: Measurement setup with bi-directional coupler and phantom.....	70
Figure 73: Setup to characterize the demodulating logarithmic amplifier AD8318.....	72
Figure 74: Measured $V_{OUT}$ vs. $P_{IN}$ (dBm) at 5.8GHz using the setup of Fig. 83.....	72
Figure 75: Measurement setup using the bi-directional coupler and logarithmic amplifier.....	73
Figure 76: Preliminary test bi-directional coupler and the AD8318 for air, phantom without a blood vessel and phantom with blood vessel at 500mg/dL.....	73
Figure 77: Antenna return loss power and bi-directional coupler output analysis.....	76
Figure 78: Illustration of antenna resonating at different frequencies per medium.....	77
Figure 79: Block illustration of signal generated at frequencies $f_1$ , $f_2$ , $f_3$ and antenna facing medium 1.....	78
Figure 80: Block illustration of signal generated at frequencies $f_1$ , $f_2$ , $f_3$ and antenna facing medium 2.....	78
Figure 81: Block illustration of signal generated at frequencies $f_1$ , $f_2$ , $f_3$ and antenna facing medium 3.....	79
Figure 82: Non-invasive sensor system block diagram.....	80
Figure 83: Sensor system test conducted at 5.875GHz for three different mediums.....	81
Figure 84: Photograph of the evaluation prototype for non-invasive glucose sensing with parts description.....	82
Figure 85: Photograph of the evaluation prototype for non-invasive glucose sensing under test using pork tissue and mimicking liquid blood phantoms.....	83
Figure 86: Top view of calibration model parallel to blood vessel.....	84
Figure 87: Return loss for sensing antenna and reference antennas.....	85
Figure 88: Top view of registration model at an angle with respect to the blood vessel.....	85
Figure 89: Implantable blood glucose sensing system to control insulin pump.....	92
Figure 90: Stand-alone glucose monitoring system with antennas in tubular device.....	93

## ABSTRACT

The purpose of this research was to design a blood glucose sensing system based on the induced shift in the resonant frequency of an antenna patch operating in the ISM band (5.725 – 5.875 GHz). The underlying concept is the fact that when a person has variations in their blood glucose levels, the permittivity of their blood varies accordingly. This research analyzed the feasibility of using an antenna patch as a blood glucose sensing device in three configurations: 1) as an implantable active sensor, 2) as an implantable passive antenna sensor, and 3) as a non-invasive sensor. In the first arrangement, the antenna is to be implanted inside the body as an active antenna, requiring that its power supply and internal circuitry to be implanted. In the second arrangement, the antenna is also implanted, but would not require a power supply or internal circuitry since it would be passive. For the third arrangement, the non-invasive sensing approach, the antenna is placed facing the upper arm while mounted outside the body. In order to evaluate the best approach all the three approaches were simulated using the electromagnetic field tool simulator ANSYS EM15.0 HFSS™, along with a human tissue model. The tissue model included physiological and electrical characteristics of the human abdomen for simulating the active and passive approaches, and the upper arm for the non-invasive approach. The electromagnetic boundaries were set with perfectly matched layers to eliminate any reflections which would cause a non-physical resonance in the results. Simulation of the active sensing configuration resulted in a resonant frequency shift from 5.76 to 5.78GHz (i.e., a 20 MHz shift) for a simulated blood permittivity variation of 62.0 to 63.6. This corresponds, theoretically, to an approximate glucose shift of 500 mg/dL. The passive configuration simulations did not yield conclusive variations in resonant frequency and this approach was abandoned early on in this research. Thirdly, the non-invasive approach resulted in a simulated shift of resonant frequency

from 5.797 to 5.807 (i.e., a 10MHz shift) for simulated blood permittivity variation of 51.397 to 52.642 (an approximate variation of 2000 mg/dL in glucose). In the literature planar, continuous blood-rich layers are used to simulate RF sensing of glucose, which is not applicable when measuring glucose in actual human veins, which are tubular in geometry and of finite extent. Therefore the model employed assumed a 1.8 mm diameter blood vessel, buried under a fatty layer that was capped with skin. The above results, both simulated and verified experimentally, used this more realistic model which is further proof that a practical non-invasive blood glucose measurement system should be possible.

The non-invasive approach was tested experimentally by using oil in gel phantoms to mimic the electrical properties of skin, fat, blood and muscle. A fat phantom was placed over a muscle phantom, with a strip of blood phantom within and a skin phantom was placed on top. The blood phantom had a 2000mg/dL variation of D-glucose in the phantom mixture which decreased the relative permittivity from 52.635 to 51.482 and resulted in a shift of resonant frequency from 5.855 to 5.842 (i.e., a 13MHz shift). This is consistent with the non-invasive simulated results thus validating our model of the non-invasive sensing approach. While this variation in blood glucose is non-physical (typical human glucose range can range in the extremes from 30 to 400 mg/dL, where healthy glucose levels vary from 70mg/dL to 180mg/dL) it was necessary to provide a high confidence fit between the simulated and experimental data. This is because the level of precision with which the physical phantoms could be fabricated with was insufficient to match the highly precise simulated data.

Analysis on the effect of lateral displacement of the antenna from the blood vessel, its elevation above the skin and variations caused by different skin thickness, and blood vessel depth were evaluated. A calibration technique to correct physical misalignment by the user is proposed in which two additional antennas, located diagonally with respect to the sensing antenna, serve as reference point for placement over the upper arm in line of sight with the blood vessel.

Once the non-invasive sensor approach was shown to be viable for continuous glucose monitoring, a sensor platform was designed whereby an RF generator was used to drive the antenna with a frequency sweep between 5.725 to 5.875GHz. A fraction of its output power was coupled to both the antenna and the system analysis circuitry through a directional coupler. The transmitted and received power were then processed with demodulating logarithmic amplifiers which convert the RF signal to a corresponding voltage for downstream processing. Both inputs were then fed into a microcontroller and the measured shift in resonant frequency,  $f_o$ , converted to glucose concentration which was displayed on glucose meter display.

## CHAPTER 1: INTRODUCTION

### 1.1 Overview of Glucose Monitoring

#### 1.1.1 Diabetes and Self-Monitoring of Glucose Levels

The American Diabetes Association estimates that nearly 10% of the US population has diabetes and that, by 2050, 1 in 3 Americans will have diabetes. Diabetes Mellitus is a metabolic disease in which the body is unable to produce or properly use insulin, leading to elevated glucose levels in the blood, known as hyperglycemia. A person with frequent or extended episodes of hyperglycemia can suffer from complications in the nervous system, blood vessels and other organs, as well heart disease, kidney disease, strokes, vision loss, and amputation [1] [2] [3]. Therefore, maintaining a healthy glucose level is essential in a person's life.

Clinical studies have proven that self-monitoring of glucose levels helps treatment decisions in insulin and non-insulin use patients with diabetes [1]. The Central and Eastern Europe Diabetes Technologies and Therapeutics organization stated that self-monitoring glucose is an "essential tool that should be accessible to all patients with diabetes" providing a report of numerous benefits and recommendations [4]. Simply stated self-monitoring of glucose improves health by allowing the patient to be able to take proper decisions based on their glucose levels [1] [3]. Therefore, effective and feasible methods to measure blood glucose are essential.

#### 1.1.2 Self-Monitoring Glucose Methods

A person can monitor their glucose levels via the conventional self-monitoring blood glucose (SMBG) method by taking finger prick blood samples, or through continuous monitoring glucose (CMG) means. For SMBG, the patient withdraws a drop of capillary blood sample from

the fingertip to measure the blood glucose levels at that instant in time. [5] Since, in some cases, patients are recommended to check their blood glucose at least 8 to 10 times a day, the repeated procedure of finger pricking can be painful [6] and cause calluses over time thus increasing the pain [7]. Additionally, since the results show instantaneous blood glucose levels, patients with extreme conditions could suffer episodes of dangerous levels of glucose at instances that the blood glucose is not being monitored [6].

On the other hand, CMG consists of a device that detects the patient's glucose levels continuously in real time, overcoming the problem of continuity. Unfortunately all currently FDA approved CMG methods are short term, as the disposable needle-type is an amperometric enzyme electrode that is inserted in the body and lasts only up to 14 days [8]. In addition to the pain and hassle associated to the approximate weekly installation of the needle sensor, some CMG require calibration four times a day with the finger sticking blood sample technique [3] [4] since the measurement is not done directly on the blood glucose, but rather measures the glucose of the interstitial fluid (ISF). Newer versions of CMG no longer require the calibration, but the device itself and the cost of the disposable needle can make these CGM systems marketed by Medtronic, DexCom STS and Abbott FreeStyle Navigator result in elevated costs.

### **1.1.3 Developing Alternatives for Self- Monitoring Blood Glucose**

Several alternatives for self-monitoring blood glucose (SMBG) have been researched over the last years, striving to overcome the pain and hassle of 7 to 14 day sensor reinsertion and in some CGM, calibrations with finger pricking techniques. Unfortunately, these new alternatives are faced with numerous limitations and accuracy problems thus pointing to the critical need for a more accurate, user-friendly CGM system to improve patient quality of life.

One approach is non-invasive technology, but no non-invasive technology has successfully functioned in the market [9]. By way of example, the Gluowatch that came out in



the market was discontinued after 2007 due to showing poor results and a serious defect of burning patient skin [9] [10]., Other products, such as the Glucoband, Conga Medical Glucometer, or C8MediSensors, have disappeared from the market [9] [11]. Several others are still under development such as Biosensors [12], I-Sugar X Meditech [13], Easy Check [14], and EyeSense [15], or not yet FDA approved, such as the GlucoTrack [16] and SCOUT [17]. Table 1 summarizes a list of devices/companies for continuous glucose sensing technology with their status as of October 2017, which does not include the discontinued devices Gluowatch, Diasensor and Pendra [18], or products that have disappeared from the market. Last accessed October 2017.

Table 1: Summary of non-invasive devices/company's status.

Device/ Company*	Technology	Status	Source
Biosensors	SEMP technique (Bioimpedance spectroscopy)	Under development [12]	<a href="http://www.biosensors-tech.com/">http://www.biosensors-tech.com/</a>
I-Sugar X Meditech	Fluorescent technology	Under development [13]	<a href="http://www.freedom-meditech.com/">http://www.freedom-meditech.com/</a>
EyeSense	Fluorescent technology	Under development. Launch postponed to 2015 [15]	<a href="http://en.eyesense.com/">http://en.eyesense.com/</a>
GlucoTrack	Thermal, Ultrasound and Electromagnetic Technologies	Approved 2013 in Europe. Not yet approved by FDA [16]	<a href="http://www.integrity-app.com/">http://www.integrity-app.com/</a>
Glove Instruments	NIR Spectrosocopy	Not concluded. [19]	<a href="http://groveinstruments.com/">http://groveinstruments.com/</a>
OrSense Ltd. SCOUT DS, Verelight Inc.	Occlusion technology Fluorescent spectroscopy	Not concluded. [20] Not concluded [17]	<a href="http://www.orsense.com/Glucose">http://www.orsense.com/Glucose</a> <a href="http://www.verelight.com/products.html">http://www.verelight.com/products.html</a>

Most non-invasive glucose monitoring systems face the challenge of being susceptible to external interference from other factors such as body temperature, perspiration, skin moisture, changes in skin thickness and body movement [13]. For instance, infrared spectroscopy, including near infrared (NIR) spectroscopy and far infrared (FIR) spectroscopy, depend on optical transmission and reflection measurements, which are subject to interference from external factors that affect the reflection measurement. For this reason, NIR requires frequent recalibration. In FIR, the emitted energy that is absorbed by glucose and measured is so small that this method

has not yet been proven to be accurate enough for this application [7, 10]. In other methods, such as Raman Spectroscopy, the measurement of light scattering that is caused by generated oscillations such as laser oscillation in the ocular fluid is subject to interference from other molecules [10, 18]. In thermal spectroscopy, the IR radiation that is emitted from the body is also affected by other factors external to glucose concentration [10]. Another example is the technology based on measuring the ISF fluid that is secreted from the skin to measure the glucose levels which presents a time lag deficiency [21]. Overall, non-invasive technologies lack accuracy due to being susceptible to external factors such as transpiration, temperature, positioning, among other variables, or display time lags of up to 20 minutes, making the technology not yet reliable [18]. This has led to discontinued devices such as the Gluowatch, Diasensor and Pendra [18, 12] or have postponed the estimated launching date as is the case for the Eyesense.

Another approach towards self-glucose monitoring is a fully implantable glucose monitoring system. These medical devices face other types of challenges such as in-vivo inflammatory reaction and foreign body reaction, posing risk for the patients and hence the need for biocompatibility tests on any implantable device [22]. No current biosensor can operate for longer than a few days in-vivo [23]. In a reaction to foreign materials, the body forms an encapsulation around the object that is generally 100 microns thick, which not only acts as a diffusion barrier, but is also electrically insulating. Therefore, long-term implantations are subject to gradual loss of sensor functionality and stability due to fibrosis encapsulation and tissue changes in proximity of the sensor [22, 24, 23]. Therefore, implantable devices, including antennas, are coated with biocompatible materials, but in the aspect of communicating externally from the body, this adds to the effects of sensor encapsulation [25].

In addition to the issue of biocompatibility, the life cycle of the implanted device is relevant to factors such as the sensing mechanism inside the body and the energy required to function properly. For instance, the developing device by GlySens is in trial stage and is expecting to start taking preorders late 2018. The life cycle expectancy of this device is only one year after

implantation [26]. During the wide gap of research pertaining implantable devices, no development has been proposed to function longer than 18 months due to one or more of the previously mentioned challenges faced by implantable devices for a truly “long-term” implantable solution.

## 1.2 Problem Statement

Statistical studies have proven the link between blood glucose levels and the incidence of diabetes-related complications [3]. Ideally, patients with frequent or prolonged elevated glucose levels should monitor their glucose levels continuously to be able to avoid the related complications and improve their health. Although having a CGM system allows people with diabetes to have better control of their health and life decisions, only 10% of the people with Type I diabetes type use it, due to factors such as lack of education, and cost [5].

Other factors include fear of inserting the needle-like electrodes into their bodies, the hassle of repeating this process once the disposable needle-like electrode reaches its life cycle of 7 to 14 days, [6]. Other alternatives, such as implantable devices, have challenges such as biocompatibility, an accurate and repeatable sensing mechanism, communication with the exterior and the life time of electrical energy required for operation inside the body. For this reason, developments such as long-term CGM by GlySens, while a significant step forward, will only be effective up to 18 months after implantation.

Non-invasive alternative solutions could avoid the need for an implant as well as finger pricking and insertion of disposable needle-like electrodes. Additionally, it could reduce the cost of a surgery or the cost of disposable needles. For this reason, global research has been concentrating on the search for an alternative blood glucose monitoring system, but to the best of our knowledge, no non-invasive glucose monitoring system has been FDA approved for use and while research in several institutions is on-going.

### 1.3 Research Objective

The objective of this research is to analyze the viability of a blood glucose sensing system based on the measurement of the shift of the resonant frequency of an antenna patch operating in the 5.8GHz ISM band (5.725 – 5.875 GHz). The ISM band is approved by the FCC for medical application and is therefore an ideal portion of the frequency spectrum to utilize for this application. This research analyses blood glucose sensing via an implantable active sensor, an implantable passive antenna sensor, and a non-invasive sensor by simulating the anticipated performance in ANSYS EM15.0 HFSS™, an electromagnetic field simulator ideally suited for this application. Experimental tests for the most promising sensing method are conducted using oil-in-gel human tissue phantoms which was found in the literature to be the most practical way to simulate blood glucose variations in human blood.

### 1.4 Research Background

In a study conducted at the University of Alabama Birmingham Children's Hospital, an antenna operating between 500 MHz and 20 GHz showed a correlation between blood glucose concentration and the dielectric constant and electrical conductivity of the blood [27]. This was modelled using a single pole Cole-Cole equation. Different blood samples were collected and manipulated in-vitro to analyze the blood glucose dependency. Based on this study, it was clear that implantable and non-invasive systems need to undergo further research considering the effect of other human tissues such as skin, fat and muscle.

An in-vitro demonstration of a biocompatible SiC antenna designed at 10 GHz, proposed to be implanted inside the body in the fatty tissue near a blood vessel, was reported by Dr. Afroz of our research group at USF. The system was simulated using synthetic and pig blood, and a shift of 40 MHz and 26 MHz, respectively, was observed during in-vitro trials for a blood glucose variation between 120 to 530 mg/dL [23] [28]. However, the operating frequency used in these experiments (X-band) is not suitable for medical purposes, and the in-vitro setup did not mimic

realistic human tissue surrounding the antenna under test; a planar blood layer, not blood vessels, were used which are limited in their applicability to the real-life application.

In another study, a non-invasive blood glucose monitoring system was proposed using two patch antennas radiating across a human tissue and blood setup, and operating at a frequency of 60 GHz. The insertion loss,  $S_{21}$ , was found to vary according to the glucose concentration in water solution tests [29], demonstrating further evidence of the potential of realizing a non-invasive glucose sensor. The current research differs by investigating the return loss,  $S_{11}$ , of the antenna sensor patch operating at 5.8 GHz (ISM band).

In an experiment conducted to measure the complex permittivity for non-invasive RF-microwave blood glucose sensing using a glucose-water solution of 1 - 4 g/dL glucose/water in 50 $\mu$ l of deionized water, a shift in resonance frequency was observed. When tested in the physiologically important 100 - 500 mg/dL range, no clear shift of resonance frequency was recorded as the variation in the permittivity,  $\epsilon_r$ , was too low [30]. The present research differs in that the permittivity of the glucose-water solution in [30] ranged between 68 - 80 for the frequency range 1 - 8GHz, while the present research is based on the real blood glucose level  $\epsilon_r= 52.5$  at the frequency of 5.8 GHz and uses a human tissue model.

A single patch antenna model was proposed in [31] using an oil in water tissue mimicking phantom over the frequency range from 0.3 - 20 GHz using a patch resonator operating at 2.4 GHz in the ISM band. The results of this research were similar to the research in [10], where two antennas, wideband and narrowband, were designed to be sensitive to the dielectric variations of the blood when placed in proximity to the human body. In a simulated layered tissue model, the antenna's resonant frequency increases with an increase in glucose. The current research differs from [31] and [10] in that the human tissue model was used as a general approximation, and thus does not pertain to any specific location of the body. In addition, the blood was simulated and/or mimicked as a layer covering the entire surface of the phantom area rather than as a vessel approximation which is closer to the human body situation.

## 1.5 Contributions of Dissertation

The dissertation contributes in the following aspects:

- 1) Use of a finite blood vessel to mimic the human body, not a planar blood layer as in previous studies.
- 2) Analysis of implantable antenna for passive and active sensing of blood glucose in the abdominal thorax area by simulations in ANSYS EM15.0 HFSS™.
- 3) Analysis of non-invasive sensing of blood glucose in the upper arm area by ANSYS EM15.0 HFSS™ and experimental measurements using oil-in-gel phantoms. The analysis determines a) the effect of lateral displacement of antenna from the blood vessel on the results, b) the effect of the vertical elevation of the antenna sensor from the outer surface of the skin, and c) the effect of other variations due to skin thickness variations, blood vessel depth, and thickness variation of the fat.
- 4) A calibration system for optimal antenna sensing location is proposed that uses three antennas in a diagonal position from each other.
- 5) A sensing system platform for measurement of blood glucose levels based on the non-invasive results of simulation and experimental antenna patch sensing in the upper arm area.

## 1.6 Dissertation Summary and Organization

The dissertation is organized into five chapters. Chapter 1 presents an overview of glucose monitoring, a review of existing approved self-monitoring glucose systems with their associated challenges, and presents the motivation of this research as an alternative for a self-monitoring glucose system. This chapter provides the problem statement, the research objective, the positioning of the research within the field of glucose sensing, the contributions made to this field and the dissertation organization.

Chapter 2 gives an overview of the background information necessary to develop an RF blood glucose sensing system. A human tissue model is presented based on human tissue physiological and electrical properties for the abdominal area for the implantable active and passive alternatives and for the upper arm area for the non-invasive alternative. This chapter presents simulations for active and passive antenna sensors followed by the non-invasive antenna simulations for ideal conditions.

Chapter 3 concentrates on the non-invasive sensing model, analyzing the effect of misalignment of the antenna which includes shifting the antenna sideways away from the blood vessel, and variations when the antenna is elevated above the skin from a reference 2 mm above the skin position. Further simulations analyze variations due to skin thickness increase/decrease and vein location depth. Experimental results are presented for the non-invasive sensing model and analyzed in comparison with the simulation results. An antenna alignment calibration strategy is presented to improve system accuracy.

Chapter 4 is an overview of a complete non-invasive blood glucose system. It presents a blood glucose system and an electronic system platform to automatically compute the measured shift in resonance frequency caused by variations in glucose levels digitally. The dissertation finally concludes with Chapter 5 which summarizes the research during the dissertation and presents future work which may be pursued to further demonstrate/improve the non-invasive glucose measurement system described in this dissertation.

## CHAPTER 2: RF GLUCOSE SENSING

This chapter presents background information necessary for the design of a human tissue model, including the electrical parameters and physiological considerations for the implantable active antenna sensing model, implantable passive antenna sensing model and non-invasive antenna sensing model. The chapter presents an electromagnetic simulation tool for simulations of the antenna in free space, followed by simulations of the antenna embedded in human tissue for both active and passive sensing, and ending by an antenna externally located facing human tissue for non-invasive sensing.

### 2.1 Overview of Antenna Glucose Sensing Models

#### 2.1.1 Implantable Active Sensing

In the implantable active sensing case, displayed in Figure 1, the antenna acts as an active sensor. In this case, internal electronic circuitry and a power supply are needed for operation of the glucose sensing system. This case could be ideal for a future implantable glucose sensor that also automatically dispenses insulin in real time.

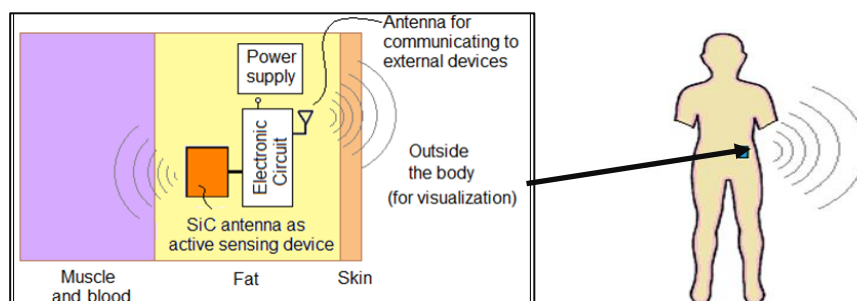


Figure 1: Active sensing antenna implanted in abdominal area configuration. Implant requires circuitry and power supply. Reprinted with permission from [32] © 2016 [MRS]

<sup>1</sup>A partial section of this chapter (text and figures) was published in MRS conference paper *SiC RF Sensor for Continuous Glucose Monitoring* © 2016 [MRS]. Permission is included in Appendix A.



### 2.1.2 Implantable Passive Sensing

In the implantable passive sensing model, as displayed in Figure 2, the antenna is implanted in fatty tissue and two additional external antennas (a transmitting and a receiving antenna) are required. The transmitting antenna sends a signal towards the implanted antenna, which is reflected to the receiving antenna by the implanted sensor and thus 'reads' the sensor's resonance frequency. External circuitry records any glucose-induced changes in the implanted sensor's resonance frequency in addition to generating the required waveform.

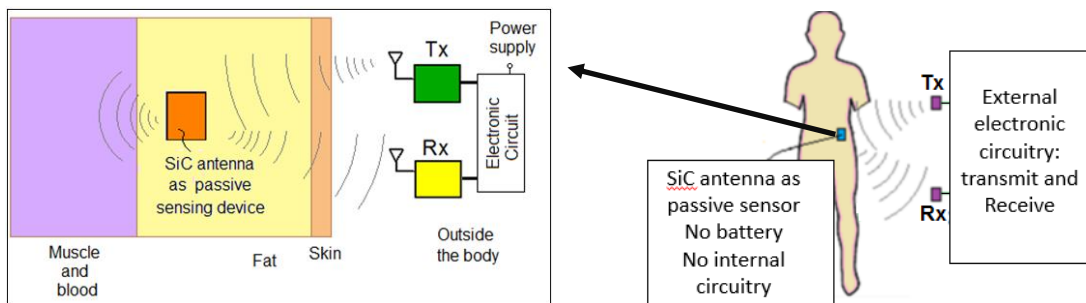


Figure 2: Implanted passive sensing antenna and external antennas configuration. The antenna implanted in the body does not require power supply or additional internal circuitry. External transmit and receive antennas interrogate the passive sensor. Reprinted with permission from [32] © 2016 [MRS]

### 2.1.3 Non-Invasive Sensing

A non-invasive solution would be much more convenient for the patient, would not require surgery, and lower power WiFi communication would be allowed due to no signal attenuation in human tissue. Figure 3 displays an antenna patch located above the upper arm. The antenna and the external circuitry are located outside the body.

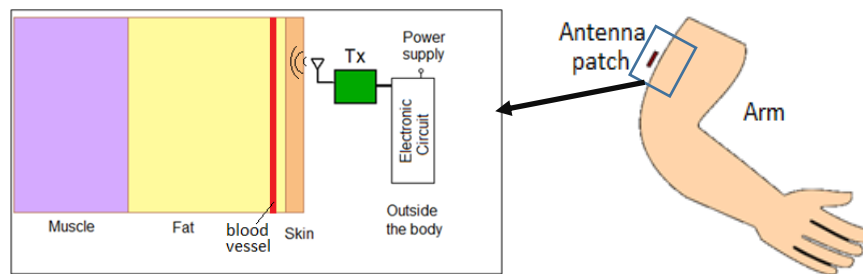


Figure 3: Non-invasive sensing antenna on top of the arm configuration. The antenna and the electronic circuitry are located outside the body. The antenna is placed in direct line of sight with a major vein.

## 2.2 Glucose Dependent Properties of Blood

### 2.2.1 Permittivity and Conductivity of Blood

The concept of an implantable antenna being used as a glucose sensor is based on the principle that the medium that surrounds an antenna affects parameters such as input impedance and resonance frequency of the antenna due to glucose-dependent changes in blood permittivity and conductivity. In the context of electromagnetism, permittivity is a measure of the resistance encountered in the medium when forming an electric field. In other words, permittivity gives a measure of the material's ability to allow an electric field to be transmitted (or stored). The dielectric constant of a material is the ratio of the permittivity of a substance to the permittivity of free space. When exploring effects of any medium on electromagnetic waves, one can explain the basis in terms of a frequency-dependent complex relative permittivity given by the formula:

$$\epsilon = \epsilon' - j\epsilon'' \quad (1)$$

where the real part of the permittivity,  $\epsilon'$ , defines the amount of electromagnetic energy stored in a material relative to the amount stored in vacuum; and the imaginary part,  $j\epsilon''$ , defines the loss factor or dielectric losses. This second term can also be expressed in terms of the material conductivity as:

$$\epsilon'' = \sigma / \epsilon_0 \omega \quad (2)$$

where  $\sigma$  is the electrical conductivity of the material [33].

### 2.2.2 Blood Glucose Dependent Experiments

In an experiment conducted at the Pukyong National University and Kyungpook National University, South Korea, it was observed that the real ( $\epsilon'$ ) and imaginary ( $\epsilon''$ ) dielectric constants of blood increases as the glucose levels in the solution decreases [34]. The experiment was conducted on a hamster tail, where a correlation between blood glucose and  $\epsilon'$  at a frequency of

10 kHz was observed, while further experiments showed also a frequency and time dependence for the results. The data collected resulted in the glucose dependence shown in Figure 4 below.

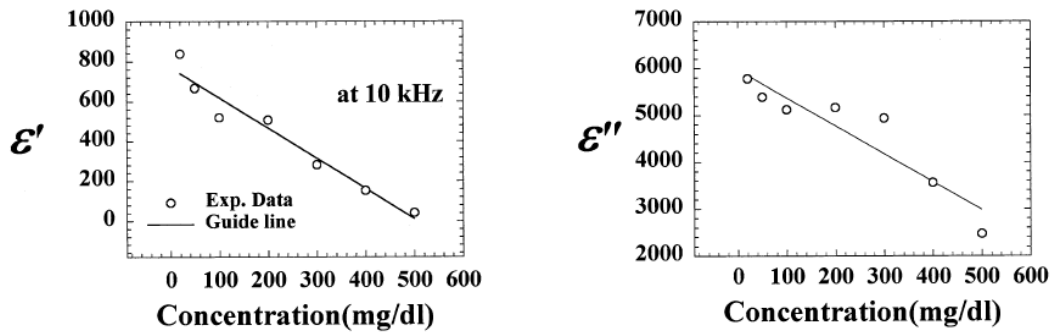


Figure 4: Water/glucose concentration dependence of the dielectric constant. Graph shows the real ( $\epsilon'$ ) (left) and the imaginary ( $\epsilon''$ ) part of equation (1) (right) at 10 kHz. Reprinted from [34] © 2003, with permission from Elsevier.

Furthermore, the effects of sugar and salt on  $\epsilon'$  and  $\sigma$  were investigated with a skin-mimicking gel, where the frequency dependence of the dielectric and conductivity constants are shown in Figure 5 and Figure 6. Either sugar or salt was varied. As can be observed, the added sugar, while keeping the salt constant, decreases the relative permittivity significantly, and increases to a smaller degree the conductivity. Also, the added salt, while keeping the sugar constant, decreases the relative permittivity to a small degree, and increases the conductivity significantly.

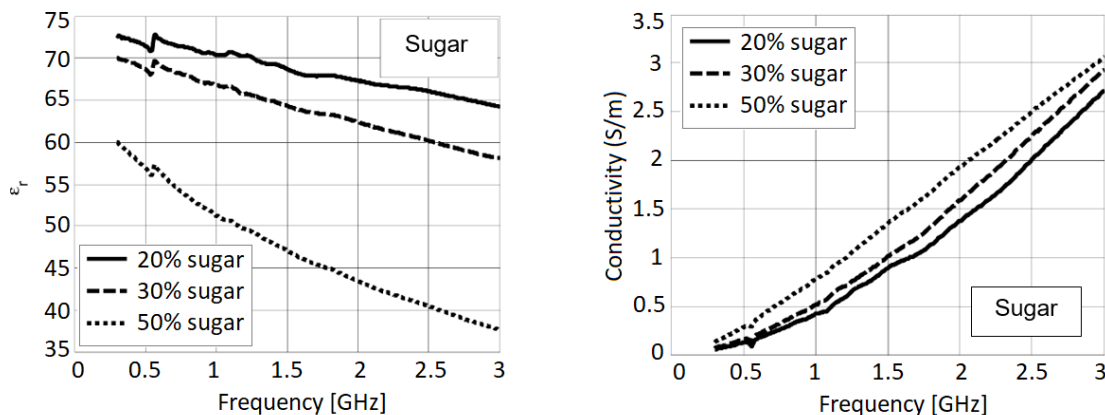


Figure 5: Frequency dependence in blood gel as a function of sugar. Permittivity dependence (left) and conductivity dependence (right) © [2008]IEEE. Reprinted from [35] with permission grant found in Appendix C

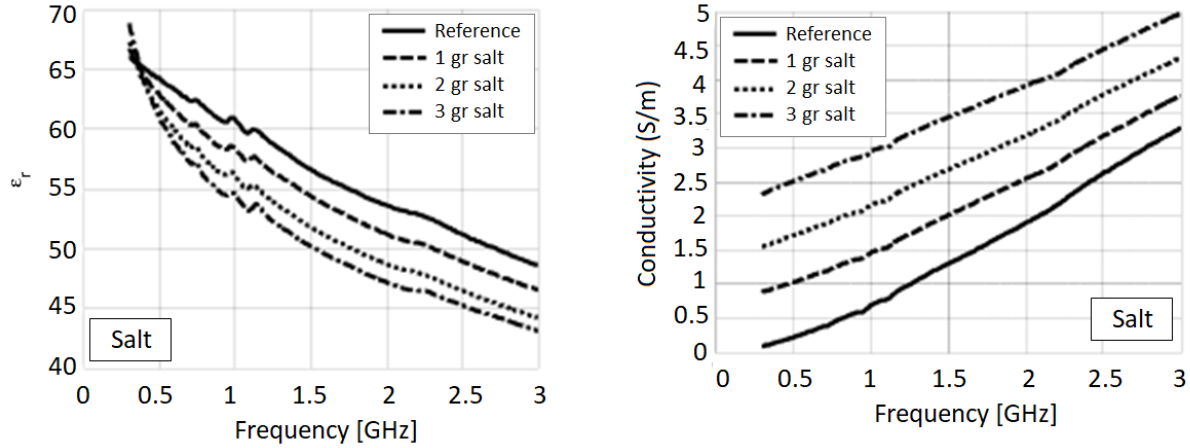


Figure 6: Frequency dependence in blood gel as a function of sugar. Permittivity dependence (left) and conductivity dependence (right) © [2008]IEEE. Reprinted from [35] with permission grant found in Appendix C

Human blood can be characterized by the Debye formula:

$$\varepsilon^* = \varepsilon_\infty + \frac{\Delta\varepsilon}{1+i2\pi\nu\tau} \quad (3)$$

or from an extension in the Havriliak-Negami formula:

$$\varepsilon^*(\nu) = \varepsilon_\infty + \frac{\Delta\varepsilon}{[1+(i2\pi\nu\tau)^{1-\alpha}]^\beta} \quad (4)$$

from which the Cole-Cole model, where  $0 \leq \alpha \leq 1$  and  $\beta=1$ , can be formulated [36].

Using in-vitro human blood samples, the dielectric properties of blood were correlated to blood glucose using a modified Cole-Cole model [10]. In a study conducted by Topsakal et al. at the University of Alabama Birmingham, the permittivity and conductivity of blood plasma was measured in-vitro at different glucose levels from 0 mg/dl to 16000 mg/dl over a frequency range from 500 MHz to 20 GHz. The results in Figure 7 display the relative permittivity and shows that it is decreases as the frequency increases [27]. That is as the glucose levels increase, the permittivity decreases. The results in Figure 8 [27] indicate that the electrical conductivity increases as the frequency increases. Notice that, for lower frequencies, there is no significant variation in the conductivity as the glucose level increases. For frequencies close to 10 GHz, the conductivity decreases for higher frequency with the glucose levels.

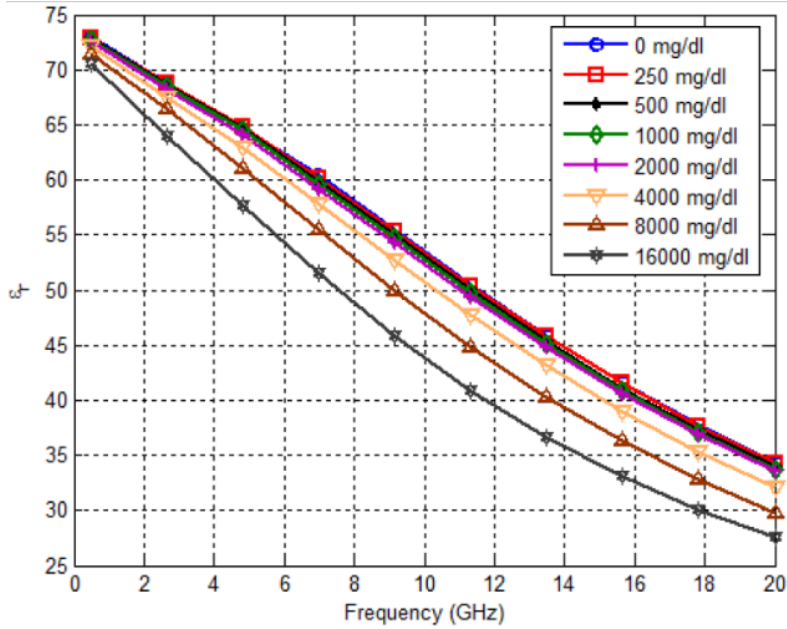


Figure 7: Relative permittivity of blood plasma vs. glucose levels concentration  
 © [2008] IEEE. Reprinted from [27] with permission grant in Appendix C

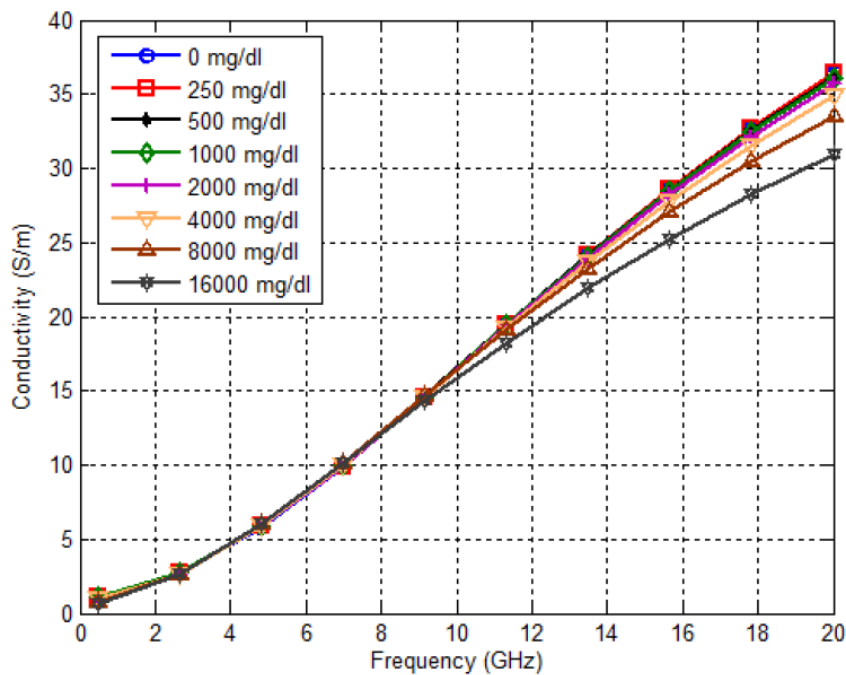


Figure 8: Electrical conductivity of blood plasma vs. glucose levels concentration.  
 © [2008] IEEE. Reprinted from [27] with permission grant in Appendix C

Overall, experimental tests have shown that variations in blood glucose change the permittivity and conductivity of the medium, indicating that an implantable antenna has a great

sensing potential, as its characteristics change directly with these changes in the surrounding medium, where the medium in the application is the blood glucose.

### 2.2.3 Sensing of Blood Glucose Levels with a 10GHz SiC Antenna

In tests conducted by Afroz et al. on a 10 GHz Silicon Carbide (SiC) based Ti/Au patch antenna, it was shown that the resonant frequency of the antenna shifts as a function of glucose level, as obtained based on in-vitro experimentation using synthetic blood fluid (SBF). A change from 120 mg/dl to 530 mg/dl of blood glucose resulted in a 40 MHz shift that was fairly linear. Assuming a linear change versus glucose concentration this translates to a shift of 97 KHz for every 1 mg/dL change in blood glucose. Using a Vector Network Analyzer (VNA), the return loss,  $S_{11}$ , of the sensing antenna was measured. Using this method, it is easy to see the resonance frequency of the antenna as this is the point where a minimum in RF signal energy is reflected back to the VNA. Additional experiments using pig blood samples displayed a similar behavior. The  $S_{11}$  response using synthetic blood and pig blood as a function of glucose level is shown in Figure 9. A comparison of the relative resonance frequency shift using synthetic blood and pig blood samples is displayed in Figure 10 [28] [23].

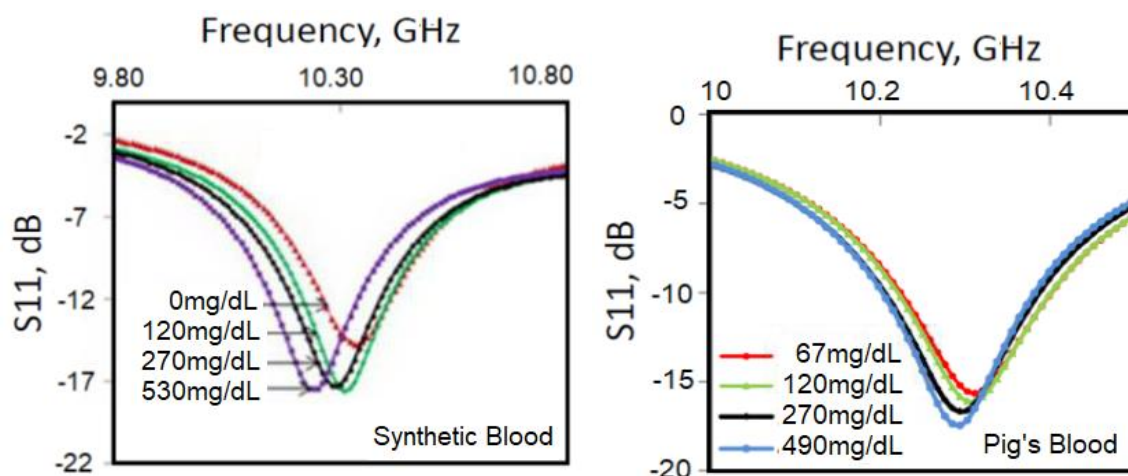


Figure 9: Return loss of a 10GHz antenna for various blood glucose concentration. Measured in synthetic blood (left) and pig blood (right) for (a) 67 mg/dl, (b) 120 mg/dl, (c) 270 mg/dl, (d) 490 mg/dl [23]. Note that  $f_0$  shifts to lower frequency as the glucose concentration increases. © [2008]IEEE. Reprinted from [28] with permission grant in Appendix C

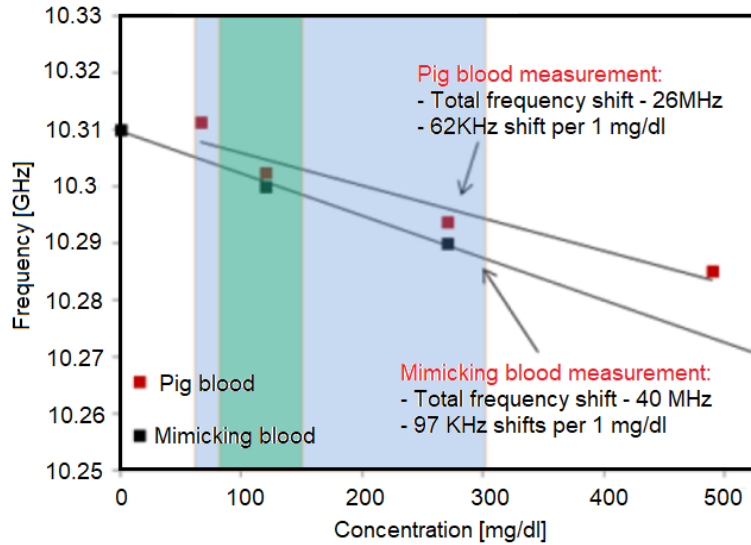


Figure 10: Resonance frequency vs. glucose concentration of a 10 GHz SiC antenna. The colored regions denote healthy (green) and unhealthy (blue) levels of blood glucose in humans and was added for reference. Note the roughly linear change in  $f_0$  vs. frequency. Trend line is a least-squares fit of the measured data © [2008]IEEE. Reprinted from [28] with permission grant in Appendix C

## 2.3 Human Tissue Models

### 2.3.1 Electrical Parameters for Each Human Tissue

The electrical parameters for human tissue used in this research were established using [37], which is based on the parametric model for the calculation of the dielectric properties of body tissues [33, 38]. Table 2 shows the conductivity and permittivity for human tissues of interest.

Table 2: Conductivity and permittivity of human tissues at 2.4, 5.8 and 10GHz [37].

Human Tissue	Conductivity			Permittivity		
	2.4GHz	5.8GHz	10GHz	2.4GHz	5.8GHz	10GHz
Wet Skin	1.5618	4.342	8.951	42.923	38.624	33.528
Fat	0.10235	0.29313	0.58521	5.2853	4.9549	4.6023
Blood	2.5024	6.5057	13.131	58.347	52.539	45.109
Muscle	1.705	4.9615	10.626	52.791	48.485	42.764

As the frequency increases, the permittivity value decreases and the conductivity value increases. The permittivity of fatty tissue is much lower than the permittivity of muscle, being an additional reason why the sensor is proposed to be implanted in the fatty area (i.e., less antenna

loading from the surrounding tissue). At the selected frequency of 5.8 GHz, the permittivity of muscle is 48.485, while for fatty tissue, it is 4.9549. To define the electrical properties of blood, the calculations by [27] and [39] were used in the models for implantable active sensing and non-invasive sensing along with the values provided in Table 2 [33, 40, 37].

## 2.3.2 Human Tissue Model for Active and Passive Implantable Sensing

### 2.3.2.1 Location in Human Body

In-vitro experimental results with a 10 GHz 4H-SiC based antenna placed under both muscle and fat concluded that the best implant location is in the fatty tissue layer [23]. The simulations for the active and passive implantable sensor were modelled within the fatty tissue layer of the abdominal area as displayed in Figure 11, which displays a front abdominal area cross view and the proposed location of the sensor implant (blue bar on left side of image). This follows the current guidelines for needle insertions, which avoid the areas around the belly button and the areas where the body naturally bends [41]. The simulation considered that the implant would be within the fatty tissue layer in proximity of the superficial epigastric vein, due to veins being less muscular than arteries and located closer to the surface of the tissue than arteries. The implanted patch antenna would be facing the muscle and blood. Included in the model are the skin, fat, muscle and blood.

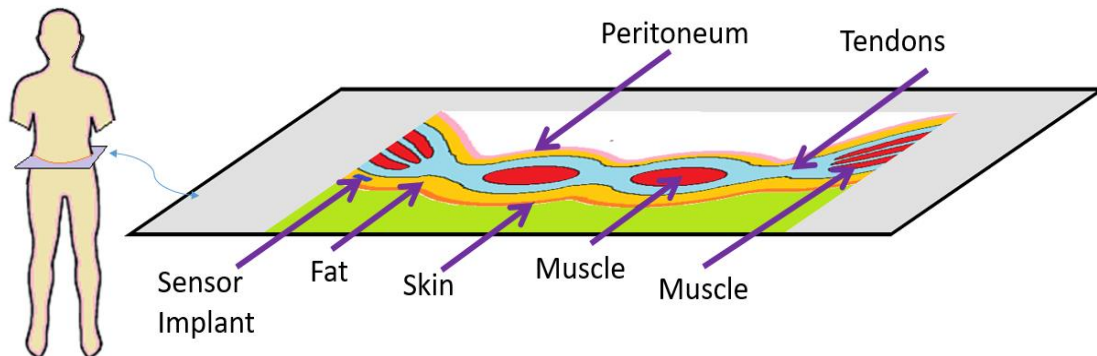


Figure 11: Proposed implant position in the fatty area of the front abdominal wall. Front wall of the abdomen horizontal cross-section view. The sensor implant is displayed as a blue bar to the left in the fat layer.



### 2.3.2.2 Thickness Approximations of Human Tissue

Based on the evaluation of glucose levels from adults with diabetes and diverse demographic backgrounds, the average skin thickness is 2.2 mm [40]. The average abdomen subcutaneous adipose layer thickness, which will be referred to by its common term as fat, was 13.9 mm in the abdominal area, ranging from 13.2 mm to 17.7 mm [40]. In a study to characterize changes in muscle thickness in the transverse abdominis (TrA) and internal oblique (IO) muscles during common exercises, the muscle thickness was obtained at rest with the subjects in the supine position with their knees bent at 90°. The average transverse abdominis muscle was  $0.50 \pm 0.11$  mm thick for males and  $0.43 \pm 0.11$  mm for females, and the average thickness for the internal oblique muscle was  $1.09 \pm 0.23$  mm for males and  $0.73 \pm 0.16$  mm for females [42]. There is an increase in the thickness of the transverse abdominis and the internal oblique related to the type of exercise being executed, in thickness ratio (contracted/rest ratio) that ranges from  $1.88 \pm 0.52$  to  $1.118 \pm 0.22$  [42].

### 2.3.2.3 Human Tissue Model for Implantable Sensing

Figure 12 shows a human tissue model for implantable sensing used for the implantable active sensing, as is, and for the implantable passive sensing by adding the external antennas in the air section (not shown for clarity).

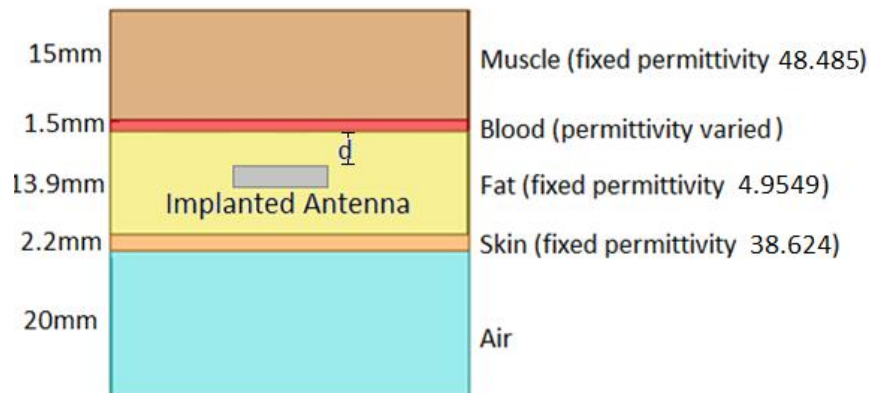


Figure 12: Human tissue model for implant showing the thickness and  $\epsilon_r$  of each layer. The antenna position is shown at a distance  $d$  from the blood layer. (Drawing not to scale).

### 2.3.3 Human Tissue Model for Non-Invasive Sensing

#### 2.3.3.1 Location in Human Body

The location for the proposed non-invasive sensing approach is the upper arm location, in direct line of sight of the cephalic vein, as displayed in Figure 13.

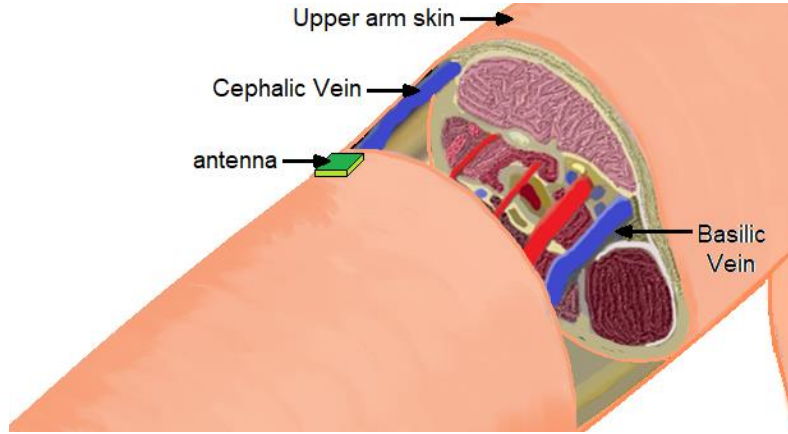


Figure 13: Antenna patch location over the arm showing cross sectional anatomy. The target blood vessel is the Cephalic vein due to its proximity to the skin. The figure is adapted from a video from The New England Journal of Medicine [43], © Massachusetts Medical Society. Permission grant found on Appendix E.

#### 2.3.3.2 Thickness Approximations of Human Tissue

The skin mean thickness for adults 25 years and older is 2.48mm for males and 2.4mm for females while the mean arm subcutaneous thickness is 9.07mm for males and 12.01mm for females [44]. For purposes of the simulations, the thickest rounded value for skin and subcutaneous thickness were selected.

Two possible veins were evaluated: the cephalic and the basilic veins, both being large superficial veins located in the upper limb. The network of veins varies person to person, and thickness varies from different arms and different sections. The following measurements of average basilic and cephalic vein diameter were used for the thickness values of the human arm model. The cephalic vein has an average diameter of 1.8mm located in the superficial fascia on the surface of the biceps brachii muscle [45]. The basilic vein is located deeper normally perforating the deep fascia above the medial epicondyle. In Brazilian cadavers, the average

diameters are shown in Table 3 [46]. Although the diameter of the basilic vein is more suitable for testing, due to the deeper location of the vein, the cephalic vein was chosen for the model used in this research.

Being that the cephalic vein was selected for the model, the muscle is based on the bicep's brachii muscle. This muscle varies from gender and the bodybuilding level of the individual. In a study conducted taking the cross sectional area of the biceps of 585 subjects (342 males and 243 females), the average cross sectional area of the bicep was  $22.2\text{cm}^2$  for males and  $14.0\text{cm}^2$  for females [47]. Another study, which aimed to study the muscle thickness changes following bench pressing training, found the average thickness to be 25.1mm for males aged 25 years [48]. In a study by Miyatani et al. comparing the measurement taken by ultrasound and by magnetic resonance imaging (MRI), the bicep muscle thickness for males ages 23 to 40 was found to be an average of 33mm when measured by ultrasound and 32mm when measured by MRI [49]. When structuring the arm tissue model, other factors were considered such as lower muscle thickness for females, as well as arm position and movement that affect muscle tension, and age. These were all implemented as variables. The muscle thickness used in the model was 25mm.

Table 3: Human arm model physical dimensions.

Human Tissue	Measure [mm]	Description		Model
Skin	2.48	Thickness for male		2.48mm
	2.4	Thickness for female		
Fat	9.07	Thickness for male		12.01mm
	12.01	Thickness for female		
Cephalic Vein	1.8	Mean diameter		1.8mm
Basilic Vein	1.90±0.63	Right arm	at the fold of the cubicus.	Not used
	2.24±0.73	Left arm		
	3.26±1.15	Right arm	at midpoint fold	
	3.46±1.41	Left arm		
	4.96±1.84	Right arm	Inferior border of the teres major muscle.	
	5.09±1.28	Left arm		
Biceps muscle	32-33mm	Average thickness for male 23-40 years old		25mm
	25.1mm	Average thickness following bench pressing male age 25		

### 2.3.3.3 Human Tissue Models for Non-invasive Sensing

Based on the human tissue physiology presented, the human tissue model for non-invasive sensing was setup as a layer of skin on top of a layer of fat and then a layer of muscle. Within the fat layer a cylindrical tube represents the target blood vessel. The dimensions were set according to Table 3. The model was used in all simulations for non-invasive blood glucose sensing, and will be referred to as the complete human tissue model (HTM). The top view and side views of the model are displayed in Figure 14. The simulations for non-invasive blood glucose sensing system are also later repeated using a simplified human tissue model (SHTM), in which the skin and muscle layers are disregarded, and only blood vessel and fat are taken into consideration, to determine the effect these layers on the results. The side views of this second model are displayed in Figure 15.

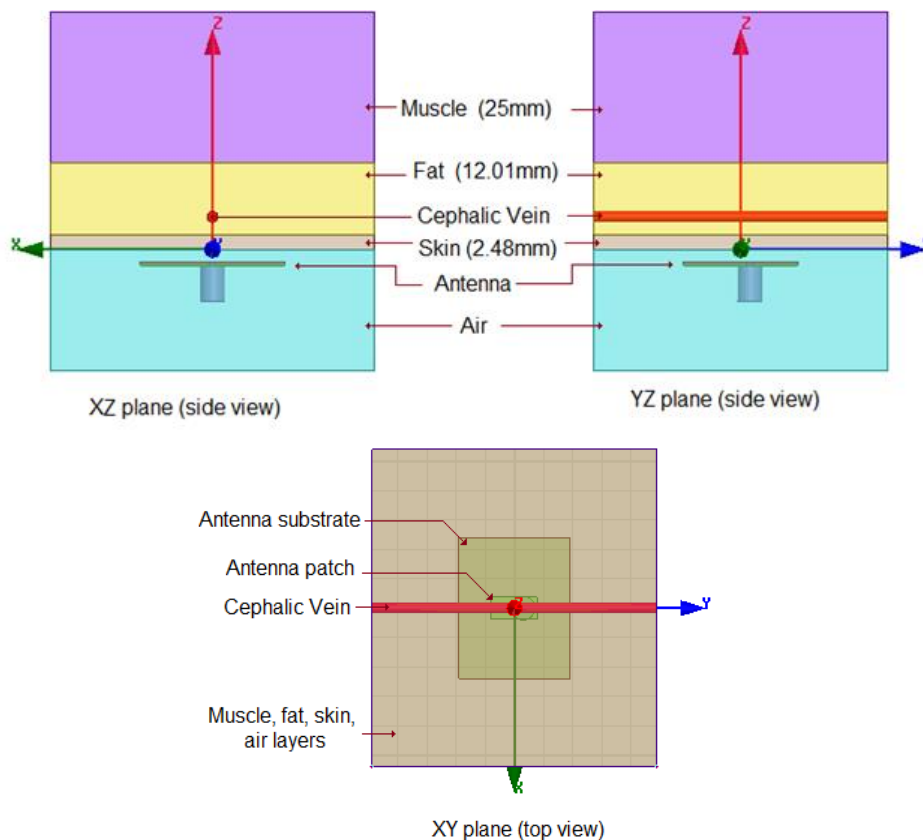


Figure 14: Complete human tissue model for non-invasive sensing simulations. Side view in the XY (left top), YZ (right top) plane and top view (bottom) showing antenna above the HTM. Antenna spacing above the arm tissue model was 2 mm.

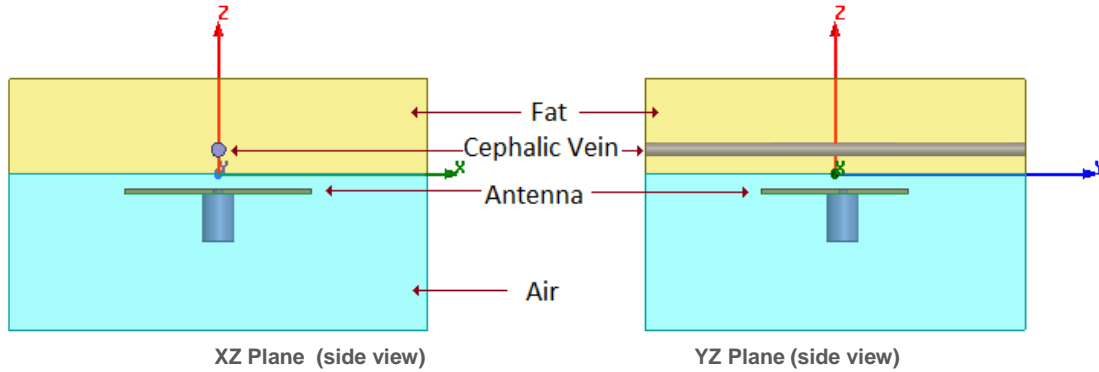


Figure 15: Simplified human tissue model for non-invasive sensing simulations. Side views showing the cephalic vein within the fat tissue. No skin and muscle included in this model. Left vein oriented into the plane of the paper, right parallel, as shown.

## 2.4 Electromagnetic Simulation Setup

### 2.4.1 HFSS™ Overview

High Frequency Electromagnetic Field Simulation (HFSS™) from Ansys is a finite element method solver software tool useful for simulating 3D electromagnetic structures [50]. The software can accurately characterize an antenna's performance in free space as well as its performance when modeled surrounded by the human tissue layer, and the effect of the presence of any additional antennas in close proximity. Each human tissue layer is modeled electrically with a corresponding electrical permittivity and conductivity as previously described. Details of the antenna's dimensions and design variables are described in the following chapter. The next section describes the PML (Perfectly matched layer) used in HFSS to prevent non-physical resonances during simulation and the antenna performance plot setup used during the simulations.

### 2.4.2 PML Boundaries

Perfectly matched layer (PML) boundaries were setup for each boundary layer of the human tissue model in order to absorb any EM radiation thus resulting in no, or minimal, EM reflection, from the simulation boundaries. The perfectly absorbing layer simulation is necessary

in the modeling of the glucose sensor so that no reflected waves are present in the area under study since the SiC RF antenna sensor is a resonant structure. PML Boundaries were setup with a uniform layer thickness of 15 mm, and with a propagation constant  $k = \omega\sqrt{\mu\varepsilon}$  at minimum frequency of 4 GHz. This results in the following setup according to the human tissue permittivity values reported in Table 2 result in the  $k$  constant as shown in Table 4.

Table 4: Propagation constant of each layer of human tissues

Human Tissue	Calculations for propagation constant $k = \omega\sqrt{\mu\varepsilon}$ (1/m) at 4GHz	Propagation constant k
Muscle	$k = 2\pi \frac{4 * 10^9}{3 * 10^8} \sqrt{48.485}$	583.045
Fat	$k = 2\pi \frac{4 * 10^9}{3 * 10^8} \sqrt{4.955}$	186.389
Skin	$k = 2\pi \frac{4 * 10^9}{3 * 10^8} \sqrt{38.624}$	520.387
Blood permittivity*	$k = 2\pi \frac{4 * 10^9}{3 * 10^8} \sqrt{52.539}$	606.931

\*Average blood glucose level. This was varied.

In Figure 16(a), the human tissue model is shown in 3D view without the PML layer, and in Figure 16(b) with the PML layer which was set for each tissue layer so as to absorb any stray radiation and eliminate reflections back to the sensor zone.

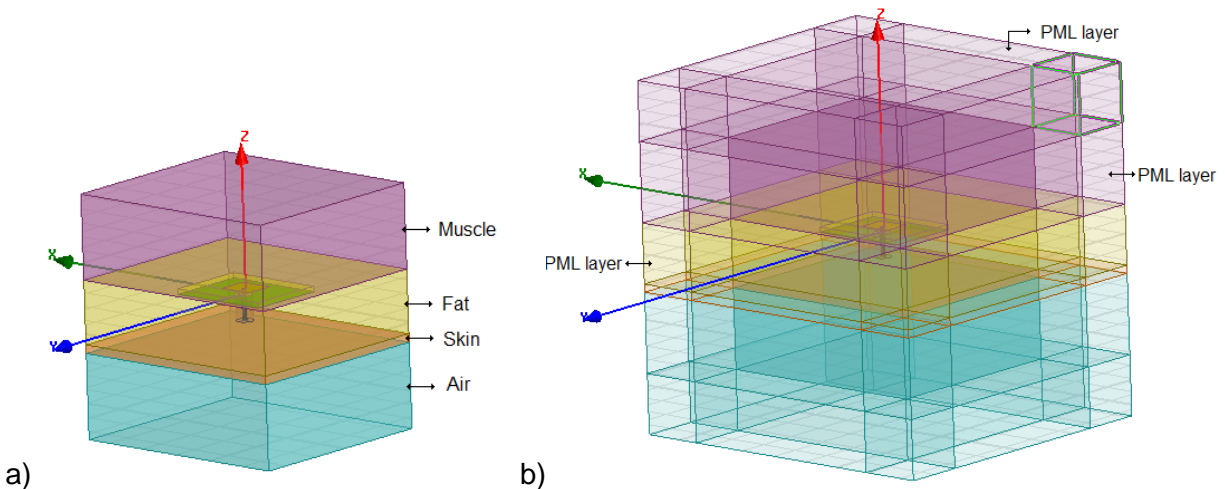


Figure 16: Human tissue model with (a) no PML boundary and b) with PML boundary.

## 2.5 Antenna Design for ISM Band (5.8 GHz) in Free Space

### 2.5.1 Antenna Design Overview

The antenna was designed using a 635 $\mu\text{m}$  thick Rogers 6010 substrate ( $\epsilon_r=10.2$ ,  $\tan \delta = 0.0023$ ). It was designed for free space using HFSS™ Antenna Design Kit for a rectangular patch antenna that is probe fed. The desired frequency of 5.8 GHz, and the characteristics of the material, were input into the software. This design was simulated in Ansoft EM15.0 HFSS™ adding the human tissue model for the implantable option and for the non-invasive CHTM and SHTM tissue models. The length, width and location of the antenna feed were gradually modified to optimize the design for the antennas implanted in the active and passive sensing models, as well as for the non-invasive mode where the antenna was found to operation best when placed 2 mm from the arm's surface.

The free-space (no tissue load) design dimensions of the antenna patch at 5.8 GHz are shown in Figure 17. The antenna design was performed to optimize the antenna's performance by varying both the patch dimensions and feed position.

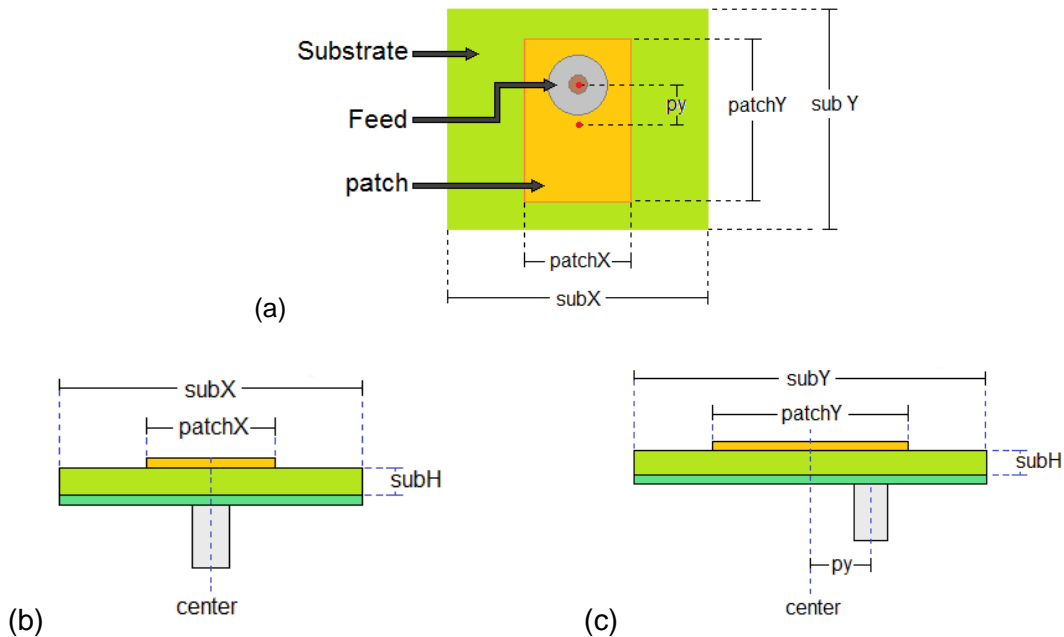


Figure 17: Schematic top and cross section views of the SiC RF antenna. (a) top view, (b) cross-section view XZ plane and (c) cross section view YZ plane.

## 2.5.2 Optimizing the Antenna to Resonate at 5.8 GHz

The antenna patch's dimensions were set to subX=2.4 cm, subY=1.9 cm, subH=10 mil, px=0 mm, patch X=8.8 mm and d=2 mm. The parameters patchY, and py, were varied one at a time to optimize the antenna resonance to 5.8GHz (i.e., minimum return loss S<sub>11</sub>). Figure 18 shows the resulting predicted S<sub>11</sub> value as the patchY parameter changes from 7 mm to 7.2 mm. This variation of the resonant frequency, in correspondence with the patchY size, is plotted in Figure 19.

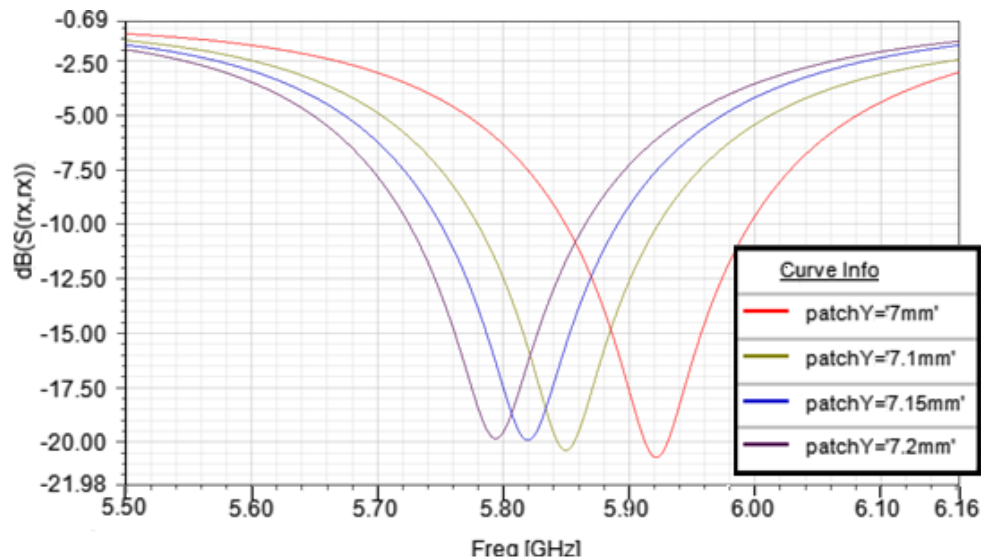


Figure 18: Simulated antenna in free space to optimize operation at 5.8 GHz. Variables are fixed at Patch X=8.8mm, px=0mm and py=1.2mm. PatchY is varied.

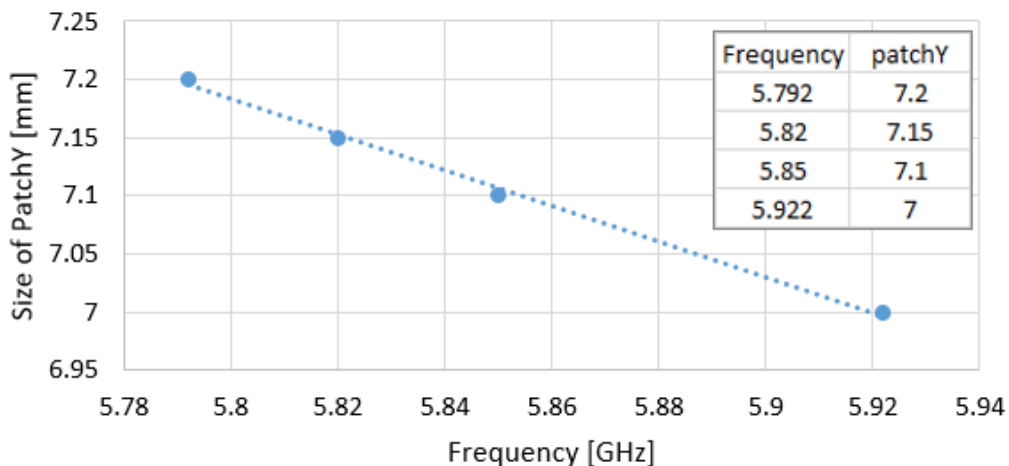


Figure 19: Plot of simulation data showing variation in  $f_0$  vs. the variable Patch Y. Dotted line is a least-squares linear fit to the data.



The parameter  $p_y$  was varied from 0 to 1.6 mm. Simulated  $S_{11}$  results are displayed in Figure 20. As the displacement of the feed increases, the  $S_{11}$  resonant frequency, gain and bandwidth increase. For instance, a  $p_y$  of 0.9mm resulted in a resonant frequency of 5.74 GHz and  $S_{11}$  of -11.9 dB. For  $p_y$  at 1.2 mm the resonant frequency increases to 5.79 GHz and  $S_{11}$  of -35.2 dB. Increasing  $p_y$  to greater than 1.2 mm results in a significant decrease in  $S_{11}$  as the displacement of the feed is located outside the dimensions of the patch. For all further trials,  $p_y$  was set to a fixed value of 1.2 mm.

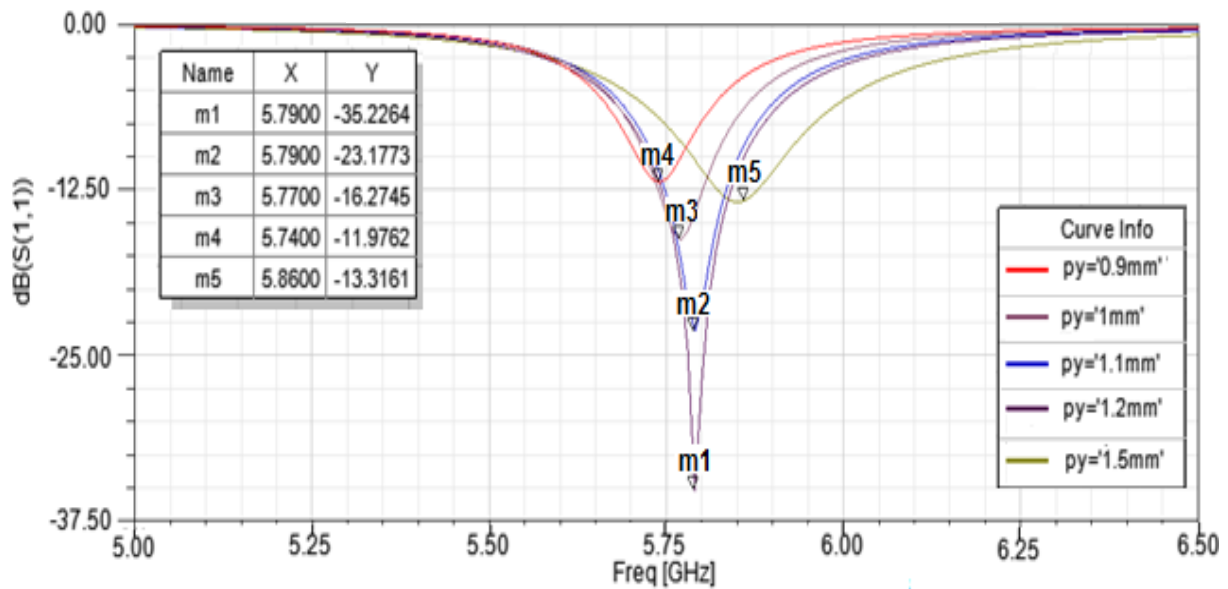


Figure 20: Simulated data showing variation of  $S_{11}$  based on the location of feed  $p_y$ . The displacement feed dimension  $p_y$  increase results in a decrease in frequency and decrease of the dB minimum peak when the value is less than or equal to 1.2mm.

The final parameters of the antenna design in free space at 5.8 GHz are displayed in Table 5. In summary, the free space antenna for 5.8GHz is designed on a 25 mil thick Duroid substrate 2.4x1.9cm with a rectangular patch 8.9 x 7.2mm. The inset feed displacement is 1.1mm in the y axis and is centered in the x axis.

Table 5: Antenna patch dimensions for free space operation at 5.8 GHz

Parameter	subX	subY	patch X	patchY	subH	px	py
Dimension	2.4 cm	1.9 cm	8.9 mm	7.2 mm	25 mil	0.0 mm	1.1 mm

The simulated value  $S_{11}$  for the antenna in free space and corresponding beam profiles can be observed in Figure 21 and Figure 22.

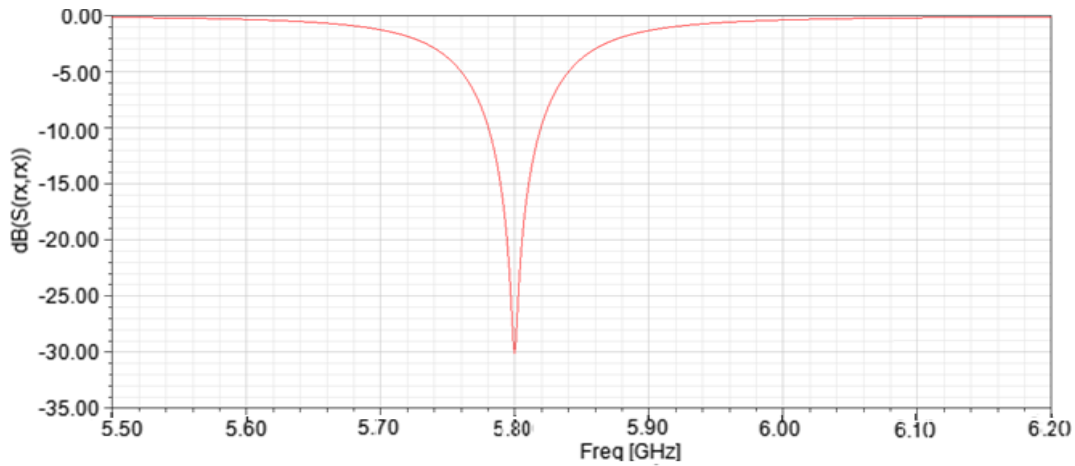


Figure 21: Final free-space antenna design showing simulated resonance at 5.80 GHz.

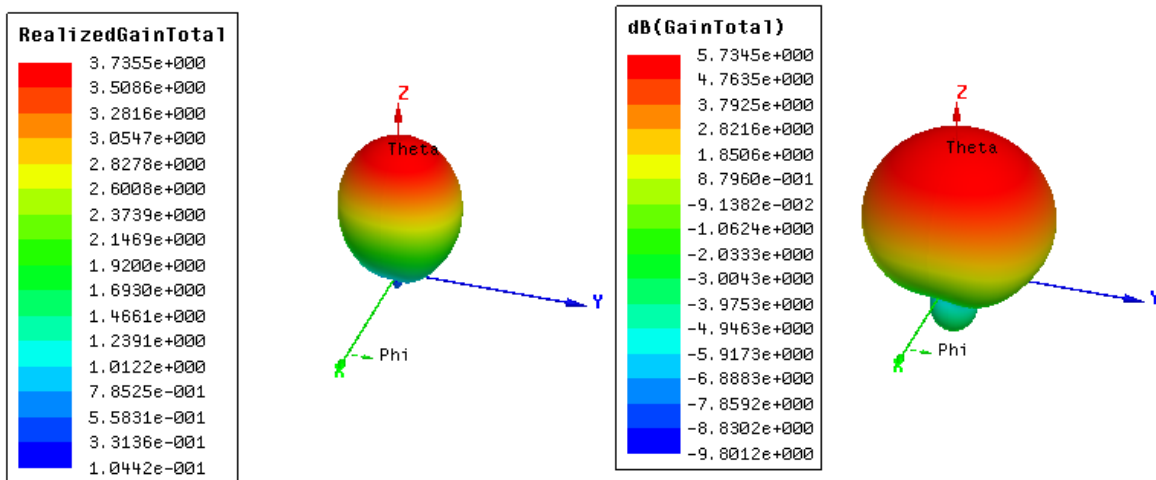


Figure 22: Simulated antenna beam profile of final optimized antenna. (a) realized gain result (left) and (b) total gain result (right)

## 2.6 Antenna Design for Active Sensing Mode

### 2.6.1 Antenna Design Overview

For the simulations presented in this section, the antenna is implanted in the fatty layer between the skin and blood/muscle with a spacing “d” as shown in Figure 12. The antenna patch is facing the blood/muscle tissues.

The average relative blood permittivity was set to 62.5 and a blood bulk conductivity of 7.5 Siemens/m was used. The other tissue values were set to the fixed permittivity displayed in Table 2. The antenna was matched to the feed by changing the location of the feed and the dimensions of the antenna following the same procedure used to optimize antenna resonance in free space. Then, the simulated blood relative permittivity was varied in steps of 0.2 from 62 to 63.6, while the bulk conductivity remained at the fixed value of 6.5 Siemens/m. The reason for this being that blood permittivity varies as the glucose levels in the blood varies, but experiences a non-significant variation in bulk conductivity [23] [10].

## 2.6.2 Antenna Matching to Tissue Environment

### 2.6.2.1 Varying the Parameter Py

The parameter  $p_y$ , which is the distance of the location of the feed from the center point ( $p_x=0, p_y=0$ ), was varied between  $p_y=1.4$  to  $1.5$ . The greater the distance  $p_y$ , the higher the resonant frequency. Also, the resonance increases and the bandwidth decreases, as can be observed from Figure 23 and Figure 24. Note that patchX was set to 4.1mm and patchY to 7.1mm.

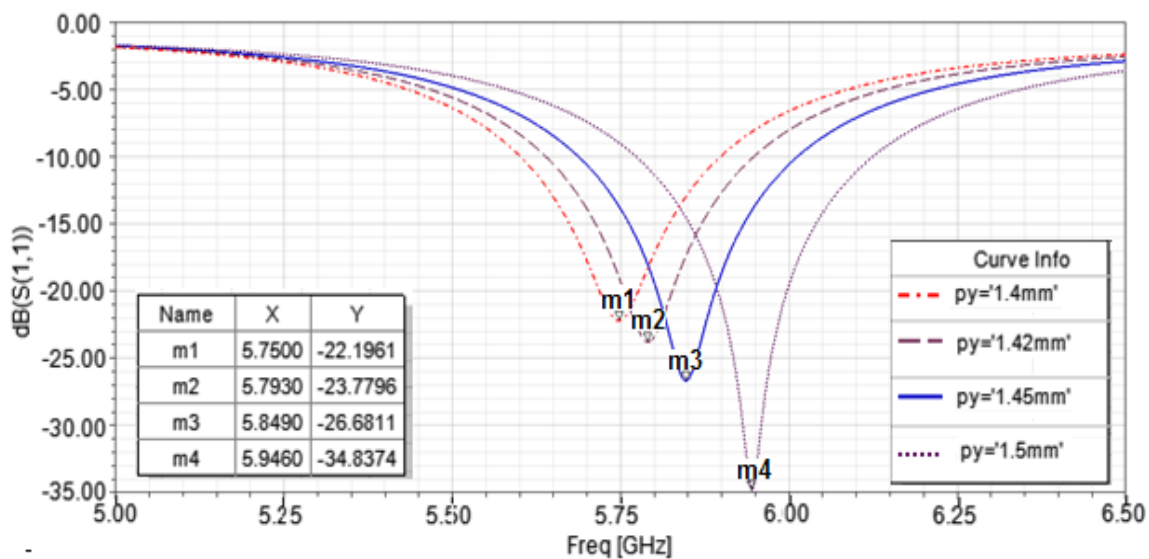


Figure 23: Return loss of active antenna based on  $p_y$  variation. Optimizing the active mode antenna by displacement of feed  $p_y$  distance.

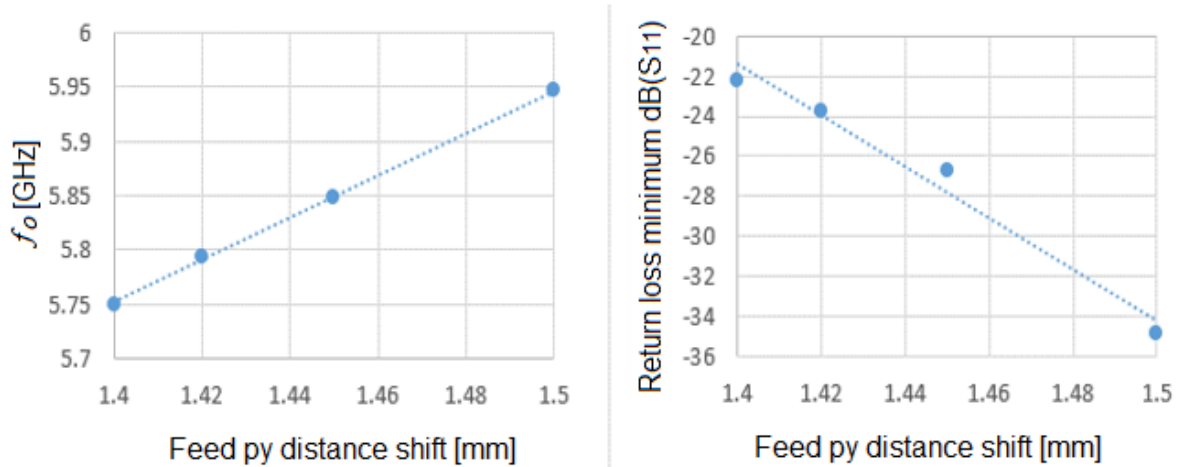


Figure 24: Resonant frequency and gain of active antenna based on py variation. (a) Variation of frequency vs. the feed py distance plot (left) and (b) variation in the gain vs. feed py distance. Trend line is a least squares fit to the data (right).

### 2.6.2.2 Variation of Parameter PatchX.

Increasing the dimension patchX increases the resonant frequency and decreases  $S_{11}$ . The parameter py was set to 1.4mm and patchX was varied from 4 mm to 4.5 mm. Figure 25 and Figure 26 show the computed return loss  $S_{11}$  versus variation in patchX. The optimized value of Patch X is 4.1 mm, as it approximates to the desired 5.8GHz and has a deeper peak than values above 4.1 mm.

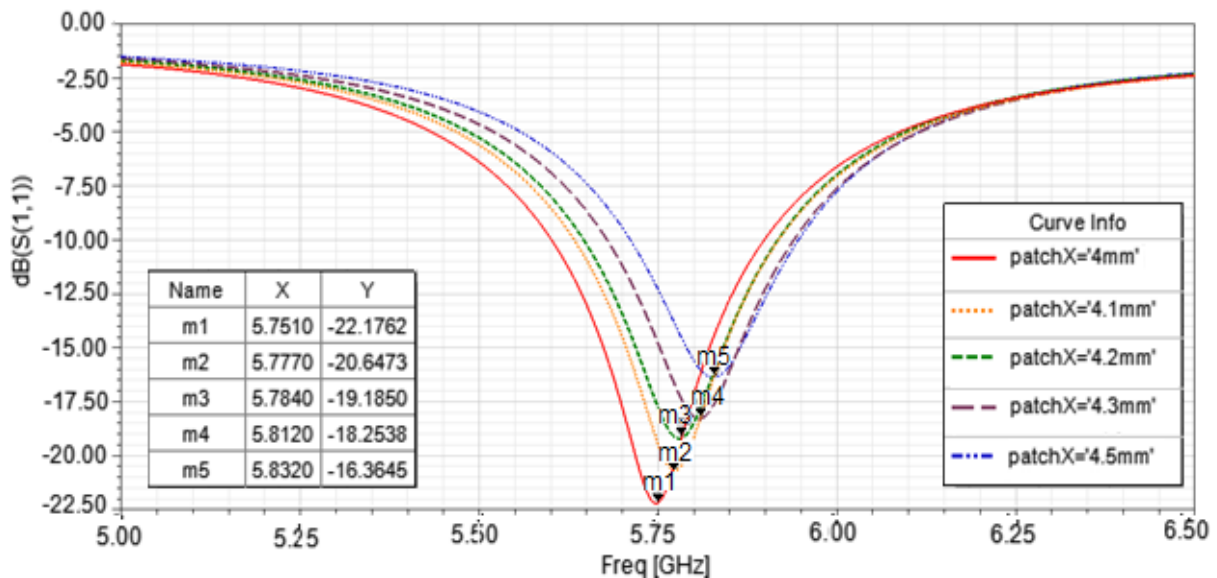


Figure 25: Return loss of active antenna based on patchX variation. The optimized value of PatchX is 4.1 mm.

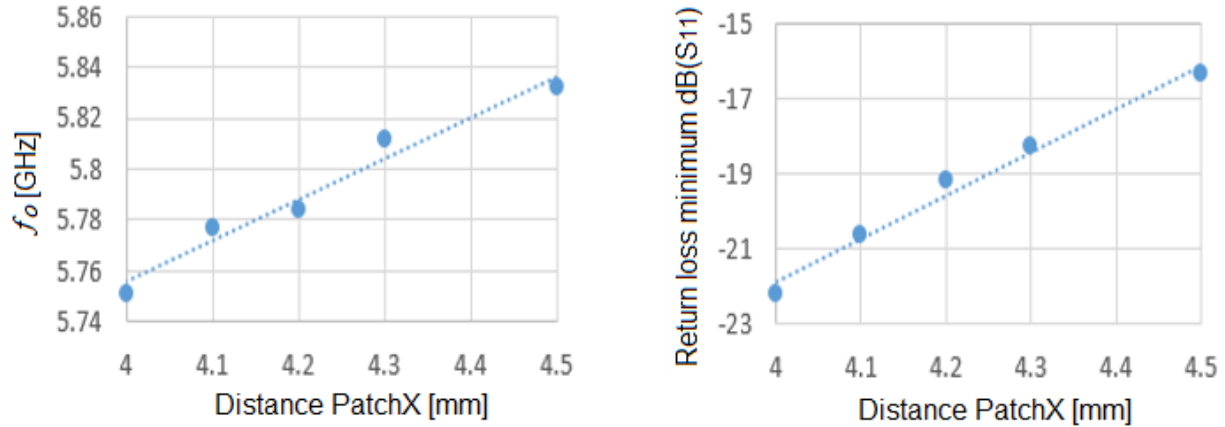


Figure 26: Resonant frequency and  $S_{11}$  of active antenna based on patch X variation. (a) Variation of frequency vs. the distance patchX distance plot (left) and (b) variation of return loss minimum vs. distance patchX distance(right). Trend line is a least-squares fit to the data.

### 2.6.3 Resulting Antenna Dimensions

Assuming a blood permittivity of 62.5 and referring to Figure 17, the antenna dimensions are as described in Table 6.

Table 6: Antenna dimensions for implantable antenna

Parameter	subX	subY	patch X	patchY	subH	px	Py
Dimension	2.4 cm	1.9 cm	4.1 mm	7.1 mm	10 mil	0.0 mm	1.4

The result of the single implanted antenna facing muscle is shown in Figure 27:

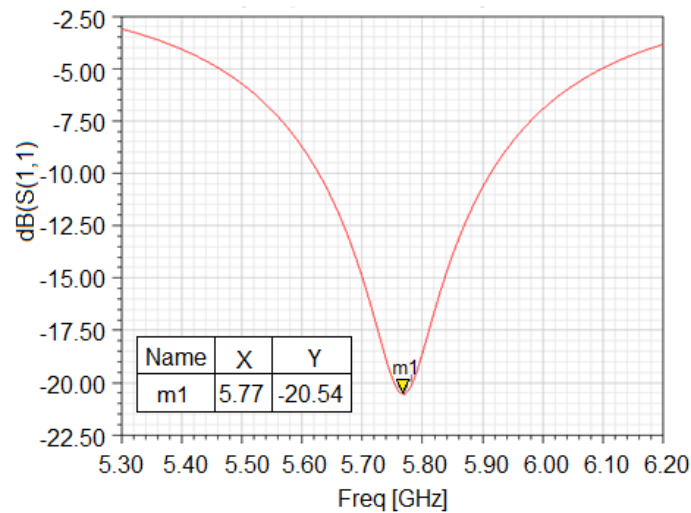


Figure 27:  $S_{11}$  of the optimized implantable antenna. Note that the resonant frequency used in this design was 5.77 GHz.

### 2.6.4 Effect of Glucose Levels in Blood

The optimized antenna in human tissue was simulated by varying the relative permittivity of blood from 62 to 63.6, while the bulk conductivity remained at the fixed value of 6.5 Seimens/m. The  $S_{11}$  results in Figure 28 show a shift in resonant frequency as the blood permittivity changes, as expected based on previous results in the literature [23].

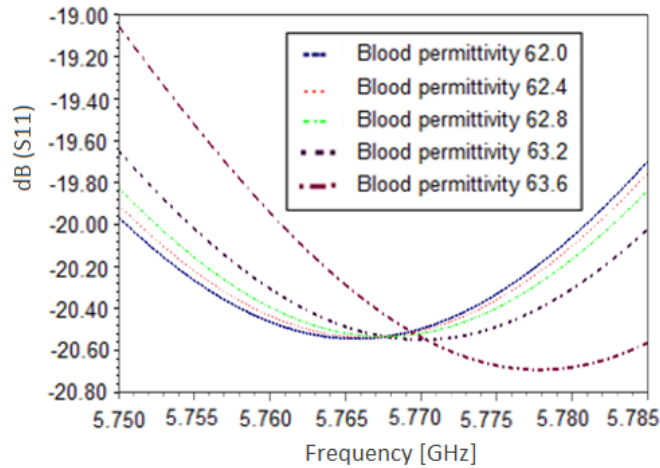


Figure 28: Simulated  $S_{11}$  of antenna in human tissue results in a shift of resonant frequency as blood permittivity varies.

Plotting frequency versus blood permittivity in Figure 29, one can observe that as blood permittivity increases, the frequency increases via an approximate second order equation as shown in the figure (i.e., polynomial fit).

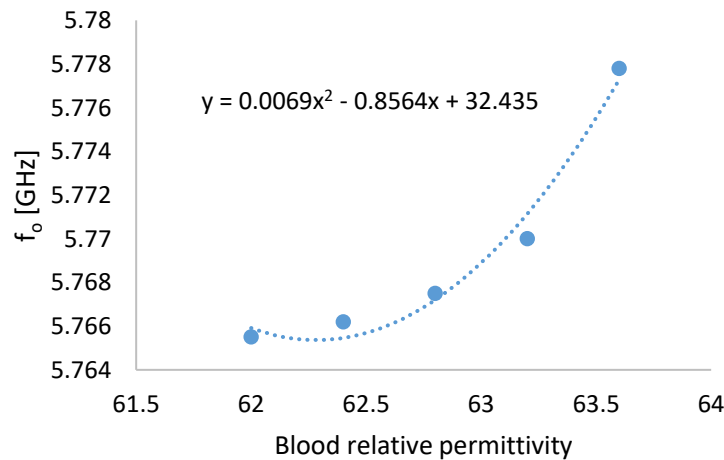


Figure 29: Plot of simulated resonant frequency vs. blood permittivity of the antenna. Note that the dependence roughly follows the polynomial fit displayed in the figure.

## 2.6.5 Summary of Active Sensing Antenna Design

The single antenna design simulated in the fatty tissue facing blood and muscle was optimized for an average blood permittivity of 62.5 by variation of the antenna's dimension and location of the feed distance  $p_y$ . The resulting antenna dimensions were:  $subX=2.4\text{cm}$ ,  $subY=1.9\text{cm}$ ,  $subH=10\text{mil}$ ,  $patchX=4.1\text{mm}$ ,  $patchy=7.1\text{mm}$ ,  $px=0\text{mm}$ ,  $py=1.4\text{mm}$ , for a distance from the antenna to the blood tissue layer of 2mm. The blood permittivity was varied from 62 to 63.6 in steps of 0.2 using a discrete sweep, resulting in a total frequency variation for this range from 5.7655 to 5.7778, respectively. In total, for this range of blood permittivity, the frequency variation was 12.3 MHz, corresponding to a 500mg/dL glucose variation. Since an increase of glucose level in blood decreases its permittivity, it can be concluded that at greater glucose levels, the resonant frequency will be lower. The antenna design can be used for an active sensing system as displayed in Figure 1. To further continue this path of research, a corresponding sensor platform to both drive the antenna and measure any glucose-dependent shift in resonant frequency is necessary. This will be discussed in Chapter 4.

## 2.7 Passive Sensing Simulations

### 2.7.1 Overview of Passive Sensing System

The passive sensing system has been simulated in the same human tissue model (Figure 12) described for the antenna active sensing system. However, in this case, the sensing antenna simulated needs to be dual sided, facing both the muscle with one side for sensing purposes and the skin and external antennas with the other side for communication purposes. As was described in Figure 2, the overall passive sensing method requires an implanted antenna in human tissue and two additional antennas located external to the body to complete the system. In the simulation, the two additional external antennas are in the air box section of the model. Figure 30 shows the antennas of the system located in the human tissue model.

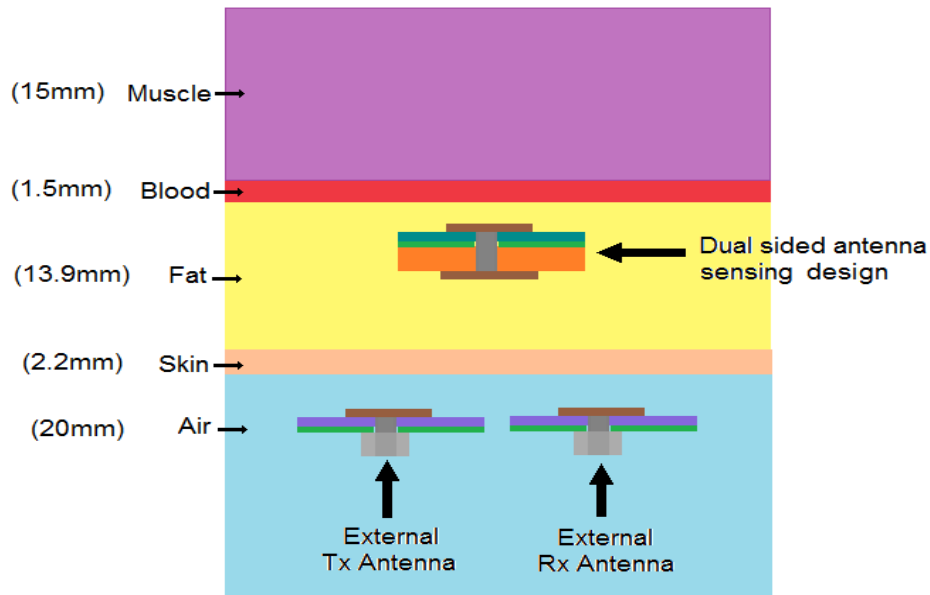


Figure 30: Passive sensing requires an implantable antenna and two external antennas. The implanted antenna is dual sided and located in the fatty tissue. The external antennas are located external to the human tissue in the air.

This analysis of the system was done by parts: The external antennas are simulated individually and  $S_{11}$  was recorded, followed by the external antennas simulated together to record the coupling between them. During this analysis the antenna separation distance was varied. To design the dual sided antenna, two parts were required: an antenna design for the side facing the blood and muscle, which coincides with the active sensing antenna function, and an antenna facing the external area, which interacts with the external antennas. This latter part is further evaluated. A summary of the passive sensing system was evaluated through simulation and is now discussed in detail.

### 2.7.2 Single External Antenna

The external antennas were simulated individually, located 2mm from the skin as displayed in Figure 31. Note that both antennas have the same dimensions, therefore yield same  $S_{11}$  result. The simulated value of  $S_{11}$  of the optimized external antenna is displayed in Figure 32.



This parameter was used as a reference level of the external antenna  $S_{11}$  to human tissue without the effect of other external or internal antennas present.

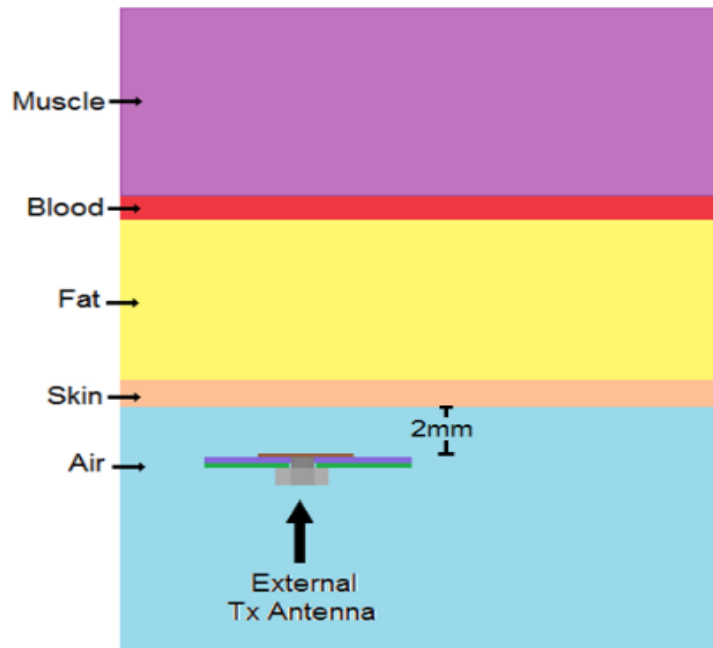


Figure 31: Simulation setup with one external antenna only in the air space. The external antenna is placed 2 mm above the skin layer, as shown.

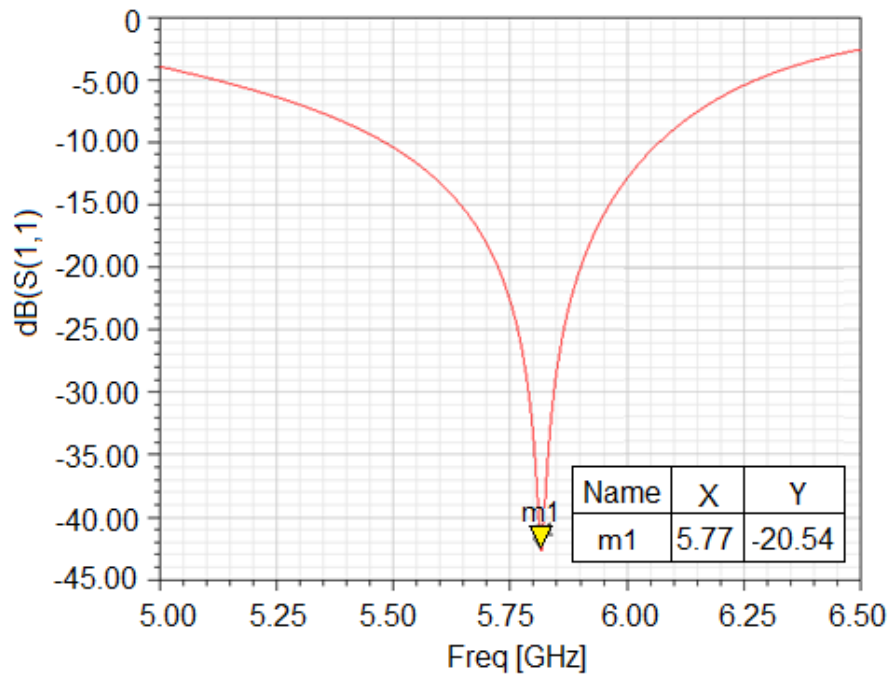


Figure 32: Simulated  $S_{11}$  for external (or internal) antenna only.

### 2.7.3 External Antennas Tx and Rx

The external antennas were simulated simultaneously to obtain the effect that the antennas have on each other, by recording their  $S_{11}$  and  $S_{21}$  parameters, and analyzing the results versus the separation distance between the antennas  $sep\_d=1mm$ ,  $10mm$  and  $20mm$ ; keeping the distance of 2mm from the skin. The solutions of  $S_{11}$  and  $S_{21}$  (return and insertion loss) for both the external and internal antennas facing the human tissue, and without the embedded antenna as set up in Figure 33, are displayed in Figure 34 and Figure 29, respectively. The  $S_{21}$  levels for this simulation was our reference point for subsequent simulations.

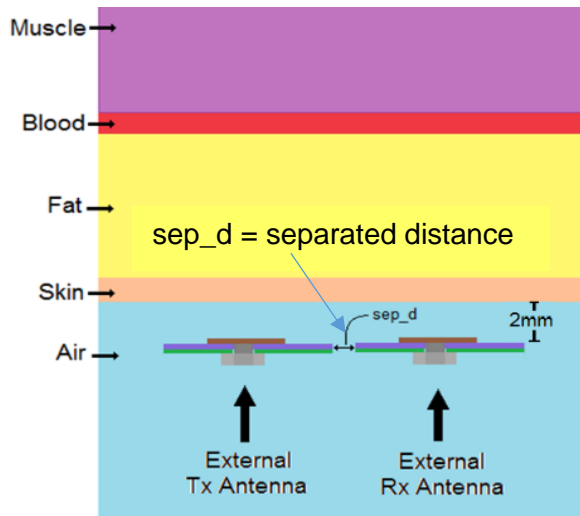


Figure 33: Simulation model for both external antennas separated by 1, 10 or 20mm.

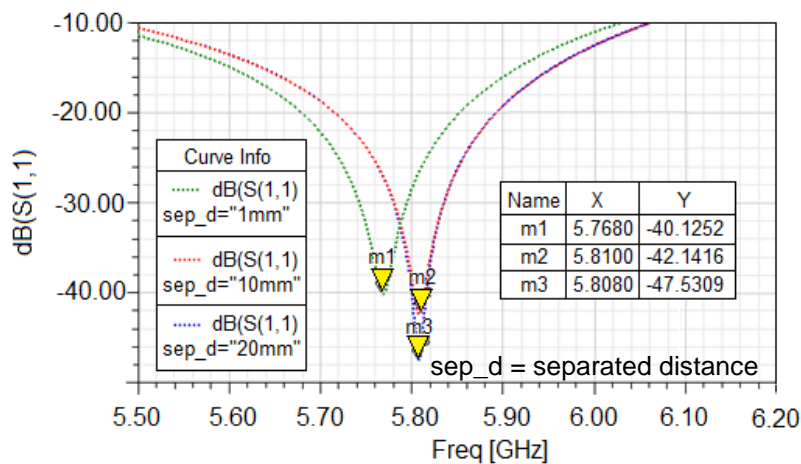


Figure 34:  $S_{11}$  for external antenna setup of Figure 33, for  $sep\_d= 1,10$  and  $20mm$ . Note the optimum return loss to the largest spacing of  $20mm$ .

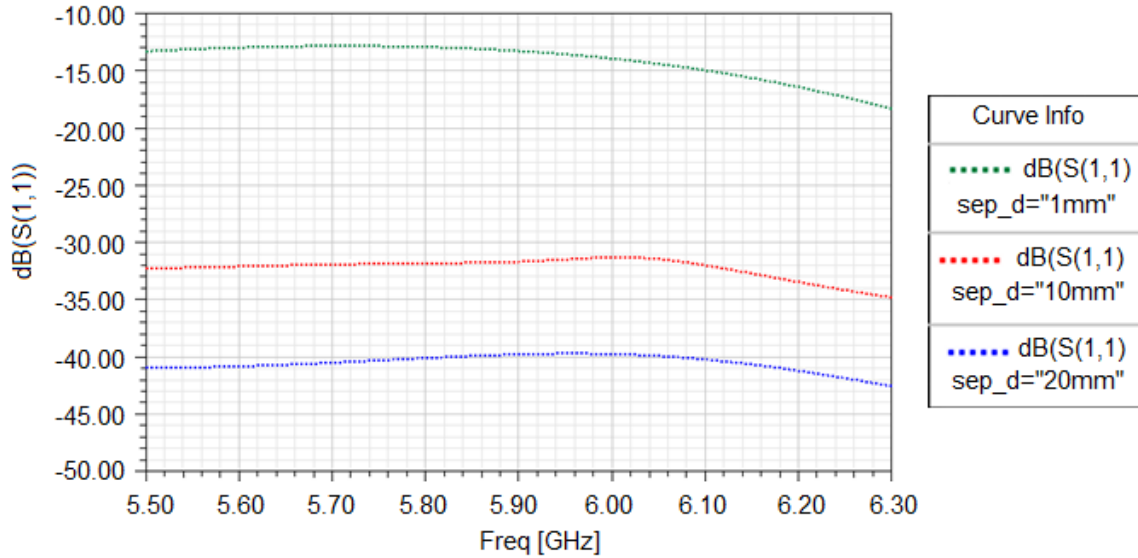


Figure 35:  $S_{21}$  for external antenna setup of Figure 33 for  $sep_d=1, 10$  and  $20$ mm. As expected the largest value of  $S_{21}$  corresponds to the largest separation between the antennas (i.e.,  $20$  mm).

## 2.7.4 Implantable Antenna

The passive system utilizes an embedded antenna that has two qualities: 1) Has blood glucose sensing potentiality, and 2) this variation must be detectable by the external antennas. This section describes the antenna as a blend of two antennas, each with the quality described. For the antenna to have the first quality, the sensing potentiality, it must have a characteristic similar to the active antenna, in which the resonant frequency of an antenna patch varies in correlation with the variation of the electrical properties of the blood (permittivity and electrical conductivity). For this to work the antenna patch of this antenna must be facing the muscle and blood. Note that this is the antenna described in the active sensing section. For the antenna to have the second quality, detectable by external antennas, the signal incoming from an external antenna must be reflected in this implanted antenna into the second external antenna. For this aspect, the antenna must be facing the external antennas. Therefore, the passive antenna must have a combination of the two requirements: an antenna facing the muscle to detect variations of the blood glucose, and an antenna facing the external antennas, to interact with external antennas, as displayed in Figure 36.

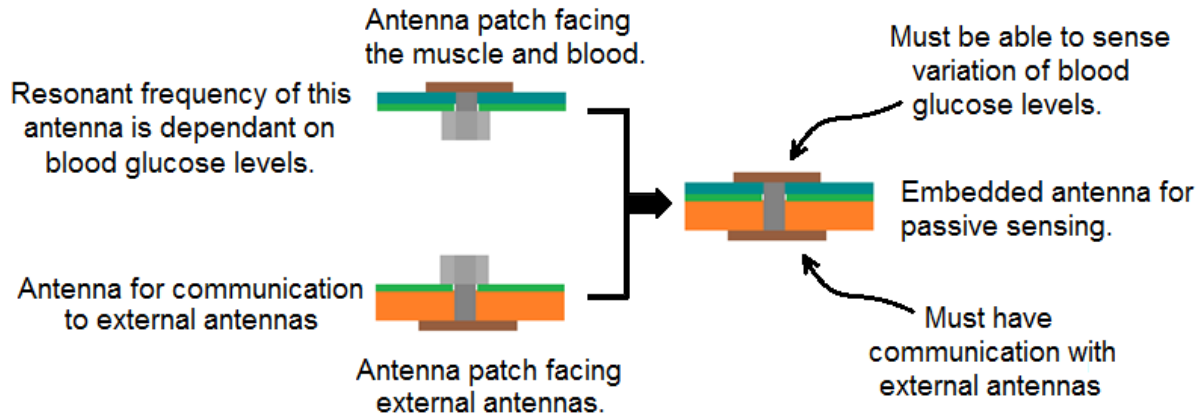


Figure 36: Implantable antenna as a two single sided antenna with two functions. The implant must both detect variations of blood glucose levels and 2) communicate with the external antennas.

### 2.7.4.1 Sensing Properties

The dual sided antenna facing the muscle and blood senses the blood glucose levels by correlation between shift of resonant frequency and the variation of the blood glucose levels, as for the active sensor discussed previously. Figure 37 displays the partial embedded antenna model that has sensing potentiality. Notice this partial passive antenna is the model used for the active antenna.

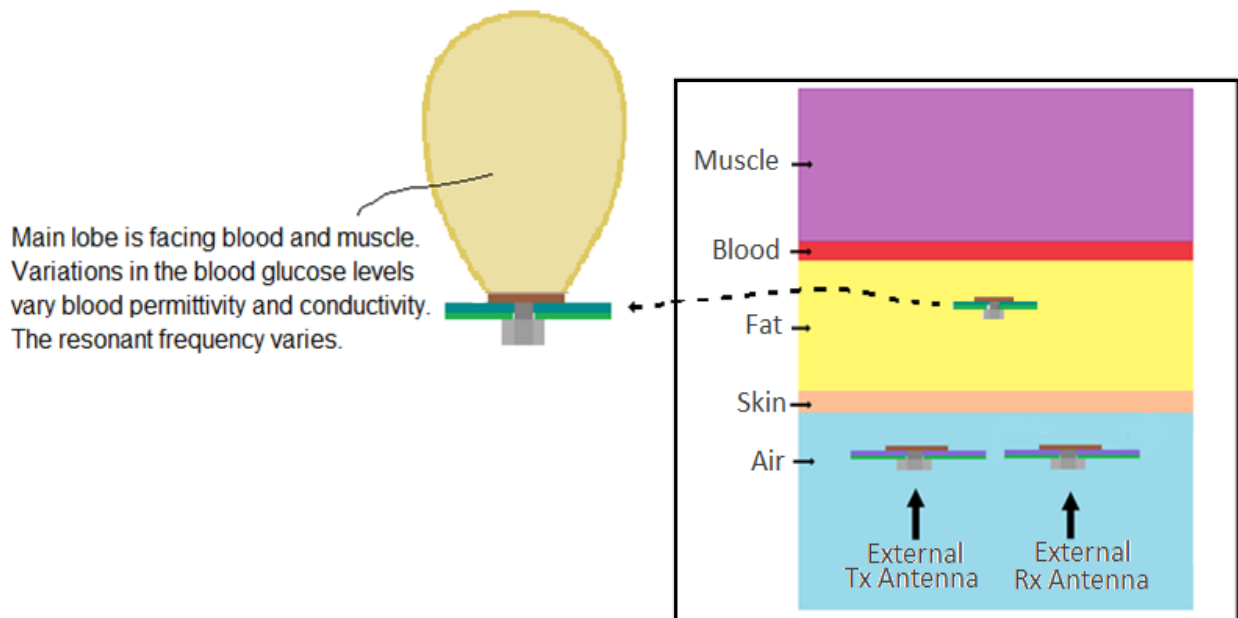


Figure 37: Partial implanted antenna must detect glucose variations. Note that this is the antenna designed in the active sensing mode.

### 2.7.4.2 Communication with External Antennas

The external Tx antenna sends a signal to the implanted antenna, which must be reflected back to the receiving antenna Rx. Therefore, the main lobe of the antenna patch must be in the direction of the external antennas, as displayed in Figure 38.

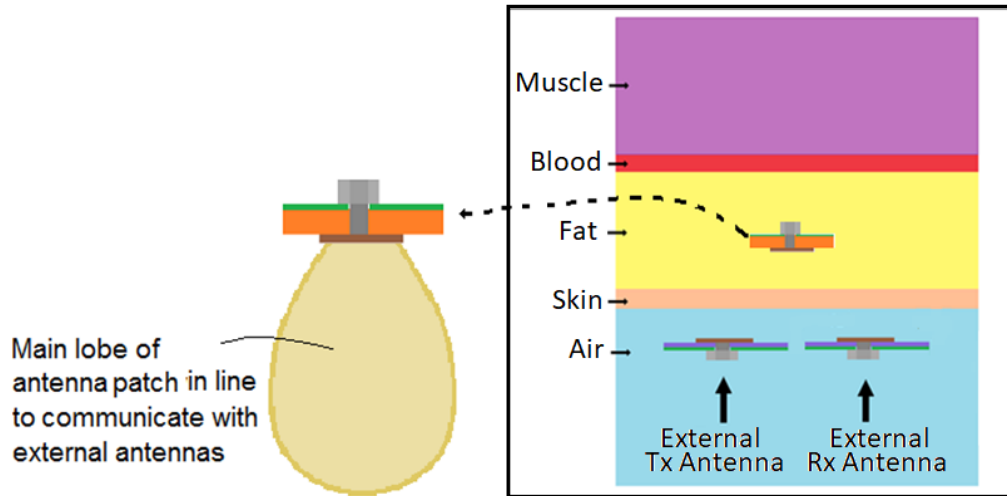


Figure 38: Partial implanted antenna must communicate with the external antennas. Tx excites the sensor patch and Rx reads the corresponding shift in resonance frequency due to glucose variations.

To analyze the antenna setup they were first tested in free space with and without the passive antenna, and the results are summarized in Figure 39.

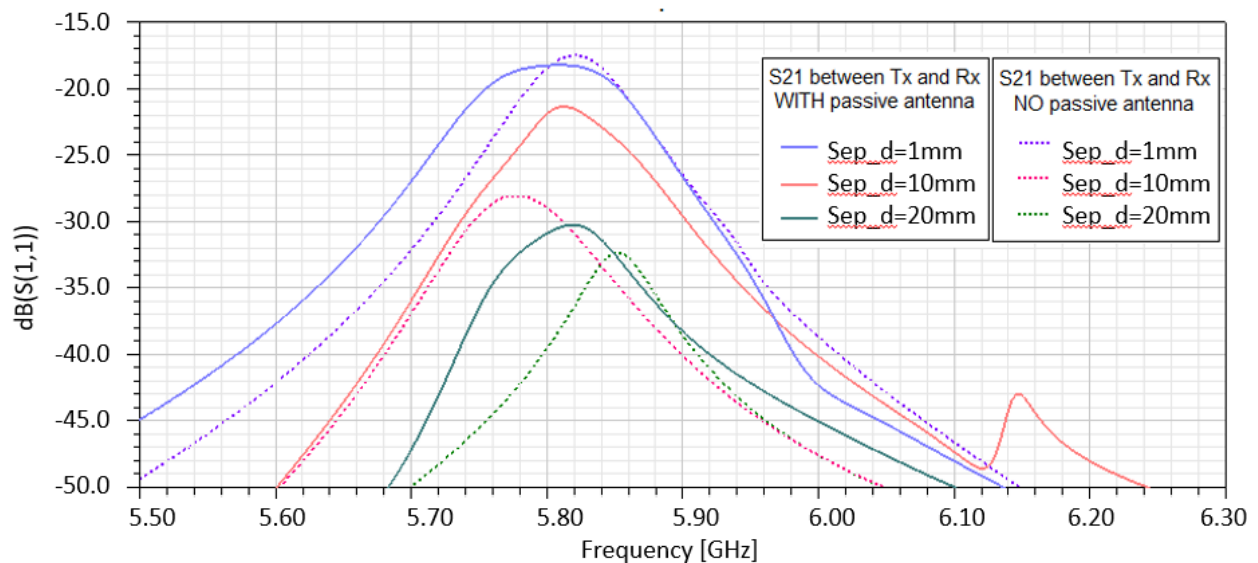


Figure 39: Simulated  $S_{21}$  results of passive sensing antenna setup in free space. Simulation with the passive antenna (solid curves) and without (dotted curves).

Analyzing the  $S_{21}$  of external antennas with and without the passive antenna implanted in human tissue, it was concluded that a separation distance of 1mm was too close. There is high mutual coupling between the external antennas for this separation distance. The  $S_{21}$  was around -18dB without the implanted antenna while the implanted antenna decreases  $S_{21}$  by ~ 1dB between the implanted antenna and no antenna. A separation distance of 20mm between the external antennas was too far from the reflecting signal. The  $S_{21}$  was around -33dB without the implanted antenna, and improves by ~ 3dB with the implanted antenna present. The separation distance between external antennas was 10mm. The  $S_{21}$  varies from ~-22dB to -28dB with the implanted antenna, with ~ a 5dB variation between the implanted antenna and no antenna.

To analyze the communication of the implanted antenna with the external antennas in human tissue, the simulation was performed by parts to obtain the effect of each individual part. The first analysis was for an embedded substrate with an integral ground plane in the fatty tissue at 2mm and at 7mm from the blood block with the external antennas separated by 1mm, 10mm and 20mm. As a reference point, the solution where two external antennas were located outside the body without any implant was used for this and all other subsequent analysis. In the next analysis, a patch was added to the embedded substrate with ground, maintaining all other parameters. Then, the feed was added while maintaining all other parameters. Finally, all parameters were maintained, removing the feed of the embedded antenna, but leaving the perforation for the feed.

#### **2.7.4.2.1 Effect of Embedded Substrate and Ground**

In the first analysis by parts, the simulation was performed with the following setup. A substrate with ground embedded in the fatty tissue layer at 2mm (Figure 40a) and 7mm (Figure 40b) from the blood block were added to the previous setup of the external antennas separated by 1mm, 10mm and 20mm (Figure 33). This was done to compare the effect of the implanted

substrate on  $S_{21}$  of the external antennas. For an average fat thickness of 13.9mm, at 2mm from the blood (Figure 40a), the substrate was located 11.9mm from the skin. At 7mm from the blood (Figure 40b), the substrate was located at 6.9mm.

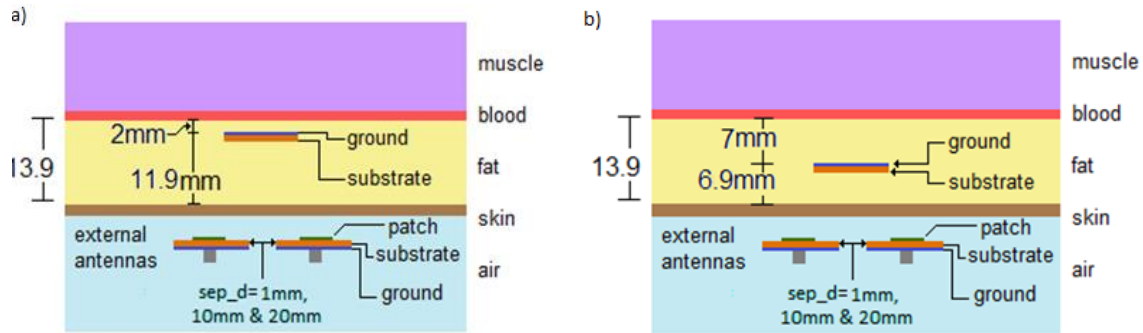


Figure 40: External antennas and embedded in fat substrate with ground plane model. Implant at a) 2mm and b) 7mm from blood.

The  $S_{21}$  of the external antennas were compared when there was no implant (dotted lines), and when there was an implant with a ground plane 2mm from the blood layer (dashed lines) in three cases: external antennas separated by 1mm (green), by 10mm (red) and by 20mm (blue). For frequencies lower than approximately 5.9GHz, the  $S_{21}$  of the external antennas when there was an implant was higher than the cases where there was no implant in the body by 1dB to 4dB, depending on the separation distance of the external antenna (Figure 41).

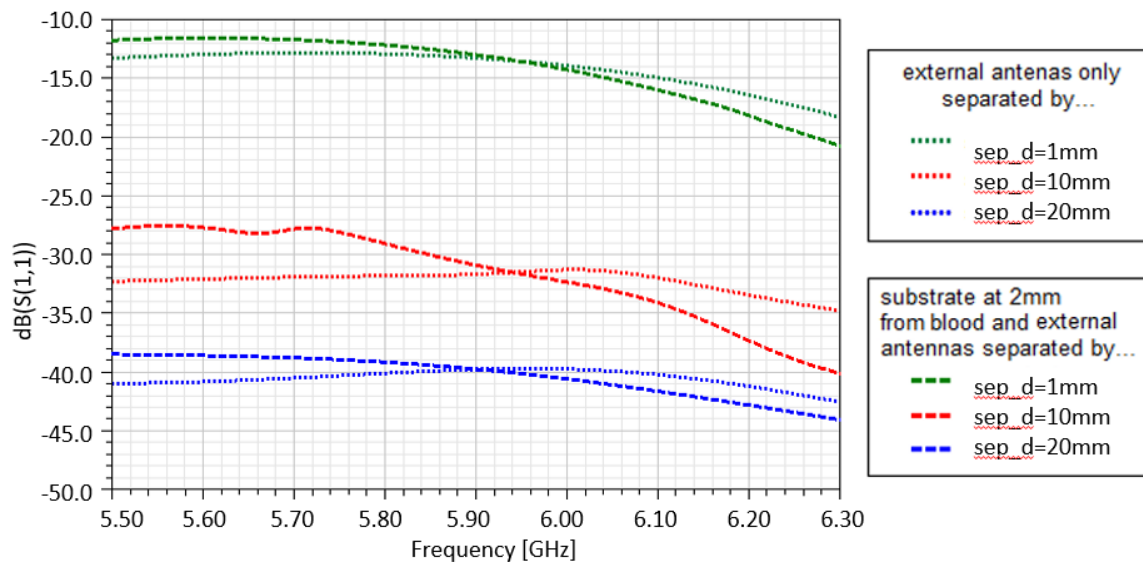


Figure 41: Simulated  $S_{21}$  of external antennas with internal substrate with a ground plane at 2mm from blood / muscle layer.

In Figure 42, the  $S_{21}$  of the external antennas is compared when there was no implant (dotted lines), and when there was an implant with a ground plane placed 7mm from the blood layer (short dashed lines) for the same three cases as before: external antennas separated by 1mm (green), by 10mm (red) and by 20mm (blue). For the case of the antennas being separated by 1mm, and for frequencies less than approximately 5.8GHz, the  $S_{21}$  of the external antennas when there was an implant is higher than the cases where there was no implant in the body by around 2dB. For the case of the antennas being separated by 10mm, the  $S_{21}$  of external antennas the when there is an implant is higher than the cases where there is no implant in the body by 8dB to 10dB for frequencies between 5.5GHz and 5.9GHz. For the case of the antennas being separated by 20mm, the  $S_{21}$  of the external antennas the when there was an implant was higher than the cases where there was no implant in the body by 8dB to 12dB for frequencies between 5.5GHz and 5.9GHz.

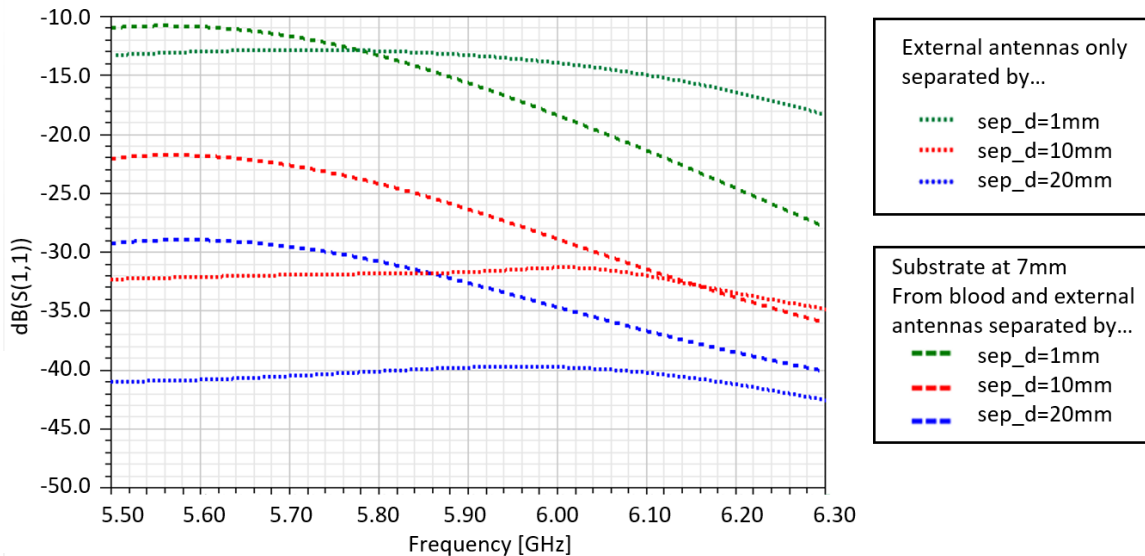


Figure 42: Simulated  $S_{21}$  of external antennas with internal substrate with a ground plane at 7mm from blood / muscle layer.

All three cases have been graphed separately: When the external antennas have been separated by 1mm (Figure 43), by 10mm (Figure 44 ) and by 20mm (Figure 45), where  $S_{21}$  with no implant (dotted line) is compared to  $S_{21}$  with implant at 2mm from blood (dashed) and with  $S_{21}$



with implant at 7mm from blood (short dashed). When the antennas are separated by 1mm, at 5.8GHz all  $S_{21}$  results have less than 1dB difference for the case there is no implant, approximate to -12dB, for when the implant at 2mm from the blood and for when the implant is at 7mm. When the antennas are separated by 10mm, at 5.8GHz all  $S_{21}$  varies from -23dB (at 7mm) to -28dB (at 2mm), to -32dB (when there is no implant).

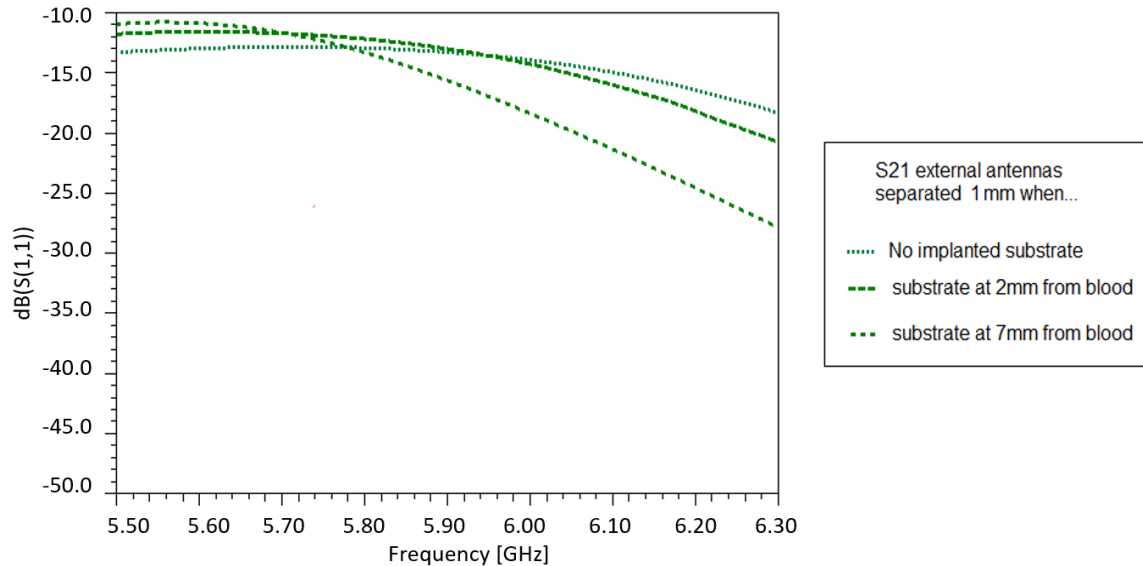


Figure 43: Simulated effect of implanted substrate on  $S_{21}$  of external antennas separated by 1mm.

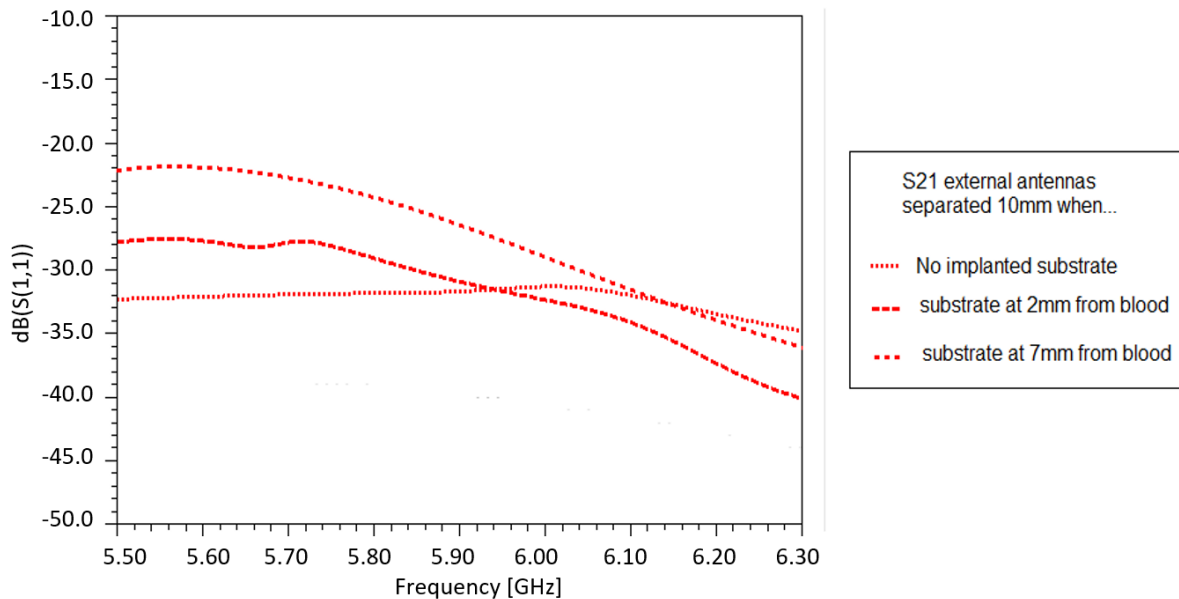


Figure 44: Simulated effect on implanted substrate on  $S_{21}$  of external antennas separated by 10mm.

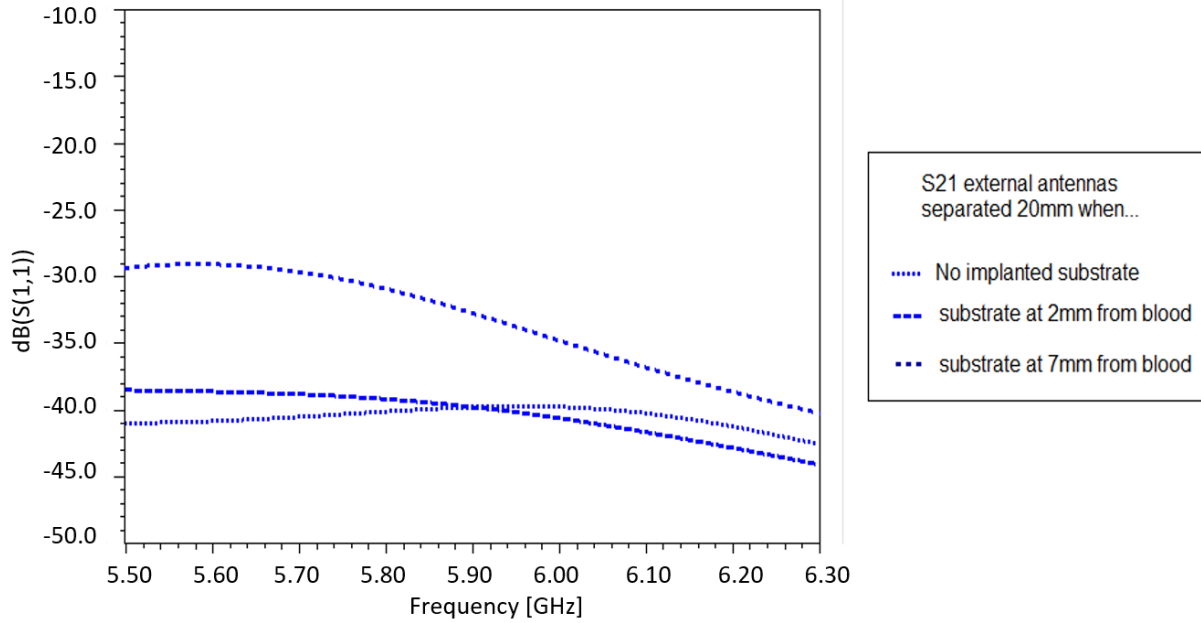


Figure 45: Simulated effect of implanted substrate on  $S_{21}$  of external antennas separated by 20mm.

Figure 46 shows a summary of the external antenna  $S_{21}$  dB for three cases: no implant, implant in the fatty tissue 2mm from the blood (at 11.9mm from the skin) and implant 7mm from the blood (at 6.9mm from the skin). Here we can observe that when the antennas are separated by 1mm, an implant has little effect on the results. Having the antennas separated by 20 mm,  $S_{21}$  is too low to be useful for this application. .

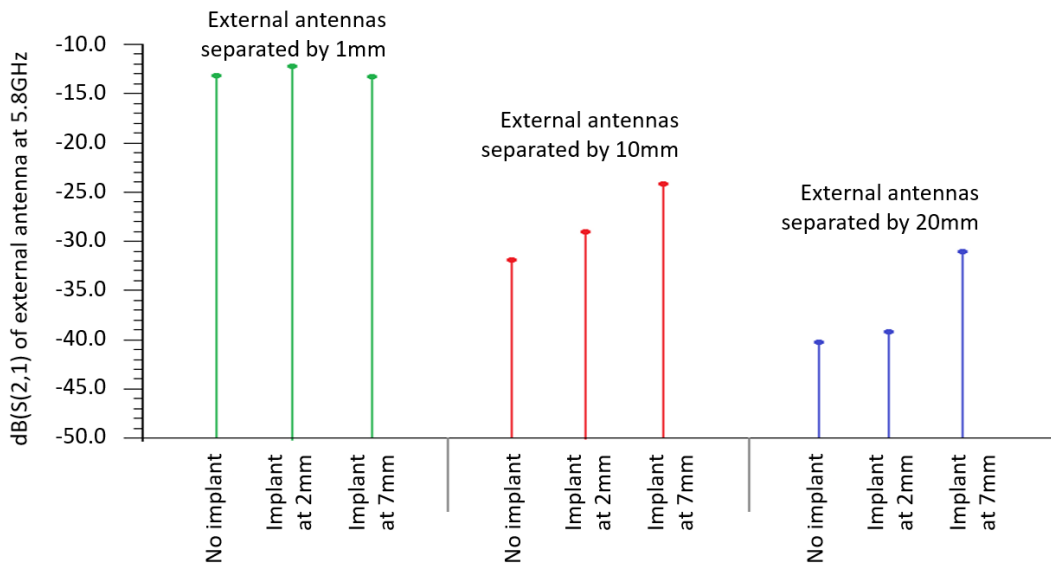


Figure 46: Comparison of the simulated  $S_{21}$  [dB] of the external antennas at 5.8GHz as a function of their separation and in relation to the internal implant position.

### 2.7.4.2.2 Effect of Embedded Patch, Substrate and Ground

In the next analysis by parts, as shown in Figure 40, a patch antenna was added to the implanted substrate of the previous section (Figure 40).

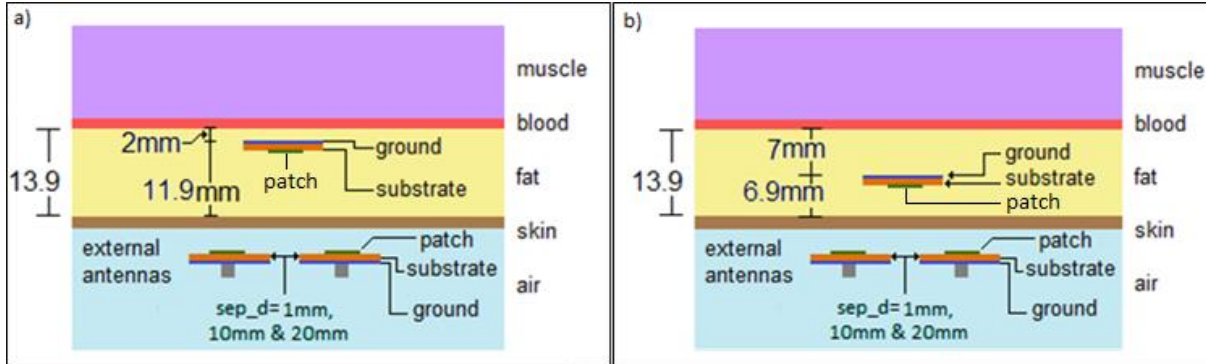


Figure 47: Configuration with implant in fat layer 2mm and 7 mm from the blood layer. Implant composed of substrate, ground plane and patch antenna.

Figure 48 and Figure 49 show the effect of the patch on substrate implant on the external antenna performance. The difference between the case in which the substrate and ground is implanted and the case in which the patch, substrate and ground is implanted is less than 1dB when this implant is located 2mm from the blood (Figure 48) and not noticeable when the implant is located 7mm from the blood (Figure 49).

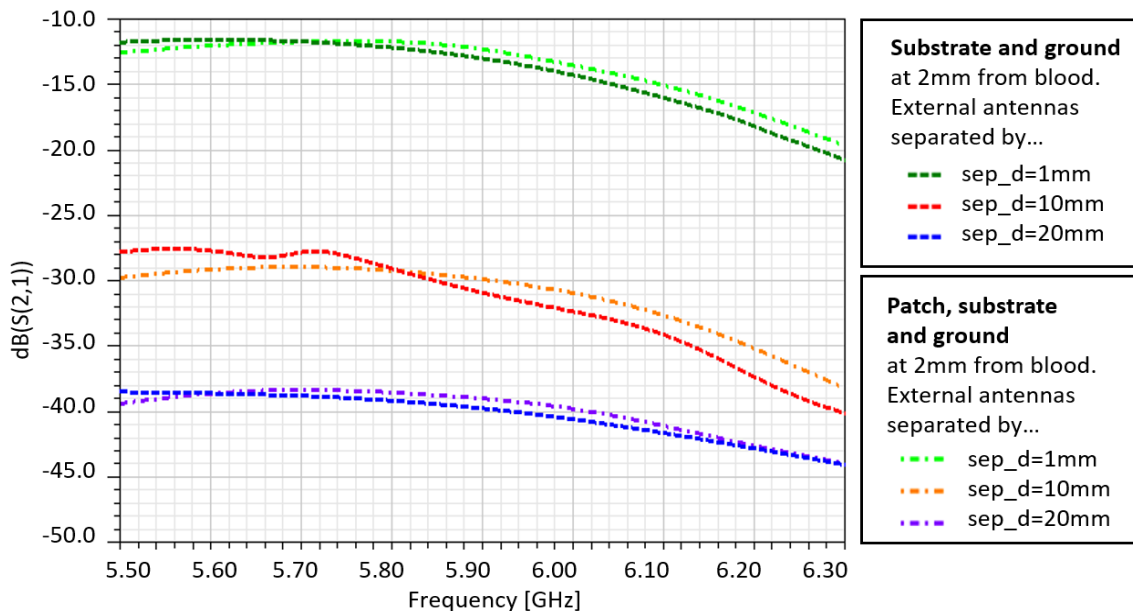


Figure 48: Effect on the  $S_{21}$  of external antennas of adding patch on implanted substrate and ground at 2mm from blood layer.

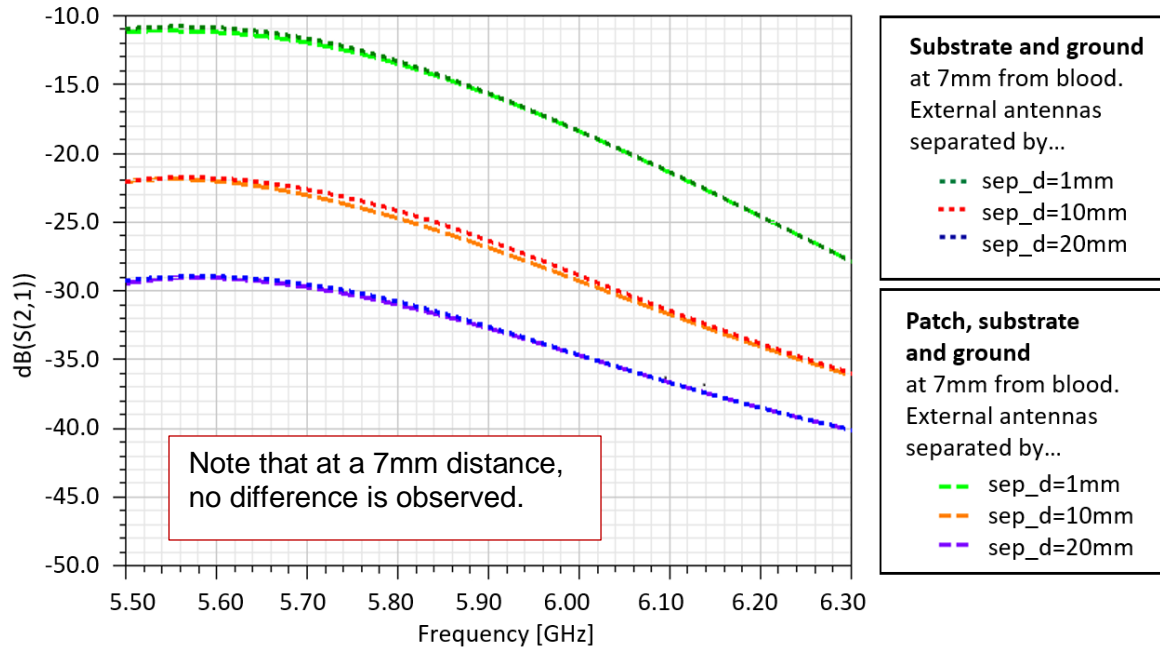


Figure 49: Effect on the  $S_{21}$  of external antennas of adding patch on implanted substrate and ground at 7mm from blood.

### 2.7.5 Passive System Simulations with Varying Blood Glucose Levels

Earlier it was noted that the implant was essentially two antennas on a single substrate: a sense antenna, identical in function to the active sensor discussed earlier, and a second antenna, on the opposite side of the implant, to interact with the external antennas. This embedded dual sided antenna was modeled in HFSS with a 10 mil top and a 50 mil bottom substrate. As previously described the top patch, located on the 10-mil substrate, is facing the blood and muscle. This dual sided antenna embedded in fatty tissue with the two external antennas configuration is shown in Figure 50 (side view) and an angular view in Figure 51.

The implant is located at 2mm from the blood to have the sensitivity required to experience a shift a resonant frequency depending on the blood glucose level, according to previous results. The external antennas are separated by 1mm. With this final setup, the simulation was performed for a blood permittivity of 62.5 and repeated with a blood permittivity of 63.6 as shown in Figure 52. With no passive antenna, the simulated  $S_{21}$  is approximately -13dB but, unfortunately, varies within a negligible range when the blood permittivity varies from 62.5 to 63.6. Using a passive

antenna,  $S_{21}$  varies from approximately -11.85 for a glucose level of 63.6dB to approximately -12dB for a glucose level of 62.5dB at a frequency 5.8GHz and no significant shift of resonant frequency is observed.

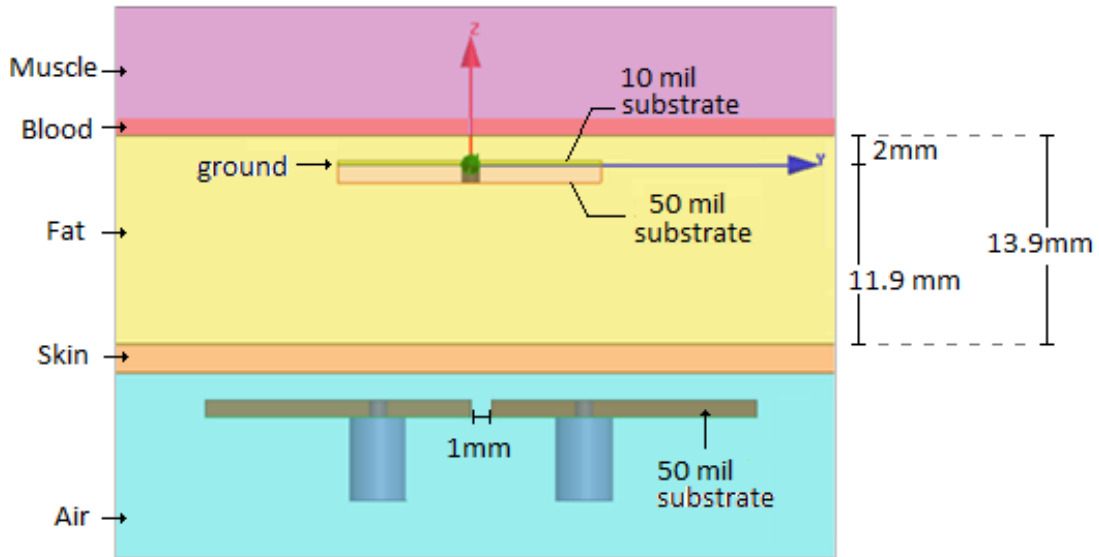


Figure 50: Passive dual antenna system as modeled in HFSS - side view.

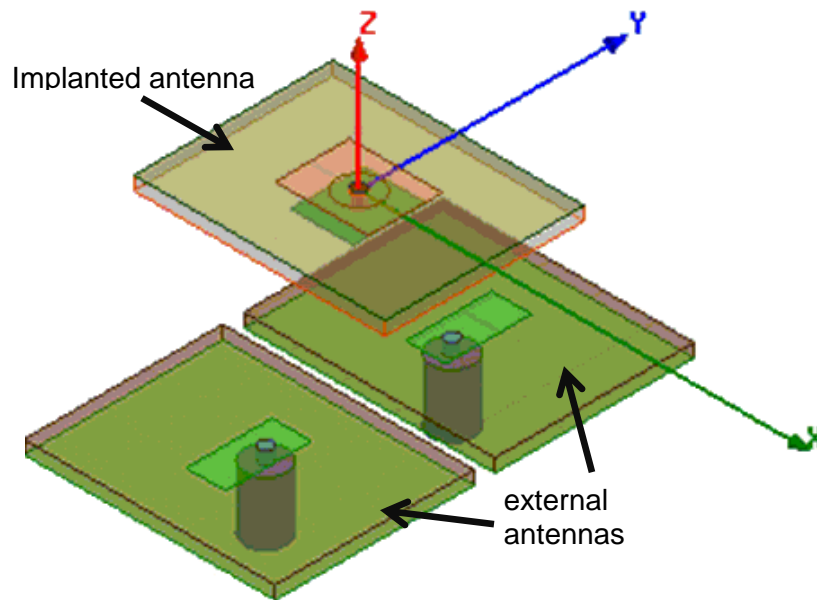


Figure 51: Three antennas passive system as modeled in HFSS - angular view. Bottom antennas in air layer which dual-sided implant is located in the fatty layer as shown in side view previously.

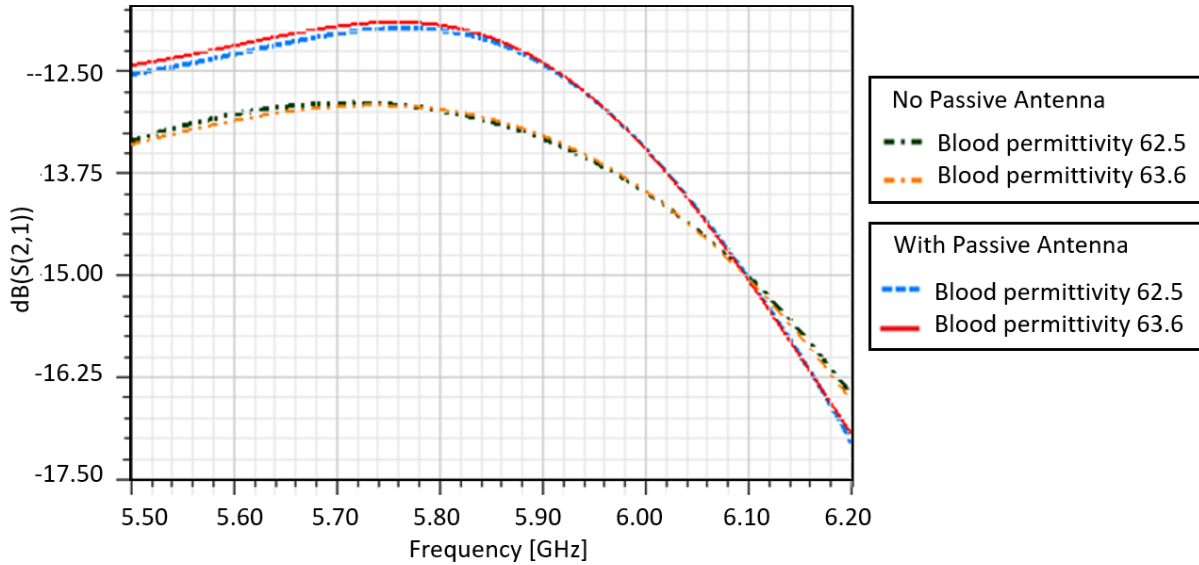


Figure 52: Passive antenna effect on  $S_{21}$  of external antennas vs. blood permittivity. Simulated with blood  $\epsilon_r = 62.5$  and  $\epsilon_r = 63.6$ . Fat simulated as free space as in preliminary test. Note negligible change in  $S_{21}$  vs. permittivity indicating that this sensing approach is not worth further consideration.

While the concept of a two-sided implant was initially thought to be a viable option for this application, the simulation results presented here do not motivate further exploration of this technique. This was somewhat surprising as results for an active implanted antenna were quite compelling. Clearly a hybrid 'active implanted, external sense' antenna system does not appear feasible for this application and was abandoned at this stage of the research.

## 2.7.6 Summary of Passive Sensing Design

Simulations for passive sensing were performed in parts in order to understand the individual contribution of the dual-antenna implant. First, the external Tx (or Rx) antenna was independently simulated in the air facing the human tissue model and, later, both antennas were simulated versus a separation of 1mm, 10mm and 20mm to predict  $S_{21}$  when no implant was in the body. This result served as a reference for the next simulations when various aspects of the dual-antenna implant was added to the simulation. Afterwards a substrate implant with a ground plane was implanted in the fatty tissue at 2mm from the blood (or 11.9mm from the skin) and at

7mm from the blood (or 6.9mm from the skin). When the antennas were separated by 1mm, the implant affects the  $S_{21}$  by less than 1dB at around the -12dB level. Having the antennas separated by 20 mm, although the implant at 7mm from the blood layer affects the signal by about 10dB,  $S_{21}$  was around -40dB. In conclusion, although there was less effect by having the antennas separated by 1mm, this separation distance allows a stronger interaction with the implant, so this was the separation distance used for the rest of the simulations. To finalize the simulations, a completely passive approach was simulated, with a dual-sided antenna implanted in the fat and the external antennas separated by 1mm. Varying the blood permittivity from 62.6 to 63.6 causes a shift of  $S_{21}$  of less than 1MHz, which is basically negligible for this application. Further simulations and would need to be carried out to have conclusive results on the passive sensing option for glucose sensing but, based on these observations, this approach was abandoned at this stage of the research in favor of the non-sensing approach which is described next.

## **2.8 Non-invasive Sensing Simulations**

### **2.8.1 Overview of Non-invasive Sensing**

For the non-invasive blood glucose sensing system, simulations were performed using the human arm tissue model described earlier in Figure 14. The antenna was designed by initially taking the single external antenna designed to function in free space, optimized to face the human tissue model, by optimizing the antenna geometry via parameters  $p_y$ ,  $patchX$  and  $patchY$ . The distance from the skin from 0mm (antenna touching the human skin) to 3mm above the skin, in intervals of 0.5mm, was studied and the antenna optimized for each spacing studied. It was observed that the optimum spacing was 2 mm. Therefore all further tests were carried out 2mm above the skin, and aligned with the blood vessel using the average human tissue skin and fat thicknesses, as well as blood vessel depth. The antenna's dimensions of the substrate and patch and the separation distance of the feed used are listed in Table 7.

Table 7: Antenna dimensions for non-invasive blood glucose sensing.

Parameter	subX	subY	patch X	patchY	subH	px	py
Dimension	2.4 cm	1.9 cm	3.7 mm	7.9 mm	25 mil	0.0 mm	1.5

### 2.8.2 Effect of Variation of Blood Vessel Electrical Permittivity

Using the external antenna optimized to the tissue model described in the last section, simulations of the antenna response as a function of blood glucose level were conducted. The blood vessel permittivity in the model was varied from 51.397 to 52.642 and the resulting return loss,  $S_{11}$ , was as shown in Figure 53. Note that the resonant frequency shifts with blood permittivity (i.e., glucose) which indicates that this sensor modality is worthy of further exploration.

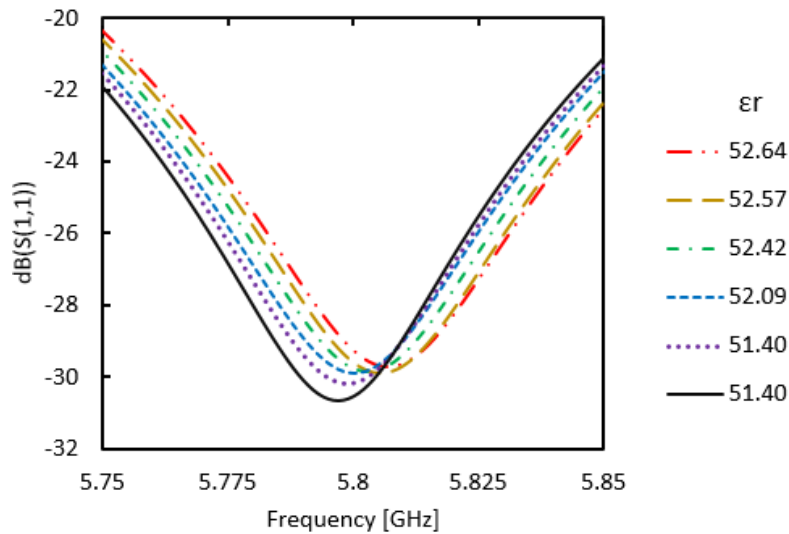


Figure 53: Variation of blood permittivity vs. return loss for non-invasive antenna. Note the predicted shift in resonant frequency,  $f_0$ , as a function of blood permittivity (i.e., glucose) thus motivating further study of this sensing approach.

In this permittivity range, a shift in the resonant frequency of 10MHz was observed. An increase of blood permittivity resulted in an increase of resonant frequency, as expected [23, 28]. Variation of the resonant frequency of the antenna was a promising result for further analysis as it appears that this sensing mode should work. Thus additional simulations to determine the resonant frequency under different conditions were conducted. Note that the graph of the return



loss was given for different relative permittivity values of the blood vessel. The next chapter details the correspondence between the relative permittivity of the blood itself.

## 2.9 Chapter Conclusion

In this chapter, the relevant literature was reviewed and the operational concepts behind RF antenna glucose sensing was presented. The chapter describes the differences between three possible sensing approaches: implantable active, implantable passive, and non-invasive sensing. The glucose-dependent properties of blood, and relevant previous works and experimental findings are presented, along with appropriate human physiological characteristics relevant for each type of sensing mode. Sensor performance was predicted using electromagnetic simulation tools to determine the anticipated resonance frequency of the antenna in free space and for each type of sensing scenario using the presented human tissue models. The optimization method of the antenna was explained and presented. Simulations for active sensing were repeated over a range of relative permittivity values and the resonant frequency found to be consistent with previous literature values. An analysis, including simulations, for the passive sensing approach, were presented in parts. Unfortunately no conclusive results as to the feasibility of this method were observed and this approach was abandoned. Finally, operational simulations for non-invasive sensing were presented using the developed tissue model. These results were so promising, an observed shift in resonance frequency as a function of blood glucose, that further analysis is more than justified and will form the basis of the rest of this dissertation.

## CHAPTER 3: NON-INVASIVE ANTENNA BLOOD GLUCOSE SENSOR

### 3.1 Chapter Overview

In the previous chapter, antennas for passive, active and non-invasive glucose sensing were designed and simulated in HFSS within a human tissue model setup that considered the permittivity, conductivity and thickness of skin, fat, blood and muscle. Of the three methods studied, the last method – non-invasive glucose sensing – proved to be worthy of additional study. The present chapter presents the results of experiments conducted to validate the promising simulated results for the non-invasive approach. These experiments were conducted using a semi-solid gel phantom that mimics the human tissue layers of skin, fat, blood, and muscle, RF sensing was implemented, as discussed previously, using an RF antenna patch designed to function in the ISM band at 5.8GHz. Simulated and experimental results are compared and discussed. Variations such as skin thickness, blood vessel depth and misalignment of the sensor with the blood vessel are presented and discussed.

### 3.2 Non-Invasive Antenna Experimental Measurements

#### 3.2.1 Introduction to Human Tissue Phantoms

Conducting tests on a human tissue phantom instead of direct testing on human subjects facilitates testing in a controlled environment as it eliminates variables such as movement, respiration, temperature variation, among other variables. A variety of phantom recipes have been proposed in the literature. Each recipe depends mainly on the testing application, while also considering factors such as location of human tissue and sensor frequency. For instance, a phantom to test the power absorption in biological tissue [51] which focuses on characteristics of

the phantom for the given purpose, will be vastly different from that of a phantom for micro-imaging of breast tissue [52], for the detection of traumatic brain injury [53], or to test the propagation of radio frequency in the body. In the case of this research, the phantom constructed needs to mimic the dielectric properties of the human skin, fat, blood and muscle in the upper arm area.

### **3.2.2 Human Tissue Phantoms Mimicking Electrical Properties**

A recipe for a phantom that mimics the electrical properties has been reported [31]. The preparation is made from de-ionized water, gelatin, NaCl, oil, and dishwasher detergent. The gelatin serves as a collagen gelling agent to solidify the mixture. The dishwasher serves as a surfactant agent. The de-ionized water is heated to the boiling point and then mixed with gelatin until the mixture is completely dissolved. The mixture is left to cool to 35°C, at which point the NaCl and dishwasher detergent are slowly added to the mixture. When the temperature reaches 28°C, the oil is slowly added to the mixture. The prepared solutions during the tests are left to solidify for a period of 5 hours and measurements are taken within a period of 12 hours as no preservatives are used in this recipe.

However, the recipe is given for a broadband application for a different frequency of 0.3 to 20GHz. The difference between the desired electrical properties at 5.8GHz for each layer and those presented in [31] are too large to be used in the desired tests. Therefore, a modified recipe was needed to mimic the permittivity and conductivity presented in [33, 38] for the skin, fat, blood and muscle in the frequency range of interest (5.8GHz, ISM Band) and by the blood glucose electrical property models presented in [27, 39]. The modification to the desired permittivity and conductivity values was achieved by altering the oil and salt proportions of different mixtures. By increasing the oil concentration, the relative permittivity is decreased while also affecting electrical permittivity. By increasing the salt proportion, the electrical conductivity is increased while also affecting the relative permittivity.

The dielectric properties were measured using ENA Network Analyzer model E5063A and HP dielectric probe model 85070 using the coaxial probe method described in [54] as displayed on Figure 54.

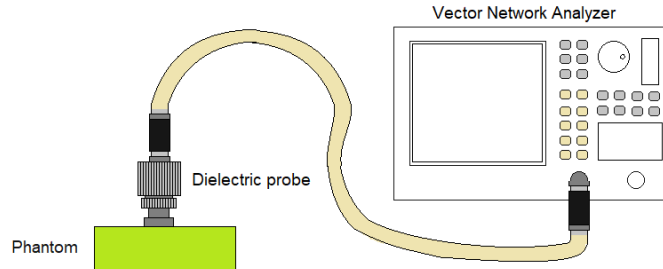


Figure 54: Coaxial probe method for measuring the permittivity of solids and semi-solids using an HP dielectric probe model 85070 [55].

The human tissue phantom is composed of skin, fat, muscle and blood. The skin, blood and muscle, for a frequency of 5.8GHz, are approximated as shown in Table 8. Note that in this initial recipe, the blood has no added glucose. The fat phantom was made from pork tissue. Measurements were taken from the sides and the center for each of the tissue samples, which were distinguished by different food coloring (Figure 55).

Table 8: Human tissue phantom ingredients for upper arm for skin, fat and muscle

Human Tissue	De-ionized water	Gelatin	NaCl	Oil	Detergent
Skin	105g	12g	0.35g	31g	20g
*Blood (NG)	525g	60g	2.5g	40mg	100g
Muscle	315g	36g	0.751g	41g	60g

\*Blood (NG) will refer to Blood (No glucose) during the rest of this dissertation.

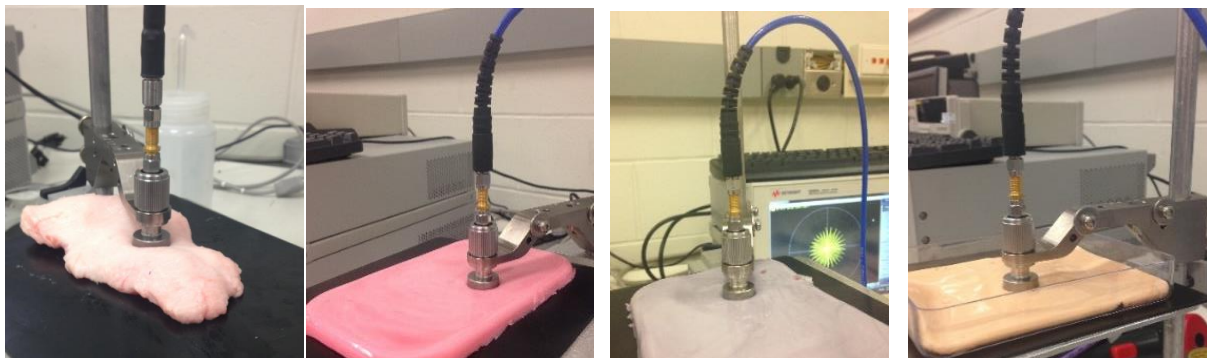


Figure 55: HP Dielectric probe model 85070 measurement on each human tissue layer. In order from left to right: a) fat phantom, b) blood phantom, c) muscle phantom and d) skin phantom.

The values obtained closely approximated the permittivity and conductivity values of the skin, blood and muscle within the frequency range of 5.725 - 5.875 GHz. The measured versus calculated relative permittivity and conductivity values are shown in Figure 56. The relative permittivity and conductivity of the fat phantom is shown in Figure 57. Although the relative permittivity and conductivity of the fat phantom were not matched to the optimal calculated fat tissue electrical properties. However the variations were negligible, since the fat permittivity, which measured approximately  $\epsilon_r=6.5$  as opposed to the optimal calculated value  $\epsilon_r=5$ , was much lower than the blood, skin and muscle values that range around  $\epsilon_r=50$ . Therefore, the measured vs. calculated blood, skin, and muscle tissue yielded a similar proportional value to the fat tissue.

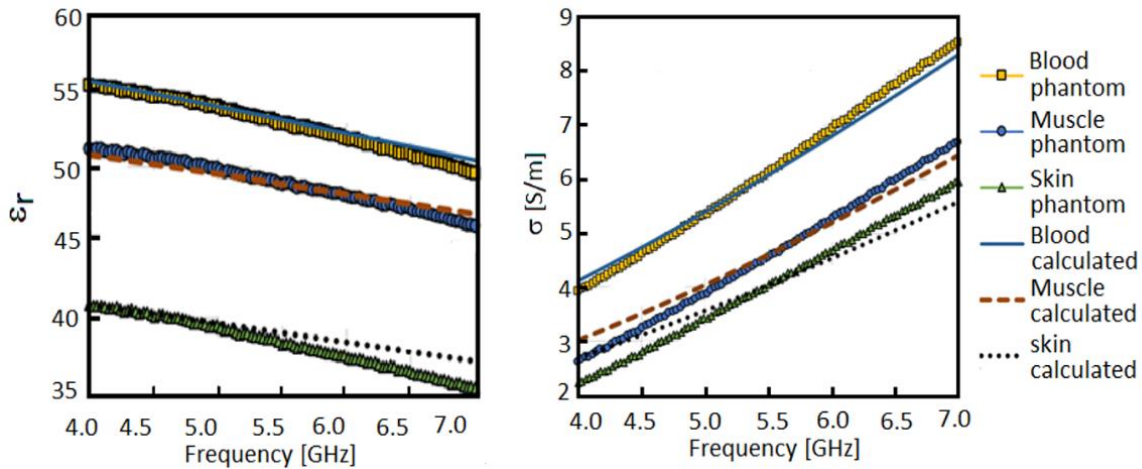


Figure 56: Dielectric properties of human tissue phantoms for skin, muscle and blood. Measured vs. calculated in the range of 4 to 7 GHz of  $\epsilon_r$  (left) and  $\sigma$  (right).

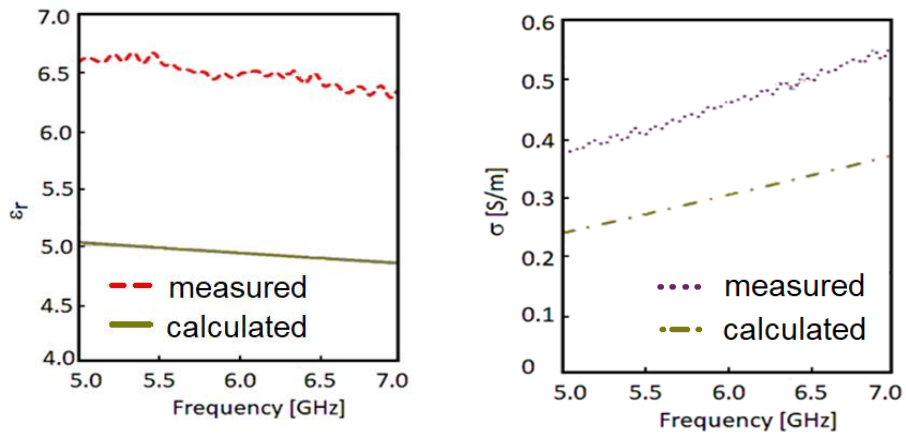


Figure 57: Dielectric properties of the fat tissue phantom. Measured vs. calculated values in the range of 5 to 7 GHz of  $\epsilon_r$  (left) and  $\sigma$  (right).

Additional phantom blood mixtures were prepared with the recipe previously described in Table 9. For each 100g of de-ionized water in the mixture, 0.1 g, 0.3g, 0.5g, 1g, 2g, 4g of Sigma D(+) glucose with a molecular mole concentration of 180.16g/mol was added for each phantom, respectively. The dielectric properties of the glucose-containing blood phantoms were measured using the HP dielectric probe 85070 shown in Figure 58. The relative permittivity measured was graphed and compared with the calculated values [37] in Figure 59.

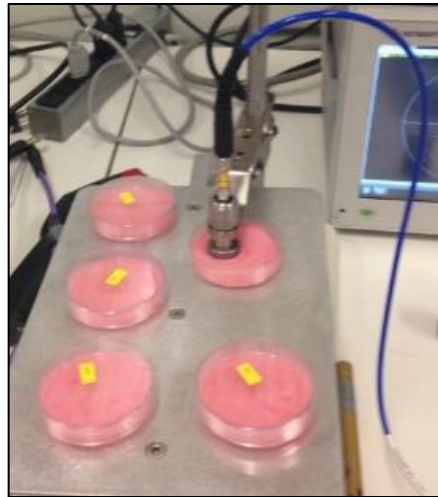


Figure 58: Photograph of HP dielectric probe model 85070 used to measure the dielectric properties of the on blood glucose samples.

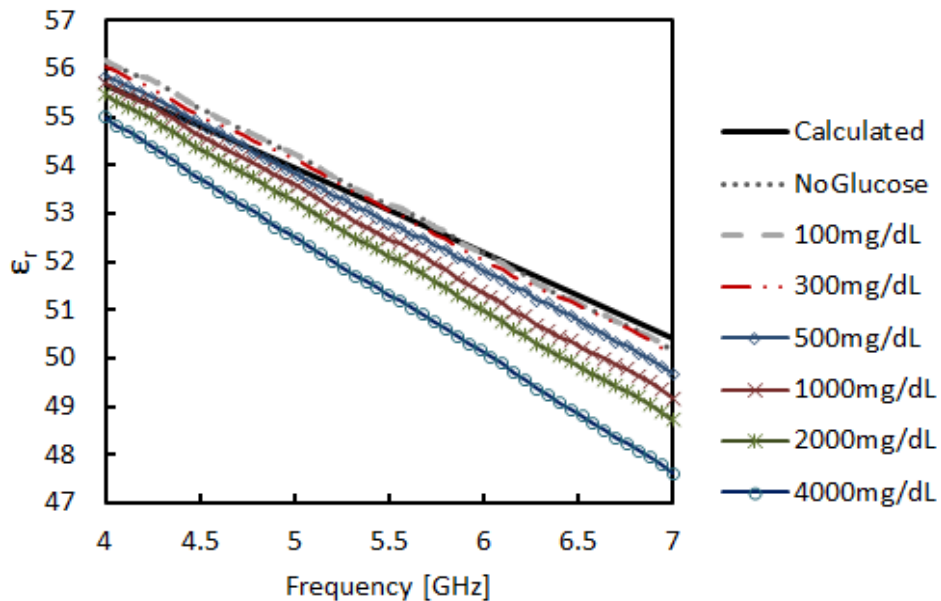


Figure 59: Permittivity,  $\epsilon_r$ , of blood phantom samples with added D-glucose. Measured results and calculated (black line) at frequencies between 4 to 7 GHz.

The measured blood glucose permittivity for 5.74, 5.8 and 5.86GHz are plotted versus glucose concentration and the data fitted with a polynomial trend. For 5.8GHz, the fitted polynomial equation of the measured blood phantom relative permittivity versus glucose is:

$$\epsilon_r (g_{5.8}) = 0.0596 g_{5.8}^2 - 0.7416 g_{5.8} + 52.642 \quad (5)$$

where  $\epsilon_r$  is the measured relative permittivity of the blood phantom at 5.8GHz and ( $g_{5.8}$ ) is the glucose concentration of the blood phantom in g/dL. Table 9 summarizes the blood phantom glucose concentration vs. both measured and calculated relative permittivity.

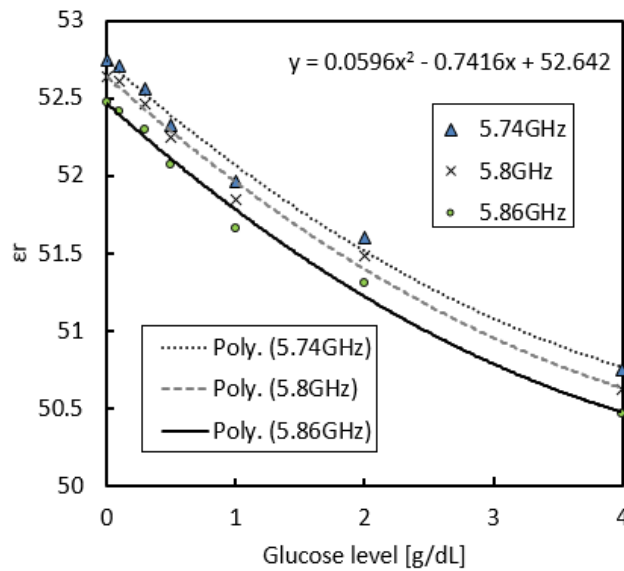


Figure 60: Measured relative permittivity at 5.8GHz vs. glucose level. Polynomial approximation fitted from 0 to 4000mg/dL (see equation (9)).

Table 9: D-Glucose concentrations in blood phantom and  $\epsilon_r$

D-glucose		D-glucose in blood phantom*		Calculated $\epsilon_r^{**}$	Measured $\epsilon_r$
[g]	[mmol/l]	[mmol/l]	[mg/dl]		
0	0	0	0	52.642	52.635
0.1	0.55506	5.550622	100	52.568	52.611
0.3	1.66518	16.65186	300	52.425	52.466
0.5	2.77531	27.75311	500	52.286	52.250
1	5.55062	55.50621	1000	51.960	51.847
2	11.1012	111.01243	2000	51.397	51.482
4	22.2024	222.0248	4000	50.629	50.616

\* For every 100ml of de-ionized water

\*\* Calculated using Equation 1

### 3.2.3 Experimental Measurements

#### 3.2.3.1 Experimental Setup

The tissue phantom was assembled as follows. First the muscle layer was set as the bottom (base) layer. Next the fat layer, containing a 2-mm wide groove to be replaced by a blood phantom vessel layer, was added. Additional fat strips were then added to the top and bottom of the blood vessel strip phantom, so that the phantom was leveled. Lastly the skin phantom was added on top to complete the arm tissue phantom. The antenna was then placed over the skin phantom in line with the blood vessel phantom. The antenna was fixed in a position with a mechanical device to ensure the antenna's position was 2mm above the skin phantom. Figure 61 shows the steps used in assembling each human tissue phantom while Figure 62 is a photograph of the antenna within the holder being placed on human tissue phantom. To have firmer phantoms for the assembly process, the phantoms were cooled to 5°C for one hour and left at room temperature for another hour. This caused a slight bending on the sides of each phantom. The corner regions were noted to not have the relative permittivity of interest, so the antenna is placed at the center of the phantom where the values were as expected.

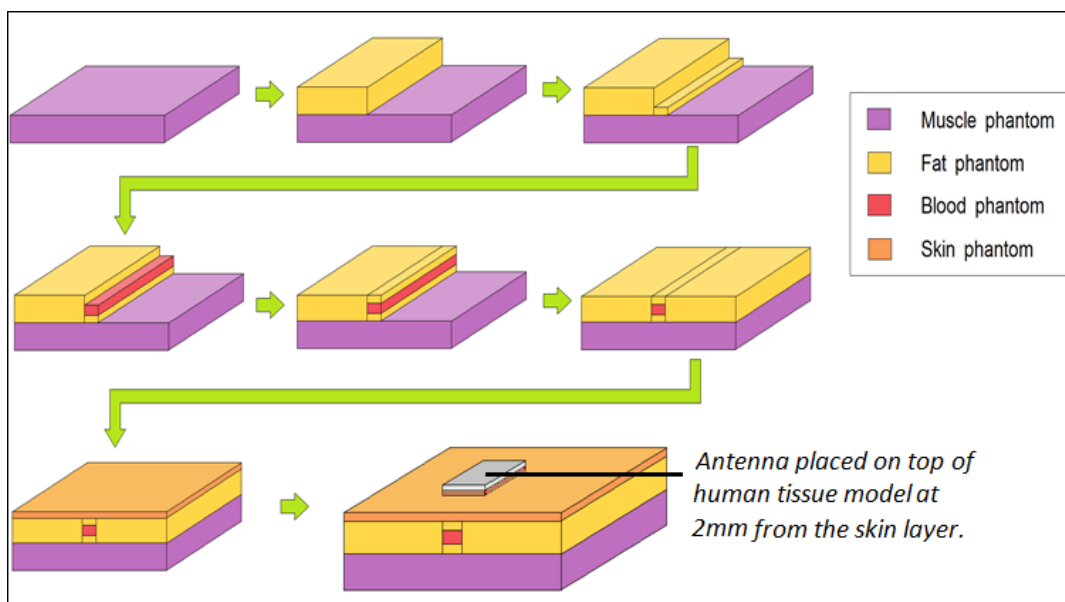


Figure 61: Steps for layering the human tissue with the blood vessel phantom. The blood vessel phantom is buried in the fat layer to mimic the Cephalic vein of the upper arm.



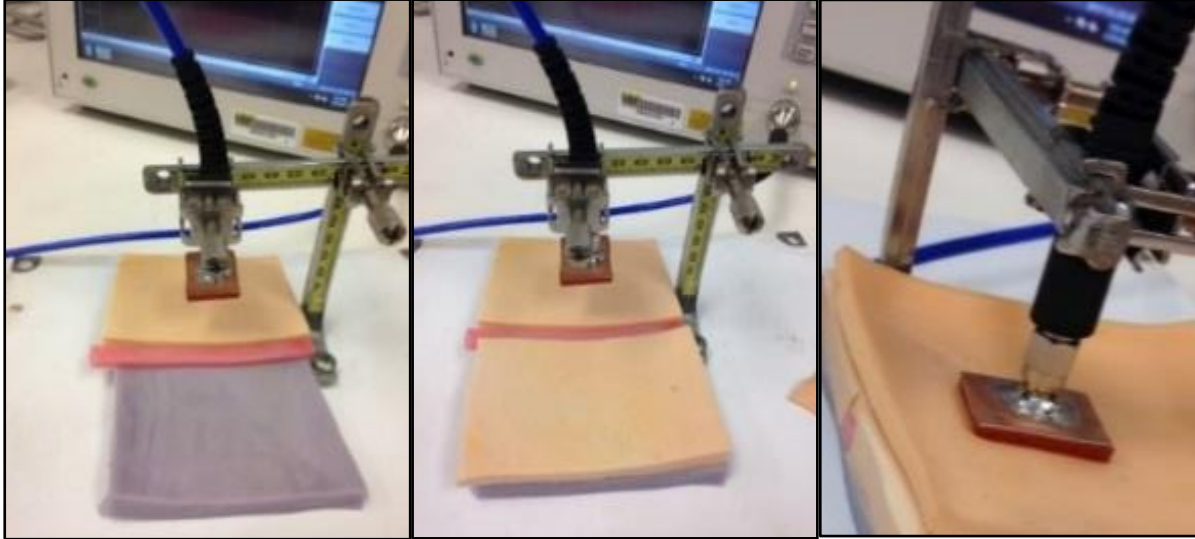


Figure 62: Photographic sequence showing the assembly of the human tissue phantom. The 5.8GHz sense antenna is shown and mounted inside a 2 mm standoff to maintain the optimum 2 mm spacing above the phantom.

### 3.2.3.2 Measured and Simulated Results

Measurements of the antenna patch were taken placing the antenna at 2 mm above the human phantom and in direct line of sight of the blood vessel with the setup previously described for blood glucose level 0, 100, 500, 1000 and 2000mg/dL. These were simulated over the 0 - 2000mg/dL glucose range using the equivalent relative permittivity calculated using Equation (5). Figure 63 (top figure) plots both the simulated and measured return loss  $S_{11}$ [dB] from 5.5 GHz to 6.1 GHz. The possible reasons for the variations observed between the simulated and measured experiments is discussed in a later section. What can be highlighted from the results presented here is that, through both methods, a shift of resonant frequency was detected due to variations of relative permittivity in the blood vessel, which corresponds to a variation of glucose levels. For glucose levels variations of 2000mg/dL, this shift of resonant frequency was found to be 13 MHz from the measured data and 11MHz from the simulated data. To visualize this, a close-up graph for the measured and simulated return loss are plotted in Figure 63 (bottom figures). The measured close-up is plotted in the frequency range 5.75 to 5.95 GHz and the simulated close-up is plotted in the frequency range 5.75 to 5.85GHz.

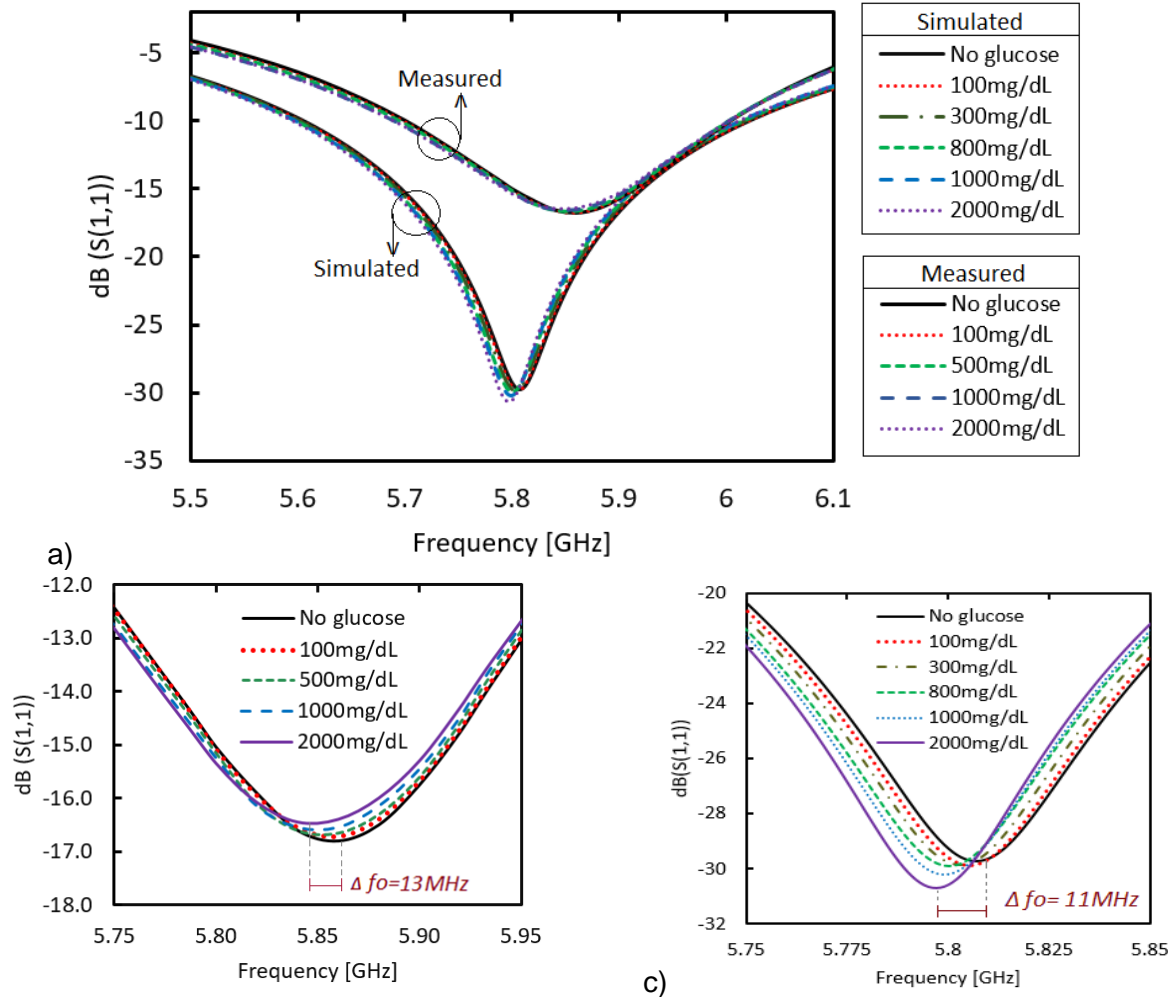


Figure 63: Return loss of the antenna as a function of glucose concentration. a) Measured and simulated plotted over range of 5.5 to 6.1GHz (top figure). b) Close-up of measured. Note total variation of 13 MHz for glucose variation of 2000mg/dL. c) Close-up of simulated return loss. Note total variation of 11 MHz for glucose variation of 2000mg/dL.

Figure 64 summarizes the measured and experimental results when the non-invasive antenna was placed 2mm above the skin and centered over the blood vessel. It can be observed that a glucose variation from 0 to 2000mg/dL resulted in a similar change in resonant frequency, although there is a shift in the data as mentioned earlier. This shift can be due to variations of thickness of the tissues layers used in the experimental setups, the slight variations of the permittivity and conductivity thickness, as well as small variations during the fabrication process of the antenna. Despite this shift, the resonant frequency variation based on glucose level concentration has a similar trend.

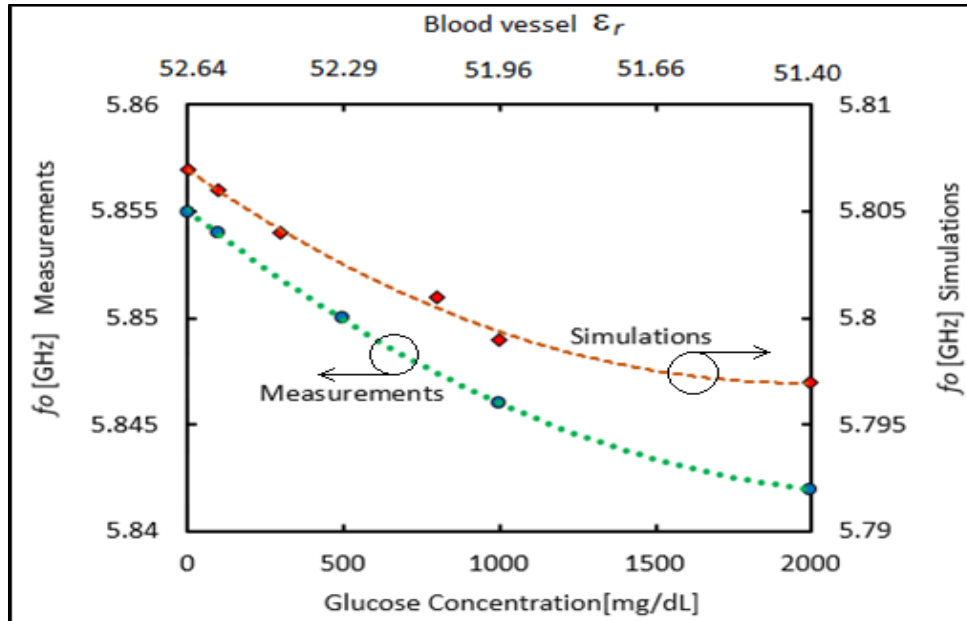


Figure 64: Measured and simulated  $f_o$  vs. glucose concentration [mg/dL] and blood  $\epsilon_r$ . Note similar tendency values with an offset between experimental and simulated data.

Based on this data it seems feasible to use a single RF sensing antenna to extract glucose information from blood in nearly real-time. What is needed now is the development of a sensor platform that can perform these measurements in real-time with an automated output of the assessed glucose value provided that setting the sense antenna properly can be achieved. Chapter 4 presents the development of the sensor platform. First factors that lead to variations of return loss must be properly understood, which are addressed in the next section.

### 3.3 Factors that Affect the Non-Invasive Antenna's Return Loss

#### 3.3.1 Physiological Factors

##### 3.3.1.1 Skin Thickness and Resonant Frequency

Analysis of the effect of the skin thickness was simulated with and without the blood vessel present. The skin thickness was varied from 1.5mm to 3.5mm, and the results plotted in Figure 65. Two distinct behaviors for simulations with blood vessel and without the blood vessel can be observed. For locations where there is no blood vessel under direct line of sight of the antenna,

for ranges lower than 2.2mm of skin thickness, decreasing the thickness of the skin decreases the resonant frequency and for ranges above 2.2mm, increasing the thickness of the skin decreases the resonant frequency. For areas where a blood vessel is in direct line of sight with the antenna, this point of variation changes to around 3mm of skin thickness. For skin thickness below 3mm, an increase of skin thickness results in an increase of resonant frequency, and for skin thickness above 3mm, an increase of skin thickness results in a decrease of resonant frequency. In a realistic average human tissue skin (2.44 - 2.48mm), a thicker skin would affect the result in return loss by increasing the resonant frequency when above the a blood vessel, while decreasing the resonant frequency if no blood vessel is in direct line of sight of the antenna. This behavior is used during the calibration stage of the programming of the system, described in chapter 4. Once calibrated, the variation of skin thickness person by person would not affected the result, as the skin thickness remains unchanged for the same person over the testing period. Regular calibration of the sensing system would keep the system prediction at the correct linear change of glucose levels until the next recommended calibration.

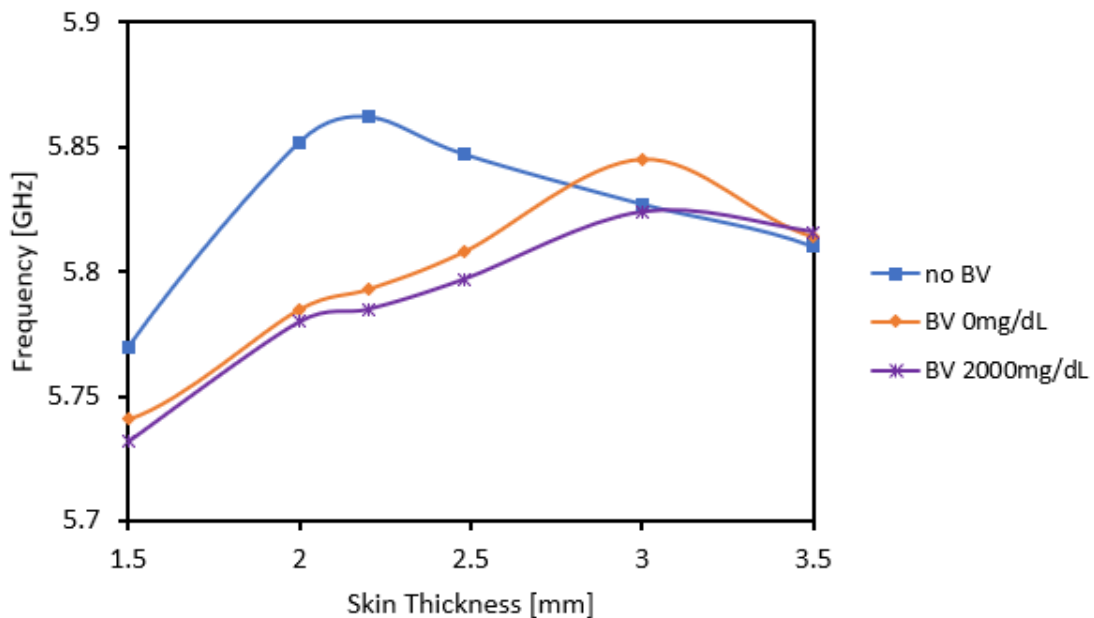


Figure 65: Skin thickness variation effect on resonant frequency. Simulated with human tissue model without blood glucose present.

### 3.3.1.2 Deepness of the Blood Vessel

A second factor that varies from one individual to another is the depth of the blood vessel. The targeted vessels are the ones located near the surface of the skin, but to test extreme values, a depth variation of 2 to 3mm was assumed. To distinguish the effect due to blood vessel and its depth, the model was evaluated with a glucose level of 300mg/dL. The results of this simulation are shown in Figure 66 where it can be observed that a change in depth by 1 mm produces a shift of resonant frequency of  $\approx 50$ MHz. Once again, this can be nulled out during the system calibration as each patient's vessel position is likely to be static.

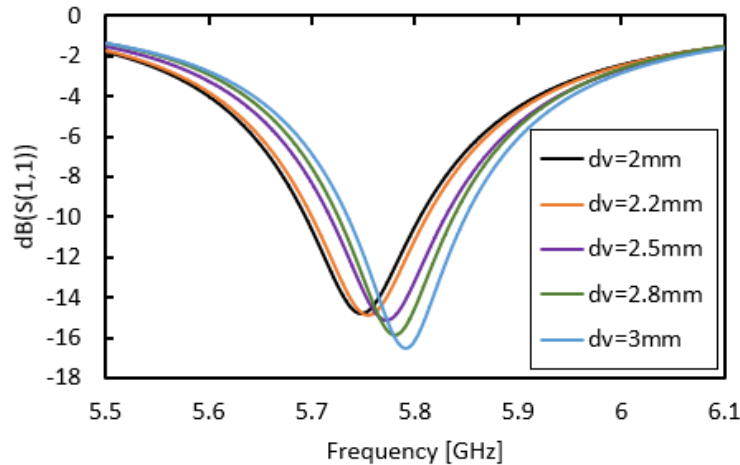


Figure 66: Effect of blood vessel depth variation on resonant frequency. A  $\approx 50$  MHz shift was observed for a depth change of 1 mm.

### 3.3.2 Misalignment of Antenna

#### 3.3.2.1 Vertical Displacement

With the antenna centered over the blood vessel, the antenna's vertical position above the skin was varied from 0.5 to 3.5 mm in 0.5mm intervals. No significant variation of shift of resonant frequency is presented when putting the antenna at different vertical elevated positions from the skin. However, the amplitude peak at the resonance frequency experiences is different at each position, where the deepest peak is found to be at 2mm above the skin. Although the interest variation is frequency shift, it is of significant importance to maintain the vertical position

stable as the technique used in the sensing system that will be described in chapter 4 involves sampling the signal at different frequencies to detect the variations of reflected power level. For this, the deepest peak is the one desirable, which is the 2mm distance from the skin. During the experimental tests, as described in a previous section, the antenna is built on a holder that ensures a 2mm distance from the skin. To implement this device in a realistic scenario, the 2mm spacing can be controlled with a 2mm standoff placed between the skin and antenna.

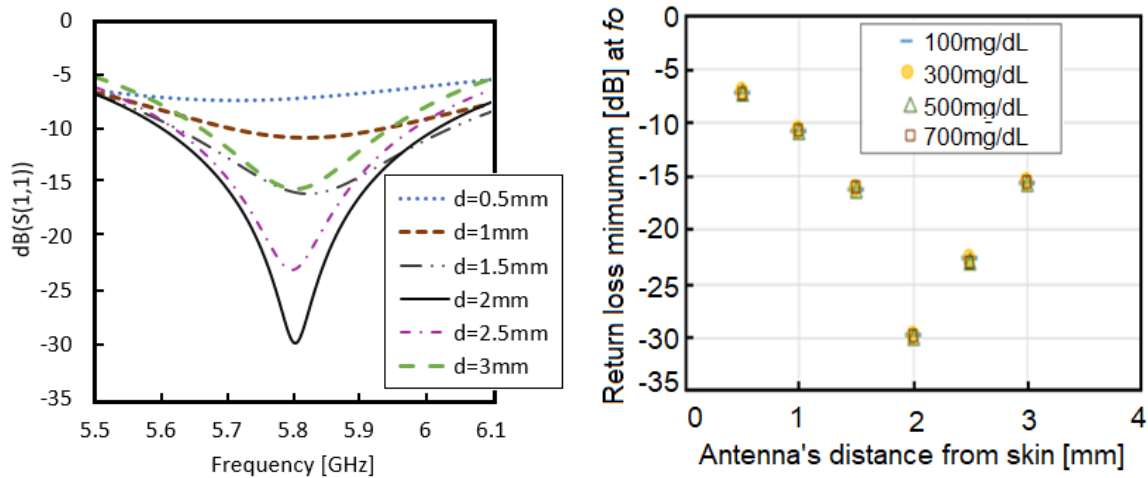


Figure 67: Vertical variation effect on the return loss of the non-invasive antenna. Return loss for blood vessel containing 700mg/dL of glucose (left). Return loss minimum amplitude at resonant frequency vs. antenna distance from skin for different blood glucose levels of 100, 300, 500 and 700mg/dL. Note optimum performance observed for 2mm height above the skin.

### 3.3.2.2 Lateral Displacement

Until this point in the exploration of using a single sense antenna to non-invasively estimate blood glucose level the antenna was aligned with the center of the blood vessel. The effect of lateral displacement was determined by placing the antenna 2mm above the skin, using a skin thickness of 2.48mm, and then displacing the antenna laterally from the blood vessel. Figure 68 summarizes the effect on the observed resonant frequency due to lateral displacement of the antenna. Notice that as the antenna is displaced further from the blood vessel, the resonant frequency approaches the resonant frequency simulated with the human tissue model without a

blood vessel which certainly makes sense as the antenna beam profile would not subtend the vessel.

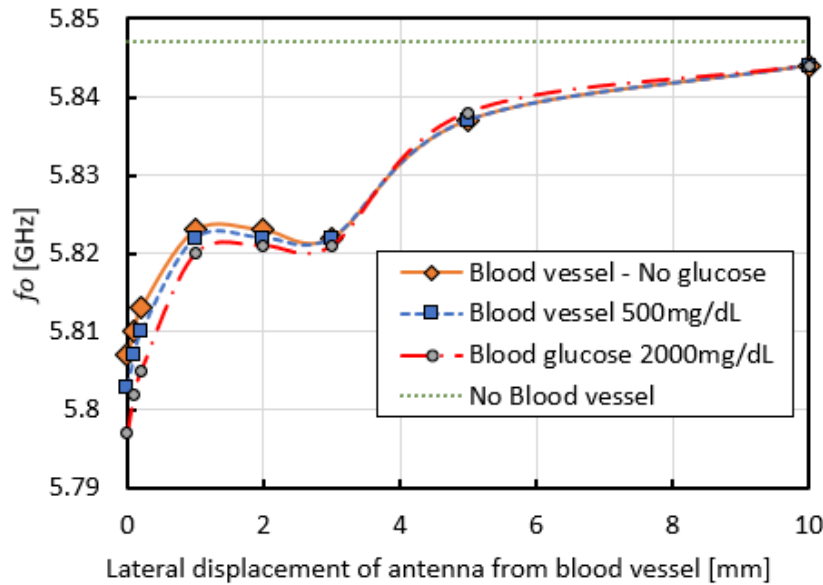


Figure 68: Simulated effect of antenna misaligned from blood vessel.

Note that the system response approaches that for no blood vessel, as expected, for large displacements.

Clearly the effect of mechanical misalignment of the sense antenna, even after variations in blood vessel depth and skin thickness have been calibrated out, is on par with the anticipated change in resonant frequency due to glucose variations. Fortunately a ‘mechanical alignment’ strategy has been developed to address this issue and will be presented in Chapter 4 where it is shown that an effective means for aligning the sense antenna with the blood vessel is both possible and very practical.

### 3.4 Chapter Summary

The sense antenna was simulated and tested using a human tissue oil-in-water gel phantom that mimics the dielectric properties ( $\epsilon_r$  and  $\sigma$ ) of skin, blood, fat and muscle. The dielectric properties of each human tissue phantom were achieved by adding oil to decrease the relative permittivity and adding salt to increase the electrical conductivity. D-glucose was added

to the blood phantom in proportions of 100, 300, 500, 1000 and 2000mg/dL. Each phantom was layered according to the human tissue model in which a blood vessel strip phantom was inserted inside the fat phantom, with a bottom muscle phantom and a top skin phantom. The antenna was fixed 2mm above the skin of the phantom using a constructed holder to ensure an even and constant distance was achieved. The experimental result from the sense antenna to the above mentioned variation of D-glucose level in the blood vessel was a 13MHz shift of resonant frequency, with a similar trend to the simulated results which predicted a 11MHz shift of resonant frequency.

Additional factors affect the resonant frequency of the non-invasive antenna and were explored. The skin thickness varies in each human and a variation from 2mm to 2.48 mm can produce a shift of resonant frequency up to 15MHz which is on the order of the glucose-dependent shift. In addition blood vessel depth variations also affect the sensor output to a similar degree. Fortunately this does not pose a problem, as the variations of D-glucose at the mentioned difference are still observed and a person's skin thickness and blood vessel location are constant for each person. To use the non-invasive antenna as a sensor, the glucose dependent equation should be calculated for each separate individual, thus these differences in tissue physiology can be calibrated out for each user. The antenna being further or closer to the skin than the optimal 2mm distance causes a variation in the return loss amplitude while lateral displacement from the blood vessel causes a lack of sensing functionality for a displacement of 1mm from the blood vessel. Thus properly placing the sense antenna over the blood vessel is critical to being able to measure blood glucose with this non-invasive sense antenna scheme. A practical strategy to ensure that the antenna is in proper alignment has been explored and will be presented in Chapter 4. Thus the research presented in this chapter indicates that it should indeed be possible to estimate blood glucose concentration in human blood using a non-invasive RF sense antenna provided that proper care to antenna placement on the upper arm of the patient is made and patient-to-patient tissue variations accounted for during system calibration.



## CHAPTER 4: GLUCOSE SENSOR SYSTEM

### 4.1 Chapter Overview

In this chapter an electronic system platform for implementing the non-invasive glucose sensing antenna as a complete sensor system is presented. The sensor system platform determines the blood glucose concentration of the blood vessel based on the measured shift of the resonant frequency of non-invasive antenna patch sensor in the Industrial, Scientific and Medical (ISM) Radio band (5.725GHz - 5.875GHz). The non-invasive blood glucose sensing system components and connections, the measurements taken on each component and between components/sub-systems, and a description of the algorithm used in the microcontroller to determine the blood glucose level are all described. Additionally, a calibration alternative for antenna misalignment correction by using lateral calibrating antennas is presented.

The system block diagram is shown below in Figure 69 with details provided in the next section. In words an RF generator is used to drive the antenna, with a fraction of its output coupled to both the antenna and receiver through a directional coupler. In this approach both the transmitted (FWD) and reflected (REF) power are processed by demodulating logarithmic amplifiers which convert the RF signals to corresponding voltages for downstream processing. Both inputs are then fed into a microcontroller and the measured shift in resonant frequency,  $f_0$ , is converted to a real-time glucose concentration which is displayed on the sensor LCD display.

### 4.2 System Platform Hardware

The first sensor system component is the signal source to drive the antenna(s) in the ISM band. This is an RF signal generator that generates frequencies from 5.725GHz to 5.875GHz in intervals of 1MHz every 20 $\mu$ s. This signal enters a bi-directional coupler with a nominal coupling

of 6dB and a forward directivity of 23dB. This is used to obtain continuous power reflection measurements from the non-invasive antenna in reference of the forward power for each frequency at its input. The forward and reflected coupled signals then feed separate demodulating logarithmic amplifiers to convert the RF input signal to a decibel-scaled output voltage with a nominal logarithmic slope of -25mV/dB [55]. The microcontroller processes the voltages from the demodulating logarithmic amplifiers to determine a blood glucose range based on the sampled measurements at different glucose level.

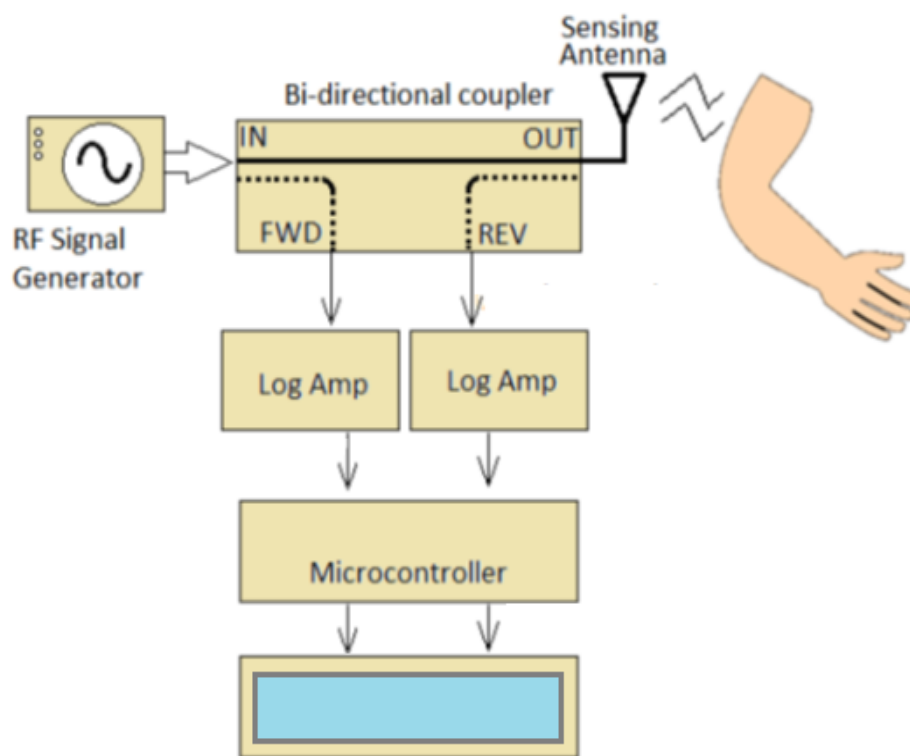


Figure 69: Block diagram of system platform for non-invasive sensing.

#### 4.2.1 Bi-Directional Coupler

The bi-directional coupler Amtery CP20008A, for frequencies from 0.5 to 8GHz, is a four-port network in which the traveling waves from the forward (through INPUT port) and the reverse (through OUTPUT port) are coupled to two ports (FWD Coupled and REV Coupled ports). A portion of the wave traveling from the INPUT port to the OUTPUT port is coupled to the FWD

coupled port but not to the REV coupled port, and a portion of the OUTPUT port is coupled to the REV coupled port but not the FWD coupled port. Figure 70 shows its electrical schematic [56] and the connection to the non-invasive blood glucose sensing system platform.

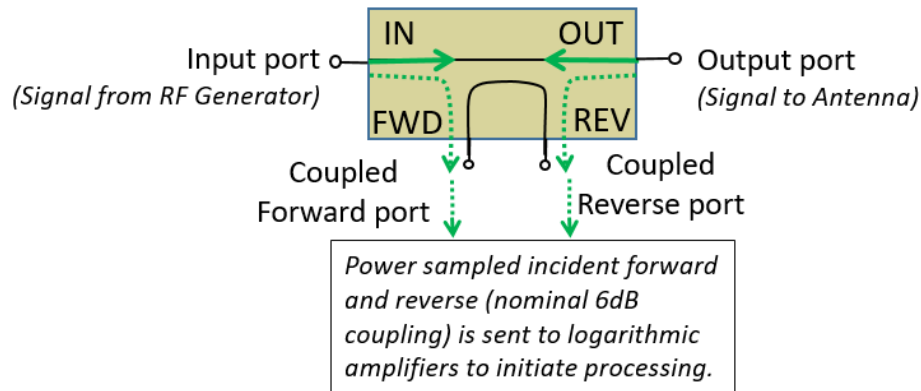


Figure 70: Bi-directional coupler port connections to the circuitry.

Coupling is a measure of how much of the incident power is sampled and it is expressed in decibels as  $10 \log \frac{P_{inc}}{P_{cp}}$ , where  $P_{inc}$  is the power incident and  $P_{cp}$  is the power coupled. The CP20008A bi-directional coupler has a nominal coupling factor of 6 dB for both forward and reverse coupling. The directivity measures the extent to which the coupler distinguishes between forward and reverse traveling waves. It is defined as the power output in the coupled port to the power flowing in the uncoupled port and is expressed in decibels as  $10 \log \frac{P_{cp}}{P_{dir}}$ . Ideally,  $P_{dir} = 0$  (Directivity is infinite as no power should couple to the auxiliary port).

In its full range of 0.5 to 8 GHz, the CP20008A has a nominal directivity of 23dB in the forward and 19dB in reverse direction [56]. The insertion loss, as well as the forward and reverse coupling, were measured by inserting a signal generated by the RF Explorer signal generator over the frequency range from 5.725GHz and 5.875GHz and is summarized in Figure 71. The measured insertion loss was -1.73dB and -1.76dB, the forward coupling was -6.3dB and -6.18dB, and the reverse coupling was -6.97dB and -6.85dB for frequencies 5.725GHz and 5.875GHz,

respectively. At the sensor center frequency of 5.8GHz, the measured forward directivity was 33dB and reverse directivity was 24dB.

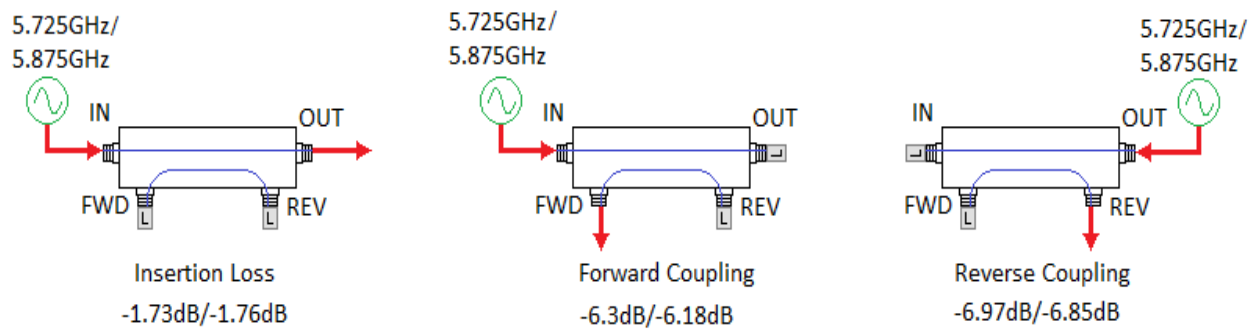


Figure 71: Measurements taken on coupler AMTERY model no. CP20008A.

a) Insertion loss, b) forward coupling, and c) reverse coupling.

The reverse port output was tested by inserting a signal in the INPUT port and driving the non-invasive antenna from the OUPUT port. The forward coupled port was connected to a 50Ω load and the reversed coupled port was connected to a network analyzer as shown in Figure 72. Frequencies of 5.725, 5.8 and 5.875GHz were injected and the signal at the reverse port measured under four conditions: 1) sense antenna in air, 2) antenna exposed to human tissue phantom without blood vessel, 3) antenna exposed to human tissue phantom with blood vessel containing 100mg/dL of glucose concentration, and 4) antenna exposed to human tissue phantom with a blood vessel containing 2000mg/dL of glucose concentration. The data was recorded to use for later microcontroller coding.

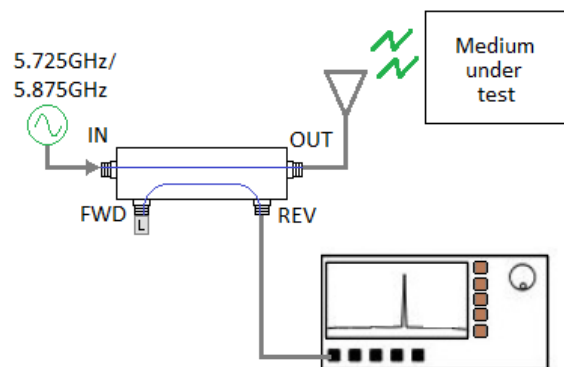


Figure 72: Measurement setup with bi-directional coupler and phantom.

The system was tested in the range of 5.725-5.875GHz for four mediums: 1) Air, 2) Human tissue phantom without blood vessel – no glucose, 3) Human tissue phantom with blood vessel - 100mg/dL glucose, and 4) Human tissue phantom with blood vessel - 2000mg/dL glucose.

#### 4.2.2 Demodulating Logarithmic Amplifier

The Analog Devices model no. AD8313 demodulating logarithmic amplifier consists of a 9-stage demodulating logarithmic amplifier, where each stage functions as a detector cell. The logarithmic amplifier, also called a logarithmic converter, compresses a signal of wide range to its decibel equivalence, thus converting the signal from one domain to another through a precise nonlinear transformation. It employs progressive compression in which a “cascade of nonlinear amplifier cells generates the logarithmic function from a series of contiguous segments” [55, 57]. The overall dc gain is high because the gain stages are dc-coupled. The device is fabricated using a SiGe bipolar IC process, and is available in a 4mm x 4mm 16 lead package (type LFCSP). The AD8318 is used in measurement mode to convert an RF input signal to a corresponding decibel-scaled output voltage, as  $V_{out}$  decreases linearly in dB with the RF input signal. In this mode a portion of  $V_{OUT}$  is fed back to  $V_{SET}$  [55]. The datasheet of the device specifies  $V_{OUT}$  with the following equation:

$$V_{OUT} = X \times V_{SLOPE/dB} \times 20 \times \log_{10} (V_{in}/V_{intercept}) \quad (6)$$

where  $X$  is the feedback factor in  $V_{SET} = V_{OUT} / X$ ,  $V_{SLOPE/dB}$  is nominally -25mV/dB, and  $V_{INTERCEPT}$  is 7dBV (20dBm, re: 50Ω or 2.239V<sub>rms</sub>).

The minimum value for  $V_{OUT}$  is  $V_{OUT} = X \times V_{OFFSET}$  where  $V_{OFFSET}$  is equal to 0.5V. The maximum value for  $V_{OUT}$  is  $V_{OUT} = 2.1 \times X$ , where  $V_{OUT}$  cannot exceed 400mV below the positive power supply voltage level. The non-invasive circuit prototype tested operated with a power supply of 5V, and with  $X=1$ , therefore, the voltage variation range of the logarithmic amplifier was 0.5V to 2.1V.

The manufacturer's datasheet specify a nominal  $V_{SLOPE/dB}$  -25mV/dB, but this can vary from device to device, so a board level calibration was performed.  $V_{OUT}$  can be expressed as

$$V_{OUT} = Slope \times (P_{IN} - Intercept) \quad (7)$$

where  $Slope = (V_{OUT1} - V_{OUT2}) / (P_{IN1} - P_{IN2})$  and  $Intercept = P_{IN1} - V_{OUT1}/Slope$ .

The device has a 10ns rise/fall time capability for input power switching between the noise floor and 0dB [57]. The CLPF was left unconnected and the integration function is provided by a 1.5pF on-chip capacitor. The output of each AD8318 was measured by connecting the input to the RF Explorer signal generator at 5.8GHz and at different power levels, in dBm, and measuring the corresponding  $V_{out}$  using an oscilloscope, as shown in Figure 73.

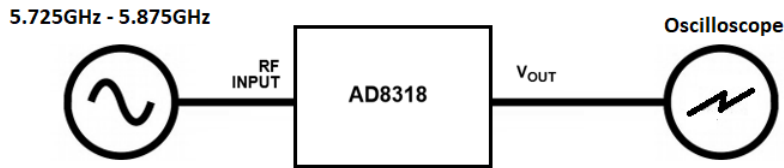


Figure 73: Setup to characterize the demodulating logarithmic amplifier AD8318. The RF Explorer was used as the source and a digital oscilloscope to capture the converted voltage waveform.

Figure 74 displays the measured  $V_{OUT}$  versus input signal power levels of -40, -30, -20, -10 and -5dBm. Note that the device used had a measured slope of -22.9mV/dB, as well as a parameter and variation error per measurement that needed to be considered during the coding of the system.

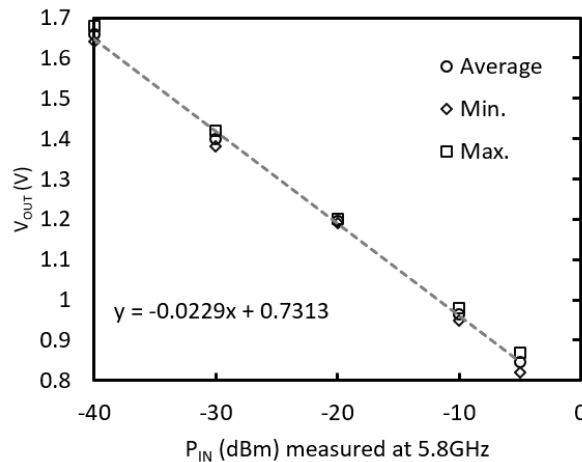


Figure 74: Measured  $V_{OUT}$  vs.  $P_{IN}$  (dBm) at 5.8GHz using the setup of Fig. 83. The observed slope is -22.9mV/dB which is within the specifications of the demodulating logarithmic amplifier.

Measurement setup is displayed in Figure 75, which was done with antenna facing air, on arm tissue without a blood vessel and with blood vessel at 500mg/dL. The results are displayed

in Figure 76. Note that when 50 ohm is loaded on the REV port of the bi-directional coupler, the FWD port is sufficiently constant for measurements in all three mediums to use as a reference signal. The REV signal can be observed with a high peak at 5.85 GHz with a value 1.56V for a phantom with no blood vessel (blue dashed line). The inversion of the signal from  $P_{OUT}$  to  $V_{OUT}$  is due to the discussed negative slope of -22.9mV/dB. When measuring antenna at phantom with blood vessel with glucose level of 500mg/dL, a peak can be observed at 5.875GHz. In contrast, when measuring antenna left measuring on empty air, the peak can be observed at 5.825GHz. This measurement is repeated at a later instance with the complete system, being recorded the highest peak at different frequencies for each of the mediums under test.

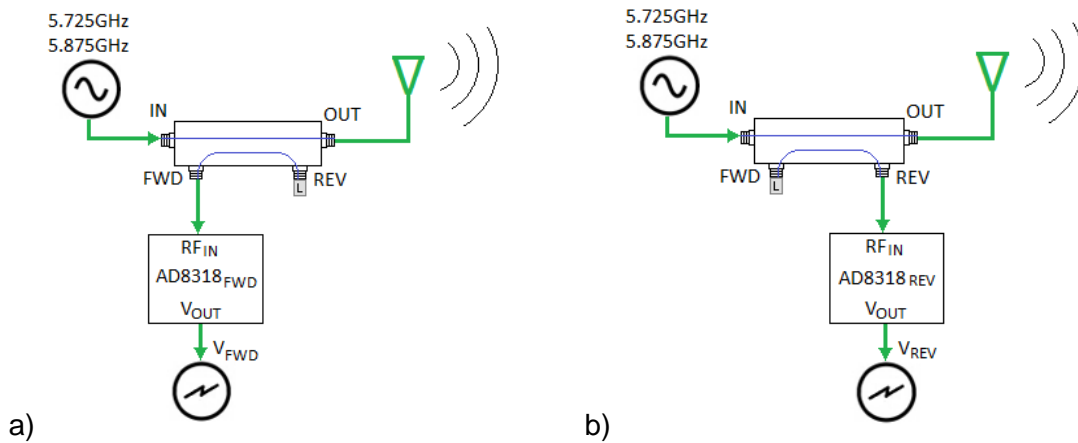


Figure 75: Measurement setup using the bi-directional coupler and logarithmic amplifier. a) For forward coupling and b) for reverse coupling.

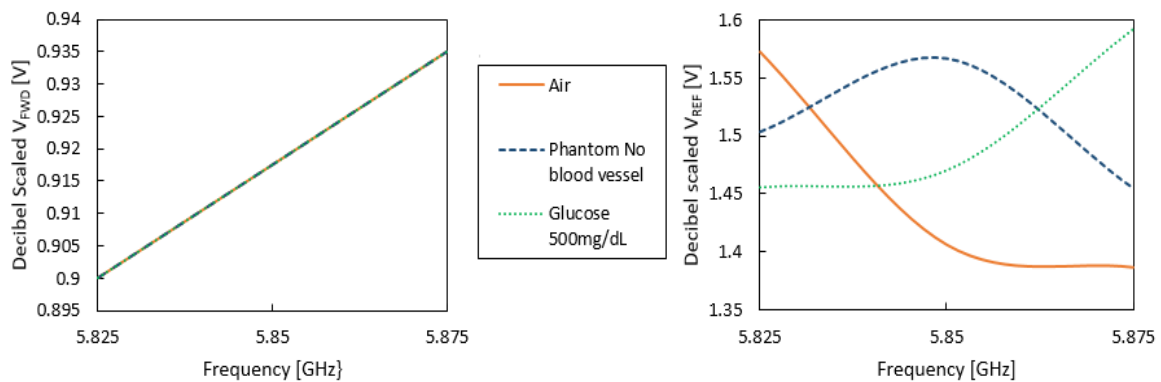


Figure 76: Preliminary test bi-directional coupler and the AD8318 for air, phantom without a blood vessel and phantom with blood vessel at 500mg/dL.

### 4.2.3 PIC Microcontroller 18F4221

The microcontroller used, Model No. PC18F4321 from microchip in the prototype research tests is an enhanced flash microcontroller with 10-bit Analog-to-Digital conversion (A/D) and utilizes low-power “nanowatt technology” [58]. Additional features that could be incorporated are communications via USART (Universal Synchronous and Asynchronous Receiver Transmitter) or SPI (Serial Peripheral Interface) to other devices and/or a computer. Note that the microcontroller was selected to test the prototype only and can be replaced by any microcontroller that fits the basic requirements of analog input and external visualization of glucose level (by LCD (liquid crystal display), cellphone, a computer, etc.). The dual in-line packaging (DIP) encapsulation was used only during initial prototype testing on breadboards. Further tests are to be implemented on a custom made printed circuit board (PCB), using the QFN (Quad Flat No-lead) encapsulation packaging option. The microcontroller was programmed to calculate an estimate of the glucose level based on the output voltages from the demodulating logarithmic amplifiers. The information was then displayed on an LCD. Two analog ports were connected to the output signals of the AD8318. Registers ADRESH and ADRESL, ADCON0, ADCON1 and ADCON2 were used to configure the ports and activate the analog to digital conversion process. The program toggles between two port conversion, where each analog port is processed and sampled. Each time one of the two channels are sampled, a minimum acquisition time is fulfilled before starting the conversion, where  $\frac{1}{2}$  Least Significant bit (LSb) error is used, having 1024 steps for the A/D conversion [58].

In short, the AD conversion requires an acquisition time, a conversion time, and a discharge time. The AD acquisition time depends on the amplifier settling time, the holding capacitor charging time and the temperature coefficient. The charge holding capacitor ( $C_{\text{HOLD}}$ ) is fully charged to the input channel voltage level before executing either conversion. This time is affected directly by the source impedance ( $R_s$ ) and the internal sampling switch ( $R_{\text{ss}}$ ). The  $C_{\text{HOLD}}$  is 25pF,  $R_s$  is 2.5K $\Omega$ , the conversion error is less than  $\frac{1}{2}$  LSb and  $V_{\text{DD}}$  is 5V [58].



The required times are therefore calculated as follows [58]:

$$T_{ACQ} = \text{Amplifier Settling Time } (T_{AMP}) + \text{Holding Capacitor Charging Time } (TC) + \text{Temperature Coefficient } (TC_{OFF})$$

and are calculated as described by the device fabrication specifications [58] listed here:

- $T_{AMP} = 0.2\mu s,$
- $TC = -(C_{HOLD})(R_{IC}+R_{SS}+R_S)\ln(1/2047) = (25pF)(1K\Omega+2K\Omega+2.5K\Omega)\ln(0.0004883) = 1.05\mu s$
- $TC_{OFF} = 0$  (working temperature of system below 25°C and does not require TC).

Once the acquisition time is fulfilled for the port (1.05μs as per above), the AD input conversion begins and a bit GO/DONE is cleared once the conversion is complete. The discharge initializes the value of the capacitor array. The time to complete a sampling conversion is therefore 1.25 μs.

#### 4.2.4 Glucose Meter Display

The non-invasive glucose estimate may then be displayed on a dedicated LCD screen, a computer, or even a smart phone. During prototype testing, the results were displayed on a 2 x 16-character LCD. Note that this LCD was used in initial tests only, and could be miniaturized by other LCD and will be discussed in the next subsection.

#### 4.2.5 System Platform Miniaturization

The non-invasive blood glucose sensor system could continue to be researched as a stand blood glucose measurement device in which a person introduces their arm into a measurement device located at a fixed station, or could be developed as a wearable device where the patient would carry the electronic device on their arm. In the case of a wearable device, the microcontroller can be replaced by the PIC16F720, version QFN 4x4, which is ideal for miniaturization purposes. This microcontroller is an extremely low power chip with a standby current of only 40 nA @ 1.8 V and has the peripheral I/O pins as well as the basic features needed

for this application including 128 bytes of non-volatile data storage, serial communication, an internal oscillator of 16MHz, and built-in ADC channels.

The display could be made using LCD with the sharp LS010B7DH01, for placement over the upper arm area. The dimensions are 1.64mm in thickness and 32.2 x 29.9 mm and the LCD is controlled via a serial interface, thus minimizing the interconnection with the microcontroller.

### 4.3 Non-Invasive Sensing Algorithm

In Figure 77 the sensing antenna return loss curve is represented on the right figure and analyzed at two frequencies in reference of the juxtaposed block diagram section on the left. If the RF Generator drives a frequency  $f_x$ , note that the return loss is at near 0dB. At this point the antenna isn't radiating and therefore most of the power is reflected back. Therefore, at frequency  $f_x$ , the output of the bi-directional coupler  $P_{REF}$  will be at its maximum level, and the difference between the  $P_{FWD}$  and  $P_{REF}$  will be at its minimum. On the other hand, at a frequency  $f_y$ , the antenna is at its deepest return loss point, meaning it is absorbing and radiating most of the power. At this frequency,  $P_{REF}$  will be at its minimum level, and the difference between the  $P_{FWD}$  and  $P_{REF}$  will be maximum. All frequencies between  $f_x$  and  $f_y$  will result in intermedium values.

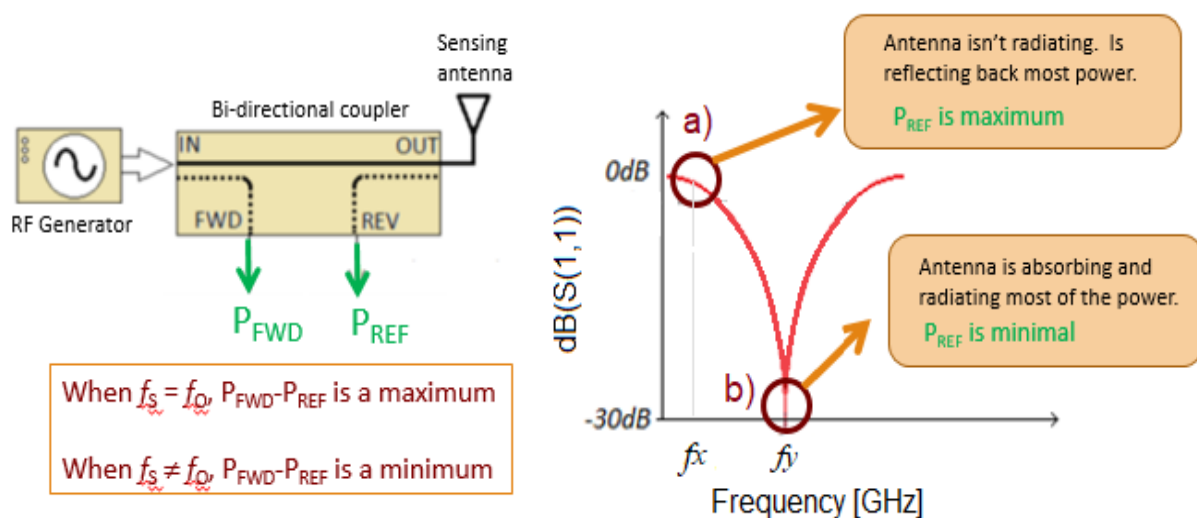


Figure 77: Antenna return loss power and bi-directional coupler output analysis. Note the highlight at frequencies  $f_x$  and  $f_y$  in the S11 representation (right) and the implications in the  $P_{FWD}-P_{REF}$  of the bi-directional coupler (left)

In essence, the algorithm consists of sweeping the frequencies between 5.725 and 5.875 GHz and calculating the difference between  $P_{FWD}$  and  $P_{REF}$ . The results of each sweep are recorded, and once the total differences at each frequency generated is computed, the result of maximum difference in the total log indicates that at that moment, the antenna was at its resonant frequency. To explain this, three scenarios will be discussed in which an antenna, when in proximity to medium 1, resonates at frequency  $f_1$ , when in proximity to medium 2 resonates at frequency  $f_2$  and when in proximity to medium 3 resonates at frequency  $f_3$ , where  $f_1 < f_2 < f_3$ , as displayed in Figure 78.

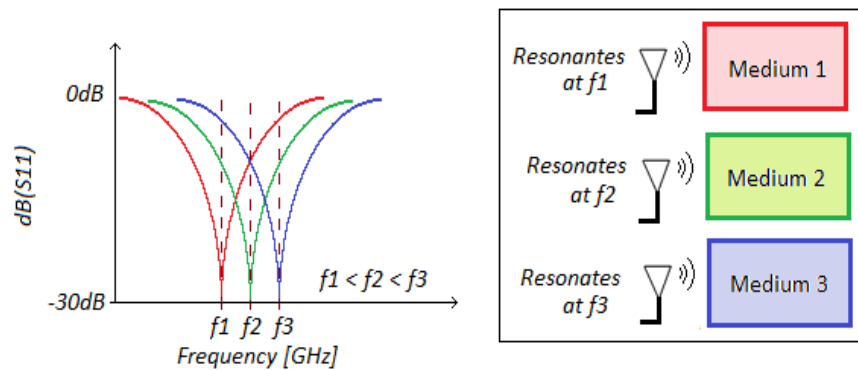


Figure 78: Illustration of antenna resonating at different frequencies per medium. Mediums 1, 2 and 3 make antenna resonate at frequencies  $f_1$ ,  $f_2$ , and  $f_3$ , respectfully.

If a frequency sweep  $f_1$ ,  $f_2$  and  $f_3$  is generated during times  $t_1$ ,  $t_2$  and  $t_3$ , in the case of the medium 1, the antenna is absorbing and radiating most of its power at  $f_1$ , so the reflected power will be at its lowest relative value during  $t_1$ . In contrast, when the generated signal is  $f_3$ , the antenna is reflecting back most of the power. For medium 1, the antenna will have its lowest power reflected (REV port) at frequency  $f_1$  during  $t_1$ . This can best be visualized representatively via the illustration in Figure 79. In contrast, if the same frequency sweep of  $f_1$ ,  $f_2$  and  $f_3$  is generated with medium 2, which resonates at frequency  $f_2$ , the antenna is absorbing and radiating most of its power during  $t_2$ , so during this time REV will have the lowest power measurement, as illustrated in Figure 79. If the frequency sweep is generated with medium 3, which resonates at  $f_3$ , the reflected power will be the lowest during  $t_3$  while generating  $f_3$ , as illustrated in Figure 81.

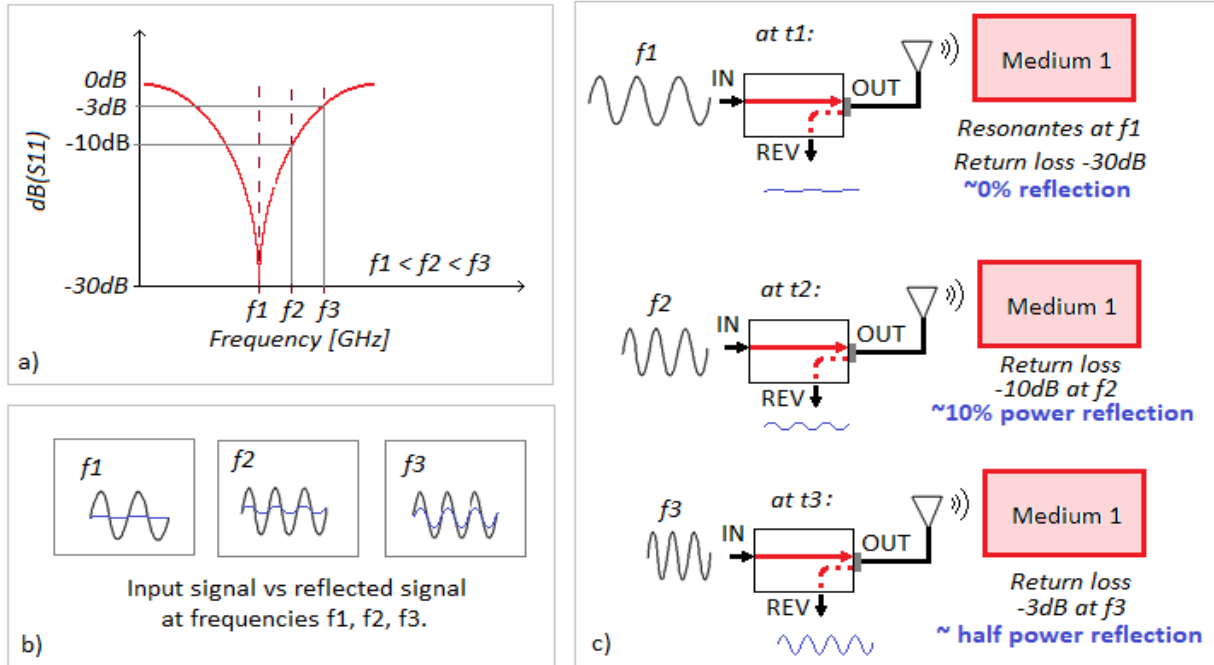


Figure 79: Block illustration of signal generated at frequencies  $f_1, f_2, f_3$  and antenna facing medium 1.

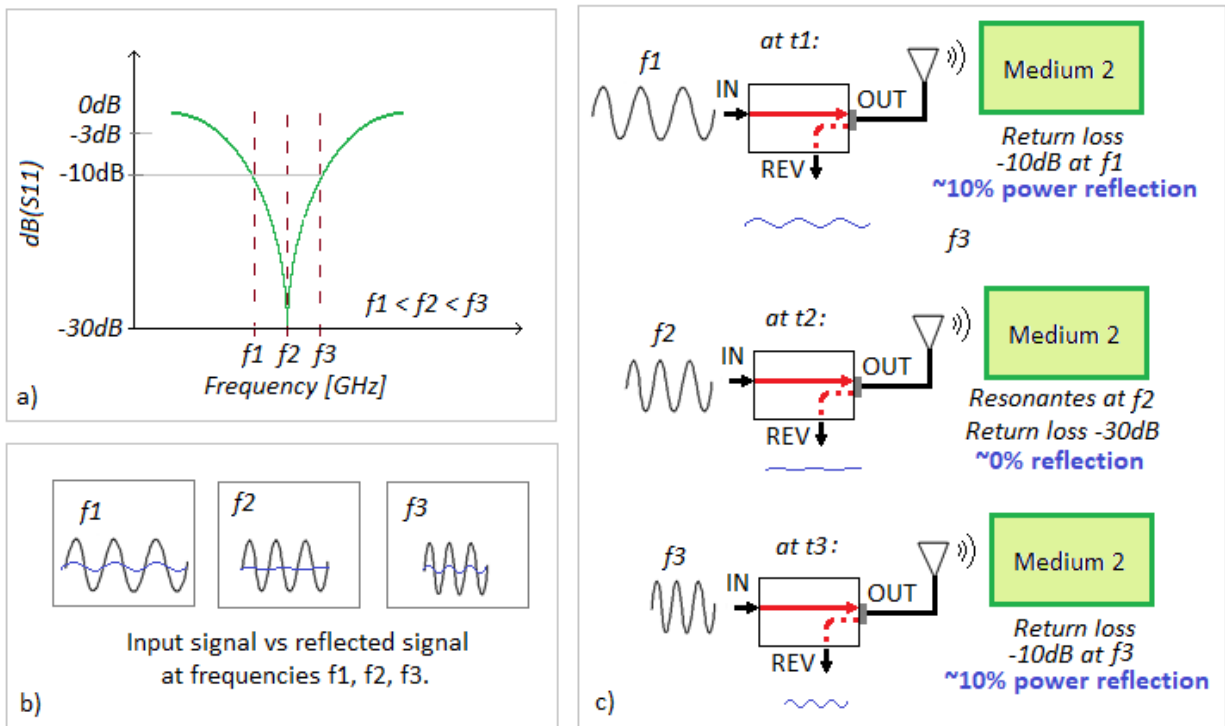


Figure 80: Block illustration of signal generated at frequencies  $f_1, f_2, f_3$  and antenna facing medium 2.

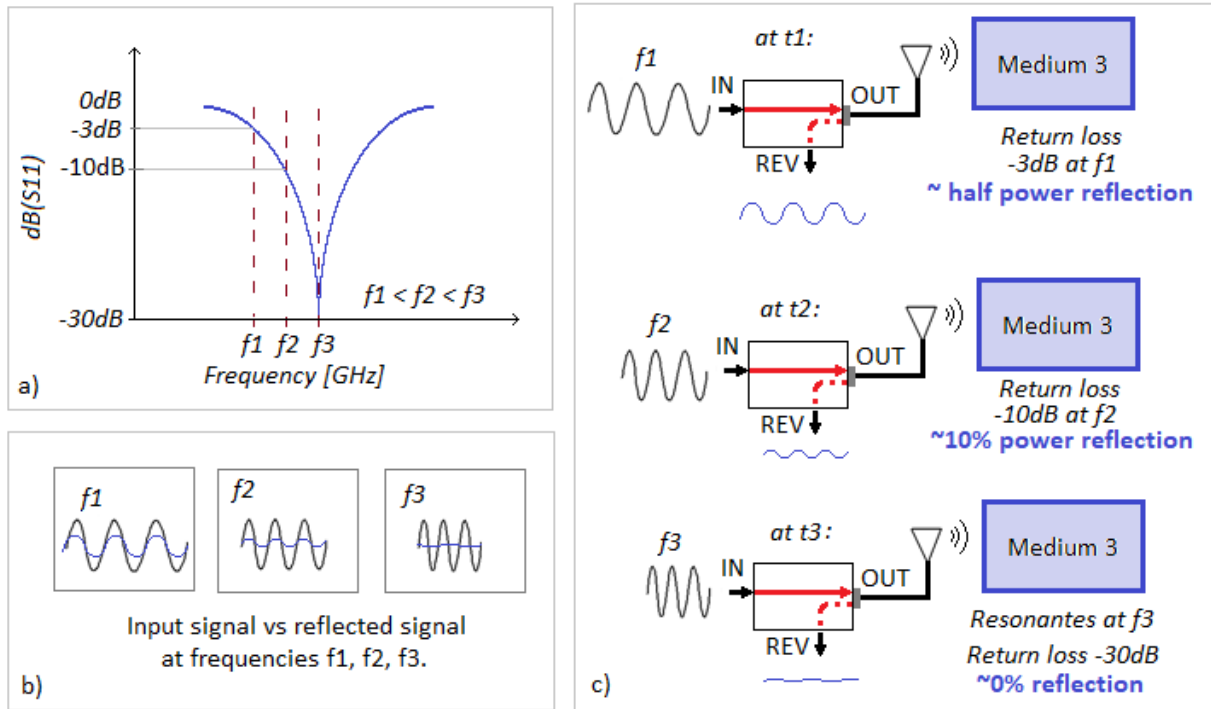


Figure 81: Block illustration of signal generated at frequencies  $f_1$ ,  $f_2$ ,  $f_3$  and antenna facing medium 3.

This algorithm may then be used to determine the resonant frequency of the antenna at signals generated between 5.725 and 5.875GHz for intervals of 1MHz (150 frequency sweeps), where the medium is the tissue phantom containing the blood vessel at a distinct glucose level. The coupled forward and reverse RF signals are converted to their corresponding decibel-scaled output voltage ( $V_{FWD}$  and  $V_{REV}$ ) by the logarithmic amplifier AD8318. Note that the logarithmic amplifier has a nominal negative slope of -25mV/dB, and was measured as shown in Figure 74. Therefore, the resonant frequency will be shown by a maximum  $V_{OUT}$  incoming from the REV port, which is referred to as  $V_{REV}$ . These voltages  $V_{REF}$  and  $V_{FWD}$  are input into analog ports AN0 and AN1 of the microcontroller. Figure 82 displays a block diagram of the microcontroller registers, where each AN0 and AN1 analog input is converted into a pair of registers ADRESH and ADRESL, which are transferred as registers FWDH and FWDL for incoming data from AN0s and REVH and REVL for incoming data from AN1.

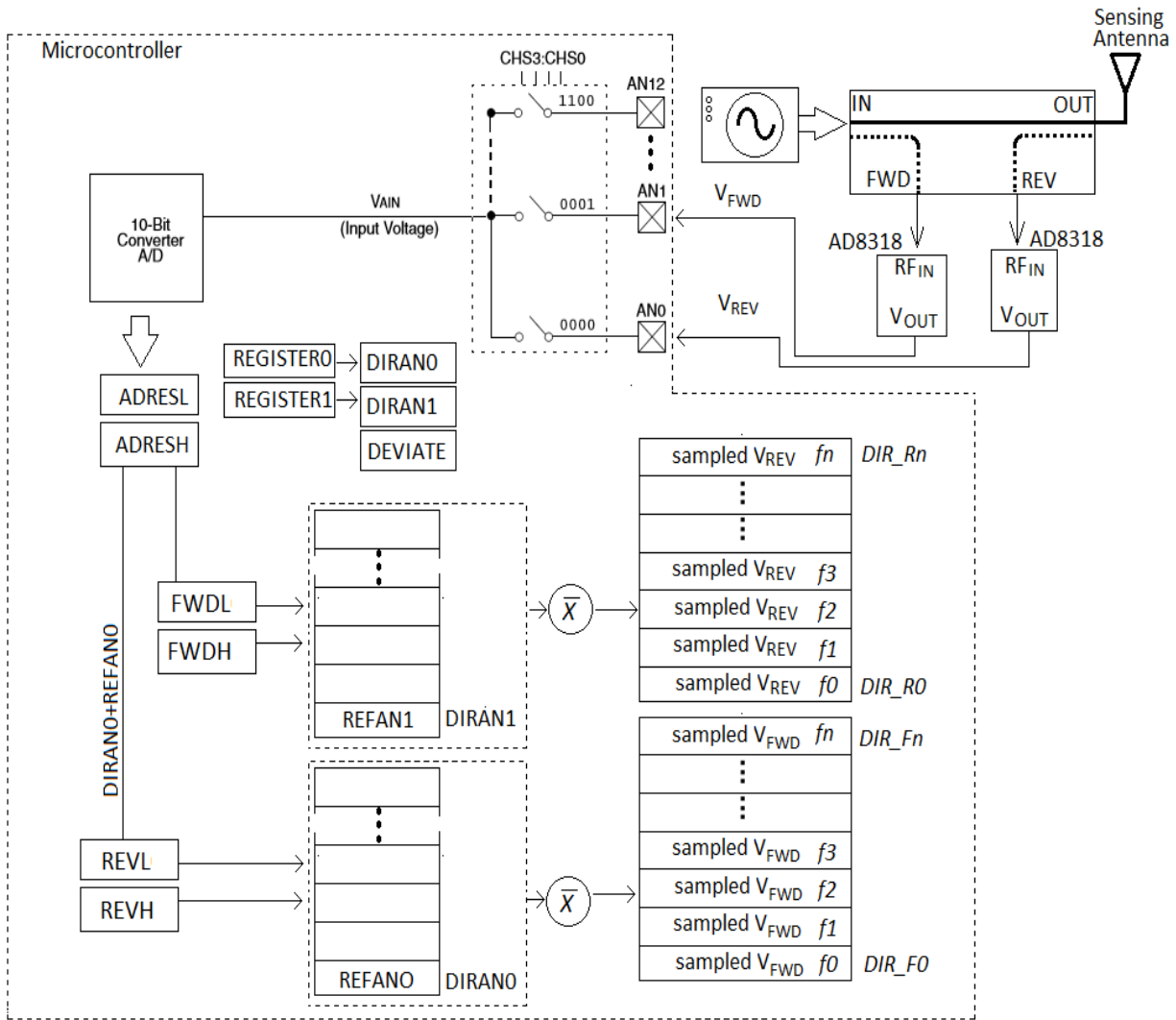


Figure 82: Non-invasive sensor system block diagram.  
Microcontroller AD conversion to memory storage block diagram (region inside dotted boundary).

The AD conversion is right justified, and variation only occurs in REVL and FWDL, but REVH and REVH are used in initially during the calibration and sampling of data. The sample data are stored in two memory sections for the current readings, where the addresses are referenced depending on the frequency that is driving the antenna. The previous average readings are stored in other two additional memory sections, where the addresses are also reference depending on the frequency. Once a new reading takes place, the reading is averaged with the stored previous readings, and the new value is stored in the memory section. Once the

frequency sweep is completed, the system processes the average and the current reading. During the next sweep, the new measurement is once again averaged to the previous reading. This continuous reading eliminates possible errors due to movement, instrument errors or any instantaneous error. In the average and current reading, the program looks for the maximum stored value and the address at which it was stored, which corresponds to a frequency. Based on this information, the system predicts the glucose levels based on a calibration measurement stored in the microcontroller.

An example of a test measurement of the three mediums was conducted at a frequency of 5.875GHz which three different mediums that resonate at 5.89, 5.87 and 5.8GHz, as shown in Figure 95. Signals at the forward and reverse coupled ports, at the voltage output ports of the logarithmic amplifier, and the expected register values of FWDL and REVL, were captured and the numerical values are shown in Figure 83.

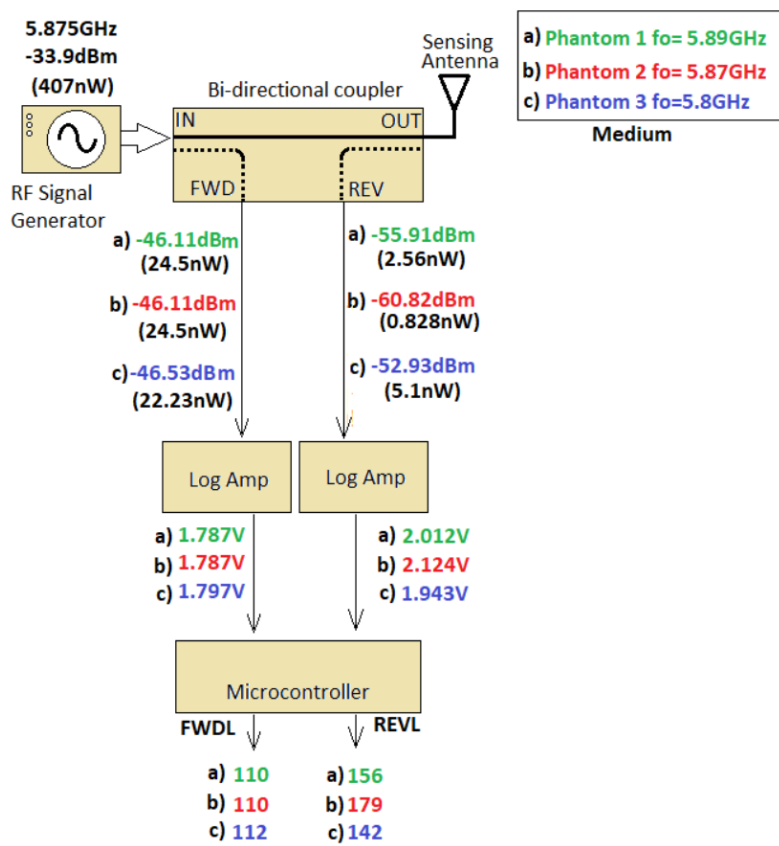


Figure 83: Sensor system test conducted at 5.875GHz for three different mediums.

Note that with medium phantom 2, the resonant frequency was closest to the frequency generated by the RF Signal generator as compared to the other phantoms. The output port REV drops to -60.82dBm, while for phantom 1 and 2 they are within -52 and -56dBm. The output of the Register REVL of the microcontroller will have the highest byte value at that instantaneous sampling during the program.

Once the program inputs signal data at each frequency from 5.725GHz to 5.825GHz, the program determines if it is valid data by analyzing if it is within a valid range stored in memory from a pre-calibrated program. The pre-calibrated system uses a parameter DEVIATE to calibrate the range of data deviation acceptance into the processing. The data will be continuously computed averaging the new incoming data with the last data stored in memory for each given frequency. These are stored in memory by indexing through assigned registers DIRAN0 and DIRAN1 which contain a reference registers REFANO and REFAN1 that act as pointers, which are averaged with previous stored data. Each average is stored in a second memory section for  $V_{FWD}$  cross-related to a third memory section for  $V_{REV}$ . Finally, the program determines the resonant frequencies by determining the highest ratio between  $V_{FWD}$  and  $V_{REV}$  and comparing this to a pre-calibrated set of values stored in memory. The information is output to the LCD for user observation. Figure 84 shows a picture of the system prototype during an air calibration routine.

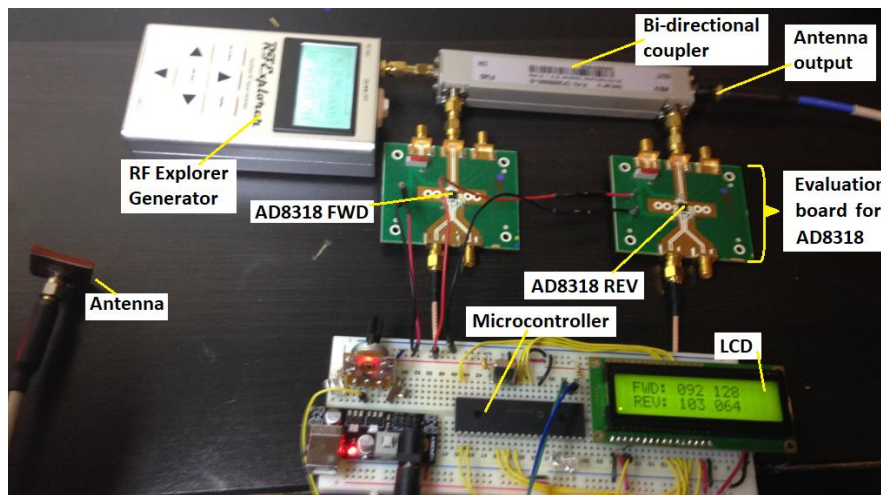


Figure 84: Photograph of the evaluation prototype for non-invasive glucose sensing with parts description.



The program was trial tested in-vitro using five mediums: 1) the sensor antenna facing air, 2) the sensor antenna 2mm above the pork tissue that mimicked surface of an arm with no blood vessel detected and 3-5) above the pork tissue with a with silicone hose to circulate mimicking blood with glucose levels 100mg/dL, 500mg/dL and 2000mg/dL (Figure 85). The program was run and was able to positively identify the different mediums under test.



Figure 85: Photograph of the evaluation prototype for non-invasive glucose sensing under test using pork tissue and mimicking liquid blood phantoms.

#### 4.4 Registration of Antenna Placement over Blood Vessel

The measured results are highly dependent on the correct positioning of the antenna with respect to the blood vessel, a point that was discussed theoretically in Chapter 3. For this, a registration strategy is proposed in which two lateral antennas would serve as a reference to position the sense antenna correctly. The registration strategy was simulated in ANSYS EM15.0 HFSS™, where three antenna patches are placed in a diagonal position from each other as shown in Figure 97 below.

The system was simulated using the simplified human tissue model, where the muscle and skin effect were disregarded, only analyzing the fat and blood vessel variation effect, to obtain preliminary results and test the viability of the proposed registration model. The  $S_{11}(1)$  (reflected power of centered sense antenna),  $S_{11}(2)$  (reflected power of antenna at side A), and  $S_{11}(3)$  (reflected power of antenna at side B) were computed for the blood vessel centered ( $dx=0$ ) and for it displaced by as much as 4 mm in intervals of 1 mm (i.e.,  $dx=1, 2, 3$  and  $4$ ) for each blood glucose level. It can be observed in Figure 86 and Figure 87, which shows the antennas in calibration model at  $dx=0, dx=1$  and  $dx=2$ , that the difference between the resonant frequency of calibrating antennas 2 and 3 is a minimum when the sensing antenna is centered over the blood vessel.

Only when the antenna is parallel and centered over the blood vessel will the return loss of the registration antennas approach the same resonant frequency with the same gain. Notice in Figure 88 that even when the blood vessel is crossing the center of the sensing antenna, because the blood vessel is not parallel to the patch antennas, the difference between the calibrating antennas 2 and 3 is 13MHz (Antenna 2 resonates at 5.809GHz and antenna 3 resonates at 5.822GHz). In contrast, in previous case of parallel blood vessel and patch, both antennas 2 and 3 resonated at 5.796GHz with the same minimum return loss peak. Therefore, this method can serve for alignment technique.

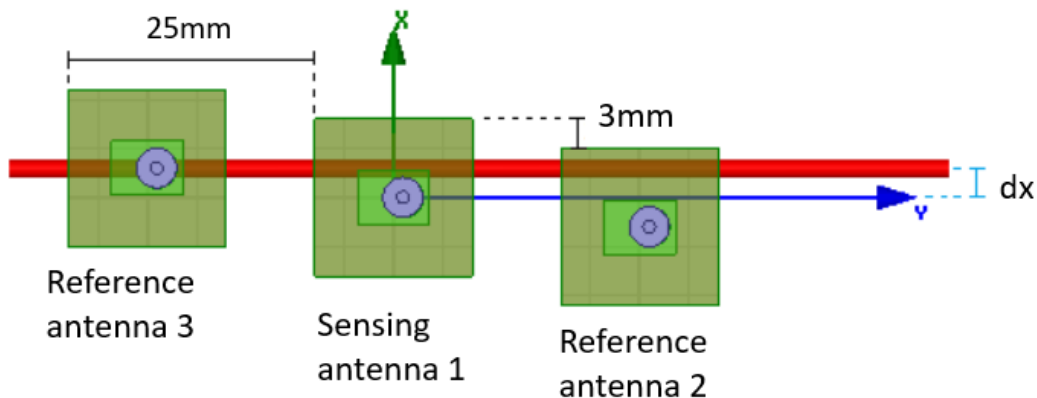


Figure 86: Top view of calibration model parallel to blood vessel. Two antennas are added at diagonal sides for sense antenna (center) registration.

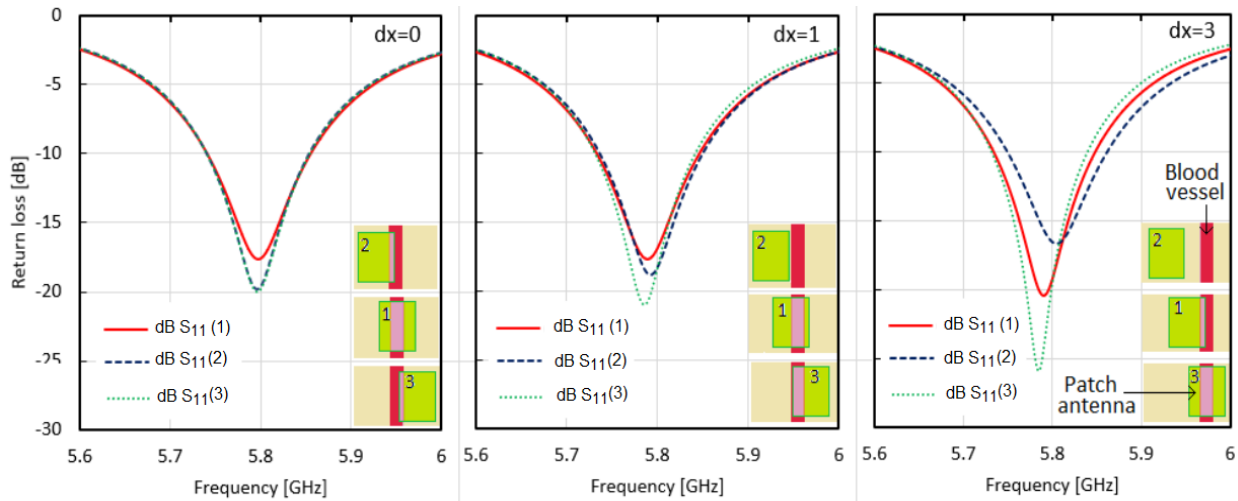


Figure 87: Return loss for sensing antenna and reference antennas..  
 a) Blood vessel centered with sensing antenna ( $dx=0$ ), b) Blood vessel displaced 1mm from sensing antenna ( $dx=1$ ), and c) Blood vessel displaced 3mm from sensing antenna ( $dx=3$ ).

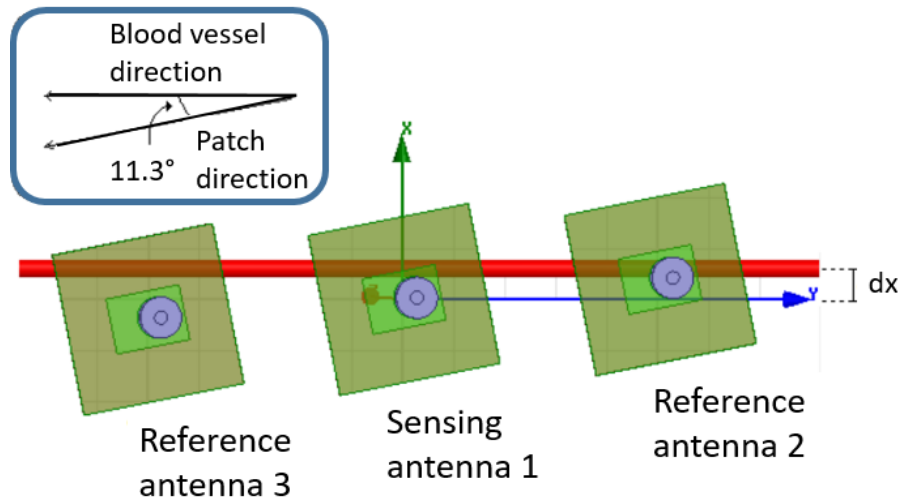


Figure 88: Top view of registration model at an angle with respect to the blood vessel. In this case a 13 MHz shift between the antennas 2 and 3 occurs. Thus this strategy can be used to both fix the proper angle as well as minimize any lateral offset, thus ensuring optimum sensor performance.

#### 4.5 Chapter Summary

A prototype system platform for a non-invasive blood glucose sensing system was designed, built and tested. A frequency sweep between 5.725 to 5.875GHz was generated by the RF Explorer Generator signal source and the signal coupled by a bi-directional coupler in forward and reverse directions. A demodulating logarithmic amplifier converts the frequency into

a decibel scaled voltage output. The microcontroller then converts each of the analog signals into digital data, stores them in memory, averages the results, and then samples and compares the data to calibration data in order to estimate the blood glucose level range. The total time of the entire frequency sweep and the analog to digital conversion and processing is performed in approximately 3 $\mu$ s with our prototype system and the estimated blood glucose displayed on a dedicated LCD screen. A registration strategy was also presented to allow the user to optimize the location of the antenna to minimize alignment errors thus increasing system sensitivity. This was accomplished by placing two additional 'registration' antennas in diagonal position with respect to the sense antenna. When the sense antenna is centered and parallel with the blood vessel, the registration antennas resonate at nearly the same value thus allowing for a null-point sensor patch alignment procedure to be implemented by the user.

## CHAPTER 5: CONCLUSIONS AND FUTURE WORK

### 5.1 Summary

The goal of this doctoral research was to explore the feasibility of an alternative blood glucose level monitoring device via an RF sensor antenna operating in one of the approved medical bands. This goal was explored by measuring the change in resonant frequency of an antenna patch in proximity to a blood vessel versus different glucose levels in the ISM band (5.725 – 5.875 GHz). The underlying concept was based on an antenna's resonant frequency being dependent on a medium's dielectric properties (relative permittivity and electrical conductivity) that is within the beam of the antenna. Since numerous previous works have demonstrated that blood relative permittivity decreases with an increase in blood glucose levels, this approach had merit but had never been fully explored and proven. Therefore this doctoral research represents a potential breakthrough in the quest to implement continuous glucose monitoring for patients suffering from diabetes.

The current research analyzed the effect of blood relative permittivity variation on the resonant frequency of an antenna in three different configurations: 1) Implanted as an active sensor, 2) Implanted as a passive sensor to be interrogated by external antenna(s), and 3) as a non-invasive sensor by placing the antenna above the upper arm skin. The antennas were designed using a 635 $\mu$ m thick Rogers 6010 substrate ( $\epsilon_r=10.2$ ,  $\tan \delta = 0.0023$ ). The research used the electromagnetic simulation tool Ansoft EM15.0 HFSS™ to model the antenna using realistic published human tissue physiological and electrical properties of skin, fat, blood and muscle. For the implantable active and passive sensor versions, the model was designed for the abdominal area of the body, whereby the antenna was to be implanted in a fatty tissue layer in close proximity to blood vasculature. For the non-invasive sensor, the antenna was designed for

the upper arm area to be above the skin and in line with the cephalic vein. Perfectly matched layer boundaries were set for each boundary layer of the human tissue model to eliminate electromagnetic reflection during all simulations.

The antenna patch was initially designed to operate at 5.8GHz in free space and later optimized to operate inside the body, for the active and passive sensor configurations, and at the external surface of the body for the non-invasive configuration. Antenna optimization was accomplished by varying the size of the patch antenna and the distance from the patch center to the feed. The resulting active antenna dimensions were a rectangular patch of 4.1x7.1mm over a substrate of 10mil thickness and 2.4x1.9cm in dimension, and with a feed displaced 1.4mm in the Y direction. The blood permittivity was varied from 62.0 to 63.6 in steps of 0.2 using a discrete sweep, resulting in a total resonance frequency variation for this range from 5.76 to 5.78 GHz, respectively (i.e., 20 MHz). In addition these results indicate that at greater glucose levels, the antenna will experience a decrease resonant frequency. The results indicated the potential of the antenna as an implantable sensor in this frequency band. To realize a blood glucose system, a circuit platform with batteries (or other energy source) would also need to be designed to be implanted in the body to make this functional. Therefore, further research and design of miniaturized circuitry for this approach would be required to bring this continuous glucose measuring system to the marketplace.

For the passive sensing approach, the implanted antenna was intended to be a stand-alone passive device inside the body, with no additional implanted circuitry or energy source such as batteries. The implanted antenna needed to perform two tasks: 1) to sense blood glucose levels inside the body by facing a major blood vessel, and 2) to communicate with two external antennas outside the body. The design of the active sensor fulfilled the first mentioned task. For the second task, a transmitting antenna needed to send the signal to the passive antenna, where it be reflected back to the receiving antenna with a shift in frequency corresponding to glucose level. Simulations of this concept were run by placing the external antennas in proximity of the

human tissue model separated by 1mm, 10mm and 20mm with no implant, and by adding implanted parts of the passive antenna in the fatty area at 2mm and at 7mm from blood vessel. When the antennas were separated by 1mm, an implant affected the  $S_{21}$  of the external antennas by less than 1dB at around the -12dB level. Having the antennas separated by 20 mm, although the implant affected the signal by about 10dB, the  $S_{21}$  signal was around the -40dB level. In conclusion, although there was less effect by having the antennas separated by 1mm, this separation distance allowed for a stronger signal. The blood permittivity was varied from 62.0 to 63.6. Unfortunately no variation was observed with the human tissue model based on blood variation in permittivity. The variations obtained were due to the location of the implant and not to the variation of blood glucose level. The test was repeated having a blood vessel in air boundaries, in which the  $S_{21}$  signal variation was based on blood glucose variation but less than 1MHz. No conclusive positive results were obtained to pursue further the passive implant approach. Furthermore, this approach also requires an implant and requires external circuitry, which makes this the least practical option for commercial use.

The third and final method that was explored was the non-invasive approach, in which an antenna patch was placed externally over the upper arm in direct line of sight of a blood vessel. The blood relative permittivity was again varied, with an increase in resonance frequency as the blood relative permittivity increased observed. Variation of  $\epsilon_r$  from 51.397 to 52.642 in the blood vessel caused a resonant frequency variation of approximately 10.5MHz on the antenna, which is the principal reason why this last sensing approach underwent further research to compare with simulated results.

The experimental tests of the non-invasive antenna approach were conducted using an oil-in-gel phantom that mimicked the dielectric properties ( $\epsilon_r$  and  $\sigma$ ) of skin, blood, fat and muscle, and an arm tissue model was constructed using each layer. The recipe was a modified version from published works by altering the proportions of oil and salt in the phantom to obtain the desired relative permittivity and electrical conductivity at frequencies from 5.725 to 5.875GHz. D-glucose

was added to the blood phantom in proportions of 100, 300, 500, 1000 and 2000mg/dL which caused a measured variation of  $\epsilon_r=52.635$  to  $\epsilon_r=51.482$ , which were approximated to  $\epsilon_r$  from 52.64 to 51.40 for numerical simulation purposes. Once the desired electrical properties for each tissue layer was achieved, the human tissue model was constructed by inserting the blood vessel as a strip phantom inside the fat phantom, with a bottom muscle phantom and a top skin phantom. The antenna was then located 2mm above the skin using a constructed holder to ensure even and fixed distance between the antenna and the arm. The experimental results with the mentioned variation of D-glucose level in the blood vessel resulted in a 13MHz shift of resonant frequency, with a similar fit trend as the simulated results. This, in a general sense, was validation of the numerical model executed in HFSS™ and justification for further development of the non-invasive sensor approach.

Further tests were carried out to determine the effect of variations that exist between different people, such as skin thickness and blood vessel depth, and variations due to any misalignment of the sense antenna with respect to the blood vessel. It was found that skin thickness variation from the 2mm to 2.48 mm can produce a shift of resonant frequency up to 15MHz. Depth variation was evaluated for extreme differences of 1mm of the blood vessel location, which can cause up to a 50MHz variation. Nevertheless, we do not believe that the skin and vessel depth variation from different individuals poses a problem, as these variables are stable for each person, and the variation due to D-glucose at the mentioned difference were still observed. Naturally proper sensor calibration would need to be performed by the medical professional when fitting the sensor system to the patient. To use the non-invasive antenna as a glucose sensor, the glucose dependent equation should be calculated for each separate individual and calibrated for each person. Misalignment of antenna was also determined by displacing the antenna further or closer to the skin, and by displacing it laterally away from the blood vessel. Although vertical misalignment does not produce significant variation in frequency, it does produce variations in the peak minimum of the resonant frequency, and must be stabilized



due to the technique used in the system to determine the resonant frequency. The distance from the skin can be stabilized by having the antenna in a holder that ensures a 2mm distance from the skin. The lateral displacement had a significant variation if not correctly aligned with the blood vessel. This can be corrected by a registration mechanism in which two additional antennas placed above and below the sense antenna, and in a diagonal direction, serve to alert the user of any a misplacement of the antenna so the user or caregiver could correctly re-align the sensing antenna.

Finally, an electronic system platform to implement the non-invasive sensing antenna was designed in which a circuit system platform determined the blood glucose concentration in a blood vessel based on the shift of the resonant frequency of a non-invasive antenna patch sensor in the Industrial, Scientific and Medical (ISM) Radio band (5.725GHz - 5.875GHz). An RF generator was used to drive the antenna, with a fraction of its output coupled to both the antenna and receiver through a directional coupler. The transmitted and received RF power were converted to a decibel scaled output voltage and fed into a microcontroller. The microcontroller processed the data to display the estimated glucose concentration on a dedicated LCD screen.

## **5.2 Recommendations and Future Work**

The active sensing antenna has the potentiality to undergo further research. In this configuration, the antenna was evaluated as a sensing device only, but did not include any research on the internal circuitry and the communication with outside the body. To be implanted inside the body, the antenna would need to be constructed using a biocompatible material such as Silicon Carbide, such as evaluated by research in references [23] and [28]. Furthermore, this antenna would need an energy source and circuitry. The energy source could derive from energy harvesting or could be an implanted battery. When a glucose level is above or below a specified level, the antenna should be able to communicate with an external device to alert the patient, or

be able to have control mechanisms to correct the problem such controlling the output of an insulin pump such as is displayed in Figure 86.

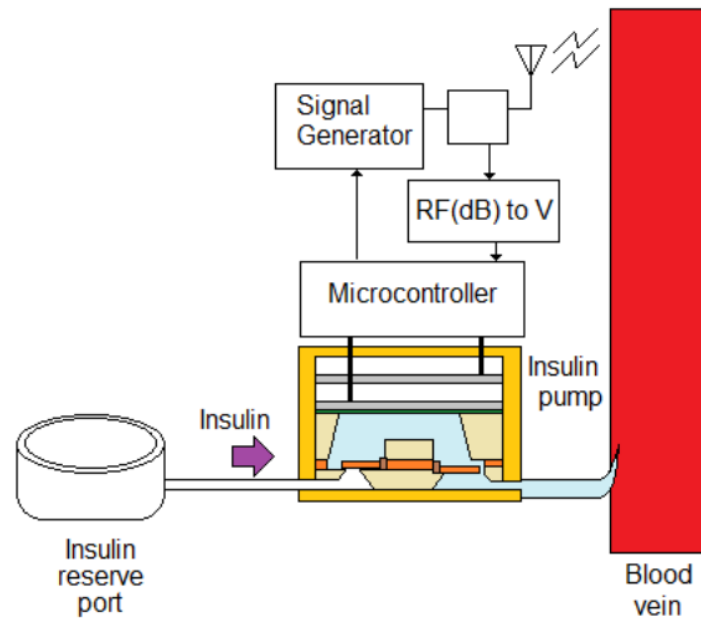


Figure 89: Implantable blood glucose sensing system to control insulin pump.

A second further work consists in additional research for the non-invasive antenna. In this path, an analysis needs to be conducted on different patients to obtain real time data on different areas of the arm, categorized by age, sex, weight, and other factors that distinguish each patient under test. The data should be cross referenced with the glucose level and health conditions of the patient. This can be added in the calibration program. All simulations done in this research could be repeated using the basilic vein instead of the cephalic vein, and other major veins in the body and compare the results with the ones presented on this research. Additional tests such as temperature variation of patient should also be evaluated. Further work include the miniaturization of the prototype for a wearable device application, or the construction as a stand-alone device where an arm can be inserted in a tubular device with an antenna or several antennas within, as displayed in Figure 90. As the patient inserts the arm, the tubular device could rotate, or could be stationary and have multiple antennas inside the tube, where sampling is activated one at a time. The sampling of different sections of the arm can add accuracy.

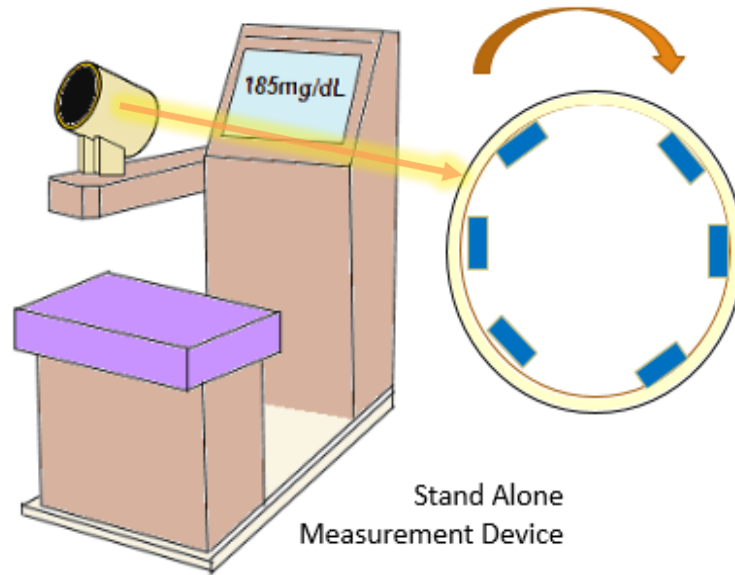


Figure 90: Stand-alone glucose monitoring system with antennas in tubular device. The tubular device could rotate or have added antennas for additional measurement points for added accuracy due to multiple arm reference points.

## REFERENCES

- [1] "Executive Summary: Standards of Medical Care in Diabetes," *Diabetes Care*, p. 36, 2013.
- [2] "Fast Facts: Data and Statistics about diabetes," 2014. [Online]. Available: <http://www.diabetes.org/diabetes-basics/statistics/>.
- [3] P. Holt, "Blood Glucose Monitoring in Diabetes," *Nursing Standard*, vol. 28, no. 27, pp. 52-58, 2014.
- [4] L. Czupryniak, L. Barkai, S. Bolgarska, A. Bronisz, J. Broz, J. Cypriak, M. Honka, A. Janez, M. Kric, N. Lalic, E. Martinka, D. Rahelic, G. Roman, T. Tankova, T. Vakoyi, B. Wolnik and N. Zherdova, "Self-Monitoring of Blood Glucose in Diabetes: From Evidence to Clinical Reality in Central and Eastern Europe," *Diabetes Technology and Therapeutics*, vol. 16, no. 7, 2014.
- [5] A. Alzaid, C. Schlaeger and R. Hinzmann, "6th Annual Symposium on Self Monitoring of Blood Glucose Applications and Beyond," *Diabetes Technology and Therapeutics*, vol. 15, no. 7, 2014.
- [6] W. Myers, "Managing Diabetes With Continuous Glucose Monitoring," *Everyday Health Media, LLC*, 12 02 2013.
- [7] The Cleveland Clinic Foundation, "Non-invasive Monitors and Glucose Sensors: What's New.," 2005.
- [8] Abbott, "Your FreeStyle Libre Pro Sensor - What you need to know," Abbott, October 2016. [Online]. Available: <http://www.freestylelibrepro.us/patients.html>. [Accessed 17 October 2017].
- [9] MikeH, "Apple Creating an iWatch That Could Monitor Glucose?!", *Diabetes Mine*, 2013.
- [10] B. Freer, *Feasibility of a Non-invasive Wireless Blood Glucose Monitor*, Thesis/Dissertation collections at RIT Scholar Works, 2011.
- [11] Trademarkia, "Trademark Document Retrieval: Glucoband," United States Patent and Trademark Office - An agency of the Department of Commerce, 2013. [Online]. Available: <http://www.trademarkia.com/glucoband-85547810.html>. [Accessed 1 July 2014].
- [12] BioSensors, inc., "Capabilities: BioSensors Technology," 2016. [Online]. Available: <http://www.biosensors-tech.com/>. [Accessed 17 May 2016].
- [13] Freedom Meditech, Inc, "I-Sugar X Meditech," 2012. [Online]. Available: <http://www.freedom-meditech.com>. [Accessed 14 07 2013].
- [14] EyeSense, "Easy Check, Positive ID EyeSense," 2010. [Online]. Available: [http://www.positiveidcorp.com/products\\_easycheck.html](http://www.positiveidcorp.com/products_easycheck.html). [Accessed 2014 July 2014].
- [15] EyeSense, "Minimal Invasive Blood Glucose Measurement," 2014. [Online]. Available: <http://en.eyesense.com/product/eyesense-technology-precise-glucose-monitoring-at-the-eye/product-information/>. [Accessed 14 July 2014].
- [16] Glucotrack, "In the News: Integrity Applications, Inc. enters into Manufacturing Agreement with Wistron Corp.," 2014. [Online]. Available: <http://www.integrity-app.com/inthenews/integrity-applications-inc-enters-into-manufacturing-agreement-with-wistron-corp-2>. [Accessed 14 July 2014].

- [17] D. Scout, "Verelight Inc.," 2014. [Online]. Available: <http://www.verelight.com/products.html>. [Accessed 14 July 2014].
- [18] C. So, K. Choi, T. Wong and J. Chung, "Recent Advances in Noninvasive Glucose Monitoring," *Dovepress*, vol. 2012:5, pp. 45-52, 29 June 2012.
- [19] "Grove Instruments," 2010. [Online]. Available: <http://groveinstruments.com>. [Accessed 14 July 2014].
- [20] "Orsense," 2014. [Online]. Available: <http://www.orsense.com>. [Accessed 01 05 2016].
- [21] N. Oliver, C. Toumazou, A. Cass and D. Johnston, "Glucose sensors: a review of current and emerging technology," *Diabetic Medicine*, vol. 26, no. 3, pp. 197-210, 2009.
- [22] Y. Onuki, U. Bhardwaj, U. Pharm, F. Papadimitrakopoulos and D. Burgess, "A Review of Biocompatible Implantable Devices: Current Challenges to Overcome Foreign Body Response," *Journal of Diabetes Society Technology*, vol. 2, no. 6, pp. 1003-1015, 2008.
- [23] S. Afroz, "A Biocompatible SiC RF Antenna for In-Vivo Sensing Applications," Ph.D. Dissertation, University of South Florida, Florida, 2013.
- [24] H. Koschwanetz and W. Reichert, "In Vitro, In Vivo and Post Explantation Testing of Glucose-Detecting Biosensors: Current Methods and Recommendations.," *Biomaterials*, vol. 28, no. 25, pp. 3687-3703, 2007.
- [25] A. Skrivervik and F. Merli, "Design Strategies for Implantable Antenna," *Antennas and Propagation Conference (LAPC)*, pp. 1-5, 14-15 November 2011.
- [26] M. Hoskins, "GlySens (Still) Developing Implantable CGM," Healthline, 5 May 2014. [Online]. Available: <http://www.healthline.com/diabetesmine/glysens-developing-implantable-cgm-see-also-icgm>. [Accessed 1 May 2016].
- [27] E. Topsakal, T. Karacolak and E. C. Moreland, "Glucose-Dependent Dielectric Properties of Blood Plasma," in *General Assembly and Scientific Symposium URSI*, Istanbul, 2011.
- [28] S. Afroz, S. W. Thomas, G. Mumcu and S. E. Saddow, "Implantable SiC based RF antenna biosensor for continuous glucose monitoring," in *IEEE sensors*, Baltimore, Maryland, 2013.
- [29] S. Saha, I. Sotiriou, I. Gouzouasis, H. Cano-Garcias, G. Palikaras and P. Kosmas, "Evaluation of the Sensitivity of Transmission Measurements at Millimeter Waves using Patch Antennas for Non-invasive Glucose," in *10th European Conference on Antennas and Propagation*, Davos, Switzerland, 2016.
- [30] V. Turgul and I. Kale, "Characterization of the Complex Permittivity of Glucose/Water Solutions for Noninvasive RF/Microwave Blood Glucose Sensing," in *IEEE Xplore*, Taipei, Taiwan, 2016.
- [31] T. Yilmaz, R. Foster and Y. Hao, "Broadband Tissue Mimicking Phantoms and a patch resonator for Evaluating Noninvasive Monitoring of Blood Glucose Levels," *IEEE transactions on Antennas and Propagation*, vol. 62, no. 6, pp. 3064-3075, 2014.
- [32] F. Araujo Cespedes, G. Mumcu and S. E. Saddow, "SiC RF Sensor for Continuous Glucose Monitoring," in *Material Research Society*, Phoenix, Arizona, 2016.
- [33] C. Gabriel, G. S and E. Corthout, "The dielectric properties of biological tissues: I. Literature survey," *Physics in Medicine and Biology*, vol. 41, pp. 2231-2249, 1996.
- [34] J. Park, C. Kim, B. Choi and K. Ham, "The correlation of the complex dielectric constant and blood glucose at low frequency," *Biosensors and Bioelectronics*, vol. 19, pp. 321-324, 2003.

- [35] T. Karacolak, A. Hood and E. Topsakal, "Design of a Dual-Band Implantable Antenna and Development of Sin Mimicking Gels for Continuous Glucose Monitoring," *IEEE Transactions on Microwave Theory and Techniques*, vol. 56, no. 4, pp. 1001-1008, 2008.
- [36] M. Wolf, R. Guilich, P. Lunkenheimer and A. Loidl, "Broadband Dielectric Spectroscopy of Human Blood," *Biochimica et Biophysica Acta*, vol. 1810, pp. 727-740, 2011.
- [37] D. Andreuccetti, R. Fossi and C. Petrucci, "Calculations of the Dielectric properties of human tissue," Institute for applied physics Nello Carrara Florence Italy, 1997-2015. [Online]. Available: <http://niremf.ifac.cnr.it/tissprop/htmlclie/htmlclie.php>. [Accessed 5 January 2017].
- [38] S. Gabriel, R. W. Lau and C. Gabriel, "The dielectric properties of biological tissues:III. Parametric models for the dielectric spectrum of Tissues," *Phys. Med. Biol.*, vol. 41, pp. 2271-2293, 1996.
- [39] T. Karacolak, E. Moreland and E. Topsakal, "Cole-Cole Model for Glucose-Dependent Dielectric Properties of Blood Plasma for Continuous Monitoring," *Microw. Opt Technol. Letter*, vol. 55, no. 5, pp. 1160-1164, 2013.
- [40] M. A. Gibney, C. H. Arce, K. J. Byron and L. J. Hirsch, "Skin and subcutaneous adipose layer thickness in adults with diabetes at sites used for insulin injections: implications for needle length recommendations," *Current Medical Research & Opinion*, vol. 26, no. 6, pp. 1519-1530, 2010.
- [41] Medtronic, "Insertion Site Management: Selecting the Best Sensor Site," Medtronic MiniMed, Inc, 2016. [Online]. Available: <http://www.medtronicdiabetes.com>. [Accessed 20 May 2016].
- [42] D. S. Teyhen, J. L. Rieger, R. B. Westrick, A. C. Miller, J. M. Molloy and J. D. Childs, "Changes in Deep Abdominal Muscle Thickness During Common Trunk-Strengthening Exercises Using Ultrasound Imaging," *Journal of Orthopaedic & Sports Physical Therapy*, vol. 38, no. 10, pp. 596-605, 2008.
- [43] S. Joing, S. Strote, L. Caroon, C. Wall, J. Hess, C. Roline, L. Oh, B. Dolan, R. Poutre, K. P. D. Carney and R. Reardon, "Ultrasound-Guided Peripheral IV Placement," *The New England Journal of Medicine*, vol. e38, no. Videos in Clinical Medicine, p. 366, 21 June 2012.
- [44] S. M. Jain, A. Lahoti, K. Pandey and R. Kiran, "Evaluation of skin and subcutaneous tissue thickness at insulin injection sites in Indian, insulin naïve, type-2 diabetic adult population," *Indian Journal of Endocrinology and Metabolism*, vol. 17, no. 5, pp. 864-870, 2013.
- [45] R. N. Planken, X. H. Keuter, A. P. Hoeks and K. J. P. al, "Diameter measurements of the forearm cephalic vein prior to vascular access creation in end-stage renal disease patients: graduated pressure cuff versus tourniquet vessel dilatation.," *Nephrol Dial Transplant*, pp. 802-806, 21 March 2006.
- [46] J. C. Costa Baptista-Silva, A. Lourenco Dias, S. Vincezo Cricenti and E. Burihan, "Anatomy of the Basilic Vein in the Arm and its importance for surgery," *Braz. Journal Morphol. Sci*, vol. 20, no. 3, pp. 171-175, 2003.
- [47] M. Hubal, H. T. P. Gordish-Dressman, T. H. E. Price, T. Angelopoulos, P. M. N. Gordon, L. Pescatello, P. Visich, Z. RF, R. Seip and P. Calkson, "Variability in muscle size and strength gain after unilateral resistance training," *PubMed.gov*, vol. 37, no. 6, pp. 964-972, 2005.
- [48] R. Ogasawara, R. Thiebaud, J. Loenneke, M. Loftin and T. Abe, "Time course for arm and chest muscle thickness changes following bench press training," *Interv Med Appl Sci*, vol. 4, no. 4, pp. 217-220, 2012.

- [49] M. Miyatani, H. Kanehisa, M. Ito, Y. Kawakami and F. T, "The accuracy of volume estimates using ultrasound muscle thickness measurements in different muscle groups," *European Journal of Applied Physiology*, vol. 91, no. 2-3, pp. 264-272, 2004.
- [50] Ansys, "Ansys HFSS," Ansys, Inc., 2016. [Online]. Available: <http://www.ansys.com/Products/Electronics/Ansys-HFSS>. [Accessed 10 May 2016].
- [51] T. Kobayahi, T. Nojima, K. Yamanda and S. Uebayashi, "Dry phantom composed of ceramics and its application to SAR estimation," *IEEE Trans. Microw Theory Techn*, vol. 34, no. 6, pp. 671-680, 1986.
- [52] A. A. Bakar, D. Ireland, A. Abbosh and Y. Wang, "Microwave imaging of heterogeneous breast phantoms using ultra-wideband system," *Prog. Electromagn. Res. M*, vol. 23, no. 1, pp. 109-121, 2012.
- [53] A. Mobashsher, A. M. Abbosh and Y. Wang, "Microwave system to detect traumatic brain injuries using compact unidirectional antenna and wideband transceiver with verification on realistic head phantom," *IEEE Trans. Microw. Theory Techn.*, vol. 62, no. 9, pp. 1826-1836, 2014.
- [54] Agilent Technologies, *Agilent Basics of Measuring the Dielectric Properties of Materials. Application Note.*, USA: Agilent Technologies, 2014.
- [55] Analog Devices, *AD8318 Logarithmic Detector/Controller*, Norwood, MA: Analog Devices, 2004-2017.
- [56] Amtery, *Amtery CP20008A-6*, Taipei, Taiwan: [www.amtery.com](http://www.amtery.com), 2017.
- [57] Analog Devices, *AD8307 Datasheet*, Norwood, MA: Analog Devices, 2004-2017.
- [58] Microchip, *PIC18f4321 Family*, Microchip Technology, 2006.
- [59] B. Puttkammer, "Continuous Glucose Monitor (CGM) Setup and Insert Walk Through," [Online]. Available: <http://youtu.be/ReZX7rLi5D8>. [Accessed 25 August 2014].
- [60] F. H. Netter, *Atlas of Human Anatomy*, Philadelphia: Saunders Elsevier, 2014.
- [61] Y. E. Mohammed and A. G. Saber, "Estimation of E-Field inside Muscle Tissue at MICS and ISM Frequencies Using Analytic and Numerical Methods," *Journal of Biomedical Engineering and Technology*, vol. 2, no. 3, pp. 29-33, 2014.
- [62] S. Johnson, "Notes on Perfectly Matched Layer," MIT, notes, Massachusetts, 2007, updated 2010.
- [63] Nearfield Systems, Inc, "Nearfield Systems: Gain and Directivity," 2016. [Online]. Available: <http://ww2.nearfield.com>. [Accessed 1 May 2016].
- [64] A. Neumann, *Kinesiology of the Musculoskeletal System*, 2nd ed., Missouri: Mosby Elsevier Press, 2010, p. 390.
- [65] W. W. Hurd, J. Duke and T. Falcone, "Clinical gate," 11 04 2015. [Online]. Available: <http://clinicalgate.com/gynecologic-laparoscopy/>. [Accessed 14 06 2016].
- [66] B. Chinnock, S. L. Thornton and G. W. Hendey, "Predictors of Success in Nurse-Performed Ultrasound-Guided Cannulation," *Journal of Emergency Medicine*, vol. 33, no. 4, pp. 401-405, 2007.
- [67] B. Cummings, *Human Anatomy and Physiology*, San Francisco: Addison Wesley Longman, Inc., 2001.
- [68] K. Casey, T. B. H, K. Mannava, R. Noll, S. R. Money and W. C. Sternbergh, "basilic vein transposition diameter of 4.9," *J Vasc Surg*, pp. 402-206, February 2008.
- [69] N. P. S. Sandhu and D. S. Sidhu, "Mid-arm approach to basilic and cephalic vein cannulation using ultrasound guidance," *British Journal of Anaesthesia*, vol. 93, no. 2, pp. 292-294, 2004.

- [70] Boundless, "Veins of the Upper Limbs. Boundless Anatomy and Physiology.," Boundless, 23 October 2016. [Online]. Available: <https://www.boundless.com/physiology/textbooks/boundless-anatomy-and-physiology-textbook/cardiovascular-system-blood-vessels-19/circulatory-routes-189/veins-of-the-upper-limbs-944-2203/>. [Accessed 11 November 2016].
- [71] "KENHUB," KEN HUB, [Online]. Available: <https://www.kenhub.com>. [Accessed 28 November 2016].
- [72] R. A. a. S. D. M. Center, "WIKIPEDIA," [Online]. Available: [www.wikipedia.com](http://www.wikipedia.com). [Accessed 28 November 2016].
- [73] A. M. Asbeutah, "Anatomy of the Upper Limb," 14 February 2013. [Online]. Available: [www.slideshare.net](http://www.slideshare.net). [Accessed 1 December 2016].
- [74] Microchip Technology Inc., *PIC16(L)F720/721*, Microchip, 2010-2015.
- [75] Avnet, *Sharp LS010B7DH01*, Avnet, 2010.
- [76] HITACHI, "HD44780U," Hitachi, Ltd., Chiyoda-Ku, Tokyo, 2010.



## APPENDIX A: PERMISSION FOR MATERIAL IN CHAPTER 2

### CAMBRIDGE UNIVERSITY PRESS LICENSE TERMS AND CONDITIONS

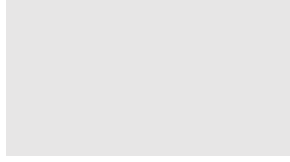
Nov 03, 2017

This Agreement between FABIOLA ARAUJO ("You") and Cambridge University Press ("Cambridge University Press") consists of your license details and the terms and conditions provided by Cambridge University Press and Copyright Clearance Center.

License Number	4221210126743
License date	Nov 03, 2017
Licensed Content Publisher	Cambridge University Press
Licensed Content Publication	MRS Advances
Licensed Content Title	SiC RF Sensor for Continuous Glucose Monitoring
Licensed Content Author	Fabiola Araujo Cespedes, Gokhan Mumcu, Stephen E. Saddow
Licensed Content Date	May 23, 2016
Licensed Content Volume	1
Licensed Content Issue	55
Start page	3691
End page	3696
Type of Use	Dissertation/Thesis
Requestor type	Author
Portion	Full article
Author of this Cambridge University Press article	Yes
Author / editor of the new work	Yes
Order reference number	
Territory for reuse	North America Only
Title of your thesis / dissertation	RF Sensing System for Continuous Glucose Monitoring
Expected completion date	Dec 2017
Estimated size(pages)	107
Requestor Location	FABIOLA ARAUJO
Publisher Tax ID	
Billing Type	
Billing Address	

Total

Terms and Conditions



### TERMS & CONDITIONS

Cambridge University Press grants the Licensee permission on a non-exclusive non-transferable basis to reproduce, make available or otherwise use the Licensed content 'Content' in the named territory 'Territory' for the purpose listed 'the Use' on Page 1 of this Agreement subject to the following terms and conditions.

1. The License is limited to the permission granted and the Content detailed herein and does not extend to any other permission or content.
2. Cambridge gives no warranty or indemnity in respect of any third-party copyright material included in the Content, for which the Licensee should seek separate permission clearance.
3. The integrity of the Content must be ensured.
4. The License does extend to any edition published specifically for the use of handicapped or reading-impaired individuals.
5. The Licensee shall provide a prominent acknowledgement in the following format:  
author/s, title of article, name of journal, volume number, issue number, page references,  
, reproduced with permission.

Other terms and conditions:

v1.0

Questions? [customercare@copyright.com](mailto:customercare@copyright.com) or +1-855-239-3415 (toll free in the US) or +1-978-646-2777.



## APPENDIX B: PERMISSION FOR FIGURE 4

### ELSEVIER LICENSE TERMS AND CONDITIONS

Nov 03, 2017

This Agreement between FABIOLA ARAUJO ("You") and Elsevier ("Elsevier") consists of your license details and the terms and conditions provided by Elsevier and Copyright Clearance Center.

License Number	4221211240842
License date	Nov 03, 2017
Licensed Content Publisher	Elsevier
Licensed Content Publication	Biosensors and Bioelectronics
Licensed Content Title	The correlation of the complex dielectric constant and blood glucose at low frequency
Licensed Content Author	J.-H. Park,C.-S. Kim,B.-C. Choj,K.-Y. Ham
Licensed Content Date	Dec 15, 2003
Licensed Content Volume	19
Licensed Content Issue	4
Licensed Content Pages	4
Start Page	321
End Page	324
Type of Use	reuse in a thesis/dissertation
Intended publisher of new work	other
Portion	figures/tables/illustrations
Number of figures/tables/illustrations	1
Format	both print and electronic
Are you the author of this Elsevier article?	No
Will you be translating?	No
Original figure numbers	Fig. 4. The glucose concentration dependence of $\epsilon'$ (a) and $\epsilon''$ (b) at 10 kHz for water/glucose systems. Solid lines are guides line.
Title of your thesis/dissertation	RF Sensing System for Continuous Glucose Monitoring
Expected completion date	Dec 2017
Estimated size (number of pages)	107
Requestor Location	FABIOLA ARAUJO
Publisher Tax ID	

Total **0.00 USD**

Terms and Conditions

#### INTRODUCTION

1. The publisher for this copyrighted material is Elsevier. By clicking "accept" in connection with completing this licensing transaction, you agree that the following terms and conditions apply to this transaction (along with the Billing and Payment terms and conditions established by Copyright Clearance Center, Inc. ("CCC"), at the time that you opened your Rightslink account and that are available at any time at <http://myaccount.copyright.com>).

#### GENERAL TERMS

2. Elsevier hereby grants you permission to reproduce the aforementioned material subject to the terms and conditions indicated.

3. Acknowledgement: If any part of the material to be used (for example, figures) has appeared in our publication with credit or acknowledgement to another source, permission must also be sought from that source. If such permission is not obtained then that material may not be included in your publication/copies. Suitable acknowledgement to the source must be made, either as a footnote or in a reference list at the end of your publication, as follows:

"Reprinted from Publication title, Vol /edition number, Author(s), Title of article / title of chapter, Pages No., Copyright (Year), with permission from Elsevier [OR APPLICABLE SOCIETY COPYRIGHT OWNER]." Also Lancet special credit - "Reprinted from The Lancet, Vol. number, Author(s), Title of article, Pages No., Copyright (Year), with permission from Elsevier."

4. Reproduction of this material is confined to the purpose and/or media for which permission is hereby given.

5. Altering/Modifying Material: Not Permitted. However figures and illustrations may be altered/adapted minimally to serve your work. Any other abbreviations, additions, deletions and/or any other alterations shall be made only with prior written authorization of Elsevier Ltd. (Please contact Elsevier at [permissions@elsevier.com](mailto:permissions@elsevier.com)). No modifications can be made to any Lancet figures/tables and they must be reproduced in full.

6. If the permission fee for the requested use of our material is waived in this instance, please be advised that your future requests for Elsevier materials may attract a fee.

7. Reservation of Rights: Publisher reserves all rights not specifically granted in the combination of (i) the license details provided by you and accepted in the course of this licensing transaction, (ii) these terms and conditions and (iii) CCC's Billing and Payment terms and conditions.

8. License Contingent Upon Payment: While you may exercise the rights licensed immediately upon issuance of the license at the end of the licensing process for the transaction, provided that you have disclosed complete and accurate details of your proposed use, no license is finally effective unless and until full payment is received from you (either by publisher or by CCC) as provided in CCC's Billing and Payment terms and conditions. If full payment is not received on a timely basis, then any license preliminarily granted shall be deemed automatically revoked and shall be void as if never granted. Further, in the event that you breach any of these terms and conditions or any of CCC's Billing and Payment terms and conditions, the license is automatically revoked and shall be void as if never granted. Use of materials as described in a revoked license, as well as any use of the materials beyond the scope of an unrevoked license, may constitute copyright infringement and publisher reserves the right to take any and all action to protect its copyright in the materials.

9. Warranties: Publisher makes no representations or warranties with respect to the licensed material.

10. Indemnity: You hereby indemnify and agree to hold harmless publisher and CCC, and their respective officers, directors, employees and agents, from and against any and all claims arising out of your use of the licensed material other than as specifically authorized pursuant to this license.

11. No Transfer of License: This license is personal to you and may not be sublicensed, assigned, or transferred by you to any other person without publisher's written permission.

12. No Amendment Except in Writing: This license may not be amended except in a writing signed by both parties (or, in the case of publisher, by CCC on publisher's behalf).

13. Objection to Contrary Terms: Publisher hereby objects to any terms contained in any purchase order, acknowledgment, check endorsement or other writing prepared by you, which terms are inconsistent with these terms and conditions or CCC's Billing and Payment terms and conditions. These terms and conditions, together with CCC's Billing and Payment terms and conditions (which are incorporated herein), comprise the entire agreement between you and publisher (and CCC) concerning this licensing transaction. In the event of any conflict between your obligations established by these terms and conditions and those established by CCC's Billing and Payment terms and conditions, these terms and conditions shall control.

14. Revocation: Elsevier or Copyright Clearance Center may deny the permissions described in this License at their sole discretion, for any reason or no reason, with a full refund payable to you. Notice of such denial will be made using the contact information provided by you. Failure to receive such notice will not alter or invalidate the denial. In no event will

Elsevier or Copyright Clearance Center be responsible or liable for any costs, expenses or damage incurred by you as a result of a denial of your permission request, other than a refund of the amount(s) paid by you to Elsevier and/or Copyright Clearance Center for denied permissions.

#### LIMITED LICENSE

The following terms and conditions apply only to specific license types:

**15. Translation:** This permission is granted for non-exclusive world **English** rights only unless your license was granted for translation rights. If you licensed translation rights you may only translate this content into the languages you requested. A professional translator must perform all translations and reproduce the content word for word preserving the integrity of the article.

**16. Posting licensed content on any Website:** The following terms and conditions apply as follows: Licensing material from an Elsevier journal: All content posted to the web site must maintain the copyright information line on the bottom of each image; A hyper-text must be included to the Homepage of the journal from which you are licensing at <http://www.sciencedirect.com/science/journal/xxxxx> or the Elsevier homepage for books at <http://www.elsevier.com>; Central Storage: This license does not include permission for a scanned version of the material to be stored in a central repository such as that provided by Heron/XanEdu.

Licensing material from an Elsevier book: A hyper-text link must be included to the Elsevier homepage at <http://www.elsevier.com> . All content posted to the web site must maintain the copyright information line on the bottom of each image.

**Posting licensed content on Electronic reserve:** In addition to the above the following clauses are applicable: The web site must be password-protected and made available only to bona fide students registered on a relevant course. This permission is granted for 1 year only. You may obtain a new license for future website posting.

**17. For journal authors:** the following clauses are applicable in addition to the above:

#### Preprints:

A preprint is an author's own write-up of research results and analysis, it has not been peer-reviewed, nor has it had any other value added to it by a publisher (such as formatting, copyright, technical enhancement etc.).

Authors can share their preprints anywhere at any time. Preprints should not be added to or enhanced in any way in order to appear more like, or to substitute for, the final versions of articles however authors can update their preprints on arXiv or RePEc with their Accepted Author Manuscript (see below).

If accepted for publication, we encourage authors to link from the preprint to their formal publication via its DOI. Millions of researchers have access to the formal publications on ScienceDirect, and so links will help users to find, access, cite and use the best available version. Please note that Cell Press, The Lancet and some society-owned have different preprint policies. Information on these policies is available on the journal homepage.

**Accepted Author Manuscripts:** An accepted author manuscript is the manuscript of an article that has been accepted for publication and which typically includes author-incorporated changes suggested during submission, peer review and editor-author communications.

Authors can share their accepted author manuscript:

- immediately
  - via their non-commercial person homepage or blog
  - by updating a preprint in arXiv or RePEc with the accepted manuscript
  - via their research institute or institutional repository for internal institutional uses or as part of an invitation-only research collaboration work-group
  - directly by providing copies to their students or to research collaborators for their personal use
  - for private scholarly sharing as part of an invitation-only work group on commercial sites with which Elsevier has an agreement
- After the embargo period
  - via non-commercial hosting platforms such as their institutional repository
  - via commercial sites with which Elsevier has an agreement

In all cases accepted manuscripts should:

- link to the formal publication via its DOI
- bear a CC-BY-NC-ND license - this is easy to do
- if aggregated with other manuscripts, for example in a repository or other site, be shared in alignment with our hosting policy not be added to or enhanced in any way to appear more like, or to substitute for, the published journal article.

**Published journal article (JPA):** A published journal article (PJA) is the definitive final record of published research that appears or will appear in the journal and embodies all value-adding publishing activities including peer review co-ordination, copy-editing, formatting, (if relevant) pagination and online enrichment.

Policies for sharing publishing journal articles differ for subscription and gold open access articles:

**Subscription Articles:** If you are an author, please share a link to your article rather than the full-text. Millions of researchers have access to the formal publications on ScienceDirect, and so links will help your users to find, access, cite, and use the best available version.

Theses and dissertations which contain embedded PJAs as part of the formal submission can be posted publicly by the awarding institution with DOI links back to the formal publications on ScienceDirect.

If you are affiliated with a library that subscribes to ScienceDirect you have additional private sharing rights for others' research accessed under that agreement. This includes use for classroom teaching and internal training at the institution (including use in course packs and courseware programs), and inclusion of the article for grant funding purposes.

**Gold Open Access Articles:** May be shared according to the author-selected end-user license and should contain a [CrossMark logo](#), the end user license, and a DOI link to the formal publication on ScienceDirect.

Please refer to Elsevier's [posting policy](#) for further information.

18. **For book authors** the following clauses are applicable in addition to the above: Authors are permitted to place a brief summary of their work online only. You are not allowed to download and post the published electronic version of your chapter, nor may you scan the printed edition to create an electronic version. **Posting to a repository:** Authors are permitted to post a summary of their chapter only in their institution's repository.

19. **Thesis/Dissertation:** If your license is for use in a thesis/dissertation your thesis may be submitted to your institution in either print or electronic form. Should your thesis be published commercially, please reapply for permission. These requirements include permission for the Library and Archives of Canada to supply single copies, on demand, of the complete thesis and include permission for Proquest/UMI to supply single copies, on demand, of the complete thesis. Should your thesis be published commercially, please reapply for permission. Theses and dissertations which contain embedded PJAs as part of the formal submission can be posted publicly by the awarding institution with DOI links back to the formal publications on ScienceDirect.

#### **Elsevier Open Access Terms and Conditions**

You can publish open access with Elsevier in hundreds of open access journals or in nearly 2000 established subscription journals that support open access publishing. Permitted third party re-use of these open access articles is defined by the author's choice of Creative Commons user license. See our [open access license policy](#) for more information.

#### **Terms & Conditions applicable to all Open Access articles published with Elsevier:**

Any reuse of the article must not represent the author as endorsing the adaptation of the article nor should the article be modified in such a way as to damage the author's honour or reputation. If any changes have been made, such changes must be clearly indicated.

The author(s) must be appropriately credited and we ask that you include the end user license and a DOI link to the formal publication on ScienceDirect.

If any part of the material to be used (for example, figures) has appeared in our publication with credit or acknowledgement to another source it is the responsibility of the user to ensure their reuse complies with the terms and conditions determined by the rights holder.

#### **Additional Terms & Conditions applicable to each Creative Commons user license:**

**CC BY:** The CC-BY license allows users to copy, to create extracts, abstracts and new works from the Article, to alter and revise the Article and to make commercial use of the Article (including reuse and/or resale of the Article by commercial entities), provided the user gives appropriate credit (with a link to the formal publication through the relevant DOI), provides a link to the license, indicates if changes were made and the licensor is not represented as endorsing the use made of the work. The full details of the license are available at <http://creativecommons.org/licenses/by/4.0>.

**CC BY NC SA:** The CC BY-NC-SA license allows users to copy, to create extracts, abstracts and new works from the Article, to alter and revise the Article, provided this is not done for commercial purposes, and that the user gives appropriate credit (with a link to the formal publication through the relevant DOI), provides a link to the license, indicates if changes were made and the licensor is not represented as endorsing the use made of the work. Further, any new works must be made available on the same conditions. The full details of the license are available at <http://creativecommons.org/licenses/by-nc-sa/4.0>.

**CC BY NC ND:** The CC BY-NC-ND license allows users to copy and distribute the Article, provided this is not done for commercial purposes and further does not permit distribution of the Article if it is changed or edited in any way, and provided the user gives appropriate credit (with a link to the formal publication through the relevant DOI), provides a link to the license, and that the licensor is not represented as endorsing the use made of the work. The full details of the

license are available at <http://creativecommons.org/licenses/by-nc-nd/4.0>. Any commercial reuse of Open Access articles published with a CC BY NC SA or CC BY NC ND license requires permission from Elsevier and will be subject to a fee.

Commercial reuse includes:

- Associating advertising with the full text of the Article
- Charging fees for document delivery or access
- Article aggregation
- Systematic distribution via e-mail lists or share buttons

Posting or linking by commercial companies for use by customers of those companies.

20. Other Conditions:

v1.9

Questions? [customercare@copyright.com](mailto:customercare@copyright.com) or +1-855-239-3415 (toll free in the US) or +1-978-646-2777.

---

---

## APPENDIX C: PERMISSION FOR IEEE PUBLISHED FIGURES

This permission grant allows the reuse of IEEE previously published figures in research and dissertations. The figures 5, 6, 7, 8, 9 and 10 from this document are originally from IEEE published material, each cited below the figure.

### Thesis / Dissertation Reuse

**The IEEE does not require individuals working on a thesis to obtain a formal reuse license, however, you may print out this statement to be used as a permission grant:**

*Requirements to be followed when using any portion (e.g., figure, graph, table, or textual material) of an IEEE copyrighted paper in a thesis:*

- 1) In the case of textual material (e.g., using short quotes or referring to the work within these papers) users must give full credit to the original source (author, paper, publication) followed by the IEEE copyright line © 2011 IEEE.
- 2) In the case of illustrations or tabular material, we require that the copyright line © [Year of original publication] IEEE appear prominently with each reprinted figure and/or table.
- 3) If a substantial portion of the original paper is to be used, and if you are not the senior author, also obtain the senior author's approval.

*Requirements to be followed when using an entire IEEE copyrighted paper in a thesis:*

- 1) The following IEEE copyright/ credit notice should be placed prominently in the references: © [year of original publication] IEEE. Reprinted, with permission, from [author names, paper title, IEEE publication title, and month/year of publication]
- 2) Only the accepted version of an IEEE copyrighted paper can be used when posting the paper or your thesis on-line.
- 3) In placing the thesis on the author's university website, please display the following message in a prominent place on the website: In reference to IEEE copyrighted material which is used with permission in this thesis, the IEEE does not endorse any of [university/educational entity's name goes here]'s products or services. Internal or personal use of this material is permitted. If interested in reprinting/republishing IEEE copyrighted material for advertising or promotional purposes or for creating new collective works for resale or redistribution, please go to [http://www.ieee.org/publications\\_standards/publications/rights/rights\\_link.html](http://www.ieee.org/publications_standards/publications/rights/rights_link.html) to learn how to obtain a License from RightsLink.


If applicable, University Microfilms and/or ProQuest Library, or the Archives of Canada may supply single copies of the dissertation.

Copyright © 2017 [Copyright Clearance Center, Inc.](#) All Rights Reserved. [Privacy statement](#). [Terms and Conditions](#).  
Comments? We would like to hear from you. E-mail us at [customer-care@copyright.com](mailto:customer-care@copyright.com)



## APPENDIX D: PERMISSION FOR FIGURE 13

Figure 13 was adapted from an illustration found on a video from The New England Journal of Medicine [43]. The NEJM allows reuse of content within a thesis or dissertation. The figure was substantially adapted (illustrating the skin and antenna to original image and eliminating sections of the original arm illustration that were not needed for this research purpose) to display intended message of this research. Thus this illustration differs substantially from the original illustration.



The NEW ENGLAND  
JOURNAL of MEDICINE

### About NEJM Permissions

---

**Reuse of Content within a Thesis or Dissertation**

Content (full-text or portions thereof) may be used in print and electronic versions of your dissertation or thesis without formal permission from the Massachusetts Medical Society, Publisher of the New England Journal of Medicine.

**The following credit line must be printed along with the copyrighted material:**

"Reproduced with permission from (scientific reference citation), Copyright Massachusetts Medical Society.